CHAPTER 3

RETRIEVAL OF HYDROMETEOR PROFILES IN TROPICAL CYCLONES AND CONVECTION BY A COMBINED RADAR-RADIOMETER ALGORITHM

3.1 Abstract

A physical retrieval algorithm is described to estimate vertical profiles of precipitation ice water content (IWC) and liquid water content (LWC) in tropical cyclones and convection over ocean from combined spaceborne radar and radiometer measurements. In the algorithm, the intercept parameter N_0 in the exponential particle size distribution (PSD) for rain, snow, and graupel are adjusted iteratively to minimize the difference between observed brightness temperatures (T_b's) and simulated ones by using a simulated annealing optimization method. The snow/graupel fraction profile is assumed in order to simulate the ice phase radiative transfer process more reasonably. Final optimal N_0's as well as the observed radar reflectivity profile are used to obtain LWC and IWC profiles.

The retrieval technique is investigated using the Fourth Convection And Moisture EXperiment (CAMEX-4) aircraft ER-2 Doppler radar (EDOP) and Advanced Microwave Precipitation Radiometer (AMPR) tropical cyclone and convection dataset during 2001. An indirect validation is performed by comparing the measured and retrieved 50 GHz

(independent channel) T_b. The global agreement shows not only the quality of the inversion procedure but also the consistency of the retrieved parameters with observations. The direct validation of the IWC retrieval by using the aircraft *in situ* microphysical measurements indicates that the algorithm can provide reliable IWC estimates, especially in stratiform regions. In convective regions, the large variability of the microphysical characteristics causes a large uncertainty in the retrieval, although the mean difference between the retrieved IWC and aircraft derived IWC is very small. The IWC estimated by the radar-only algorithm is higher than those retrieved by the combined algorithm and derived by the aircraft *in situ* observations, which suggests that information useful for improving the radar-only estimates is contained in the T_b measurements.

The algorithm is applied to the Tropical Rainfall Measurements Mission (TRMM) Hurricane Isabel (2003) case. The comparison of the hydrometeor profile retrieval with radar-only and radiometer-only algorithms shows that the nonuniform beamfilling bias for the combined algorithm is smaller than that for the radiometer-only algorithm, and is the same as that for the radar-only algorithm except for the LWC retrieval in the strong eyewall convective region. The spatial pattern of the retrieved liquid water path (LWP) and ice water path (IWP) and the shape of the retrieved LWC and IWC profiles are consistent with both TRMM Microwave Imager (TMI) and Precipitation Radar (PR) observations. The quantitative comparison shows that the retrieved mean LWP and IWP are in generally good agreement with the radar-only estimate or the radiometer-only estimate, depending on the rain type. The largest variability is found for the IWC/LWC

retrieval in the eyewall convective region, indicating that the unique dynamics in the eyewall represents the most complicated condition for the remote sensing retrieval.

3.2 Introduction

3.2.1 Importance of Hydrometeor Profiles in Tropical Cyclones and Convection

One of the main goals of the TRMM mission is to advance the earth system science objective of understanding the global energy and water cycles by providing four-dimensional distributions of latent heating over the global Tropics (Simpson et al. 1988; Kummerow et al. 2000). Tropical cyclones and convection are very important rainfall systems over the global Tropics and have a significant influence on the energy and water budgets.

The latent heat release in tropical cyclones provides heating and produces a warm-core structure, which is essential for development and maintenance of the circulation of the storm. Directly related to latent heating, ice water content (IWC) and liquid water content (LWC) have implications on tropical cyclone intensity (Cecil and Zipser, 1999; Rao and MacArthur, 1994). Early numerical hurricane model simulations show that the ice-phase microphysics plays an important role in the evolution of the simulated hurricane (Lord et al. 1984). To obtain the vertical distribution of latent heating profiles, the quantitative retrieval of hydrometor profiles is necessary.

3.2.2 Existing Algorithm Review and Examination

Microwave remote sensing techniques for rainfall can be classified broadly into the radar-only, radiometer-only, and combined radar-radiometer approaches based on the instruments to be used. Table 3.1 lists a subset of published TRMM-related single-instrument (radar-only and radiometer-only) rainfall retrieval algorithms. The radar-only algorithm is based on empirical Z-R, Z-LWC, and Z-IWC relationships to convert the radar reflectivity profile to the rain rate and hydrometeor content profile. The advantage of the spaceborne active microwave measurement is its ability to observe the vertical profile in high vertical and horizontal resolutions. But the empirical relationships are dependent on a fixed PSD assumption and unfortunately the radar-only retrieval is very sensitive to the variation of the PSD because Z, R, and M represent different moments of the particle diameter D (section 1.2.3). Another disadvantage of the spaceborne radar is the attenuation problem because the high-altitude platform requires a short radar wavelength in order to reduce the size of the antenna. An example of the radar-only algorithm is the TRMM 2A25 product (Iguchi et al. 2000).

Radiometer-only techniques for the estimation of precipitation have advanced considerably over the last decade due to both observational and radiative transfer modeling studies. These techniques can be broken down into 3 types: emission-based, scattering-based, and profiling algorithms. Emission-based algorithms are based on the low frequencies (usually <20 GHz) and the emission/absorption effect by raindrops (Wilheit et al. 1991; Hinton et al. 1992). Therefore they are only suitable for rain rate and LWC retrievals, but not for IWC estimates. Since the ocean surface is radiatively cold and its emissivity is nearly uniform at microwave frequencies, the thermal emission from

Table 3.1. A subset of published TRMM-related single-instrument (radar-only and radiometer-only) rainfall retrieval algorithms

	Radar-only	Radiometer-only		
		Emission	Scattering	Profiling
Published by	Iguchi et al. (2000) TRMM 2A25	Wilheit et al. (1997)	Spencer et al. (1989); Grody (1991); Ferraro and Marks (1995)	Kummerow et al. (1996) TRMM 2A12
Physics	Z-R Relationship from radar reflectivity profile	Thermal emission from rain water, cloud water at low frequencies	Scattering of background radiation by precipitation ice at high frequencies	Both emission and scattering of cloud and precipitation particles at all channels
Advantages	Can retrieve vertical profiles; High resolution	Insensitive to DSD	High horizontal resolution; Can be used both over ocean and over land	Retrieve vertical profiles in wide TMI swath
Dis-Advantages	Sensitive to DSD/PSD assumption; Attenuation problem	Low resolution, beamfilling problem; Sensitive to the freezing level assumption; Can be used only over ocean	Sensitive to ice PSD and density assumptions	Sensitive to cloud model microphysics, rain type classification, freezing level assumption

liquid hydrometeors and cloud liquid water increase upwelling brightness temperatures (T_b's), especially at lower frequencies (see section 1.2.2 for the detailed radiative transfer principle of the emission-based retrieval). These methods may not be used over land because of the high and nonuniform emissivity of the land surface. Emission-based retrievals are not very sensitive to the details of the DSD based on Wilheit et al. (1977). These algorithms are easy and computationally efficient but have been hampered by the uncertainty of the freezing level height and the beamfilling problem caused by the large footprints of the low frequency channels (Bell 1987; Chiu et al. 1990; Short and North 1990).

Scattering-based techniques of precipitation estimation are based on the ice scattering effect at high microwave frequencies (usually >37 GHz; Spencer et al. 1989; Grody 1991; Ferraro and Marks 1995; Ferraro 1997; Ferraro et al. 1998; Liu and Curry 1998). These techniques rely on the relation between optical depths of precipitation-sized ice particles and the vertically integrated ice water content or surface rainfall. The detailed radiative transfer calculation might be very complicated (section 1.2.2). Vivekanandan et al. (1991) developed a physical relationship between the 37-85 GHz T_b difference and the ice water path, while Spencer et al. (1989) and Ferraro and Marks (1995) used empirical methods in determining the T_b-R relationships. When applying the scattering method to the surface rain rate retrieval, it is an indirect retrieval since the surface rain may not be necessarily directly related to the upper level ice layer (such as warm rain and anvil regions). The high frequency channel usually has a higher horizontal resolution so that scattering algorithms will not be affected by the beamfilling problem as much as emission algorithms. The uncertainty of scattering methods mainly comes from

the sensitivity of the scattering coefficient to the phase, density, size distribution, shape, and orientation of the ice particles (Mugnai et al. 1990, Vivekanandan et al. 1991, Kummerow et al. 2001).

Observational (Fulton and Heymsfield 1991) and modeling (Mugnai et al. 1990; Smith et al. 1992; Adler et al. 1991) studies have shown that passive microwave measurements of precipitating clouds are sensitive to many aspects of the vertical distribution of various hydrometeor species and not only the surface rain rate. Profiling algorithms are designed to use all the available channels and both emission and scattering characteristics of cloud and precipitation particles. The general radiative transfer equation (1.11) needs to be solved for both low and high frequency channels. For TRMM, these channels are 10, 19, 37, and 85 GHz. The vertical hydrometeor profiles can be retrieved by various inversion techniques. An iterative scheme was used by Kummerow et al. (1989) and Kummerow et al. (1991) to match the observed brightness temperatures with those simulated from a relatively small number of specified profiles. Since there are typically multiple distinct profiles that can satisfy a small set of observations, other information about the vertical distribution of hydrometeors is needed to constrain the retrieval. The database of cloud model-derived profiles has been used extensively in many Bayesian retrieval methods (Kummerow et al. 1996 — known as the TRMM 2A12 product; Mugnai et al. 1993; Marzano et al. 1999). The success of these algorithms is limited by the problems of cloud model microphysical information (Evans et al. 1995).

As an example of the performance of radar-only and radiometer-only algorithms, three algorithms of hydrometeor profile retrieval have been examined by using a 1-yr TRMM tropical cyclone database (please see section 3.3.2 for the detailed desciption of this database), including one radiometer-only algorithm and two radar-only algorithms:

TRMM 2A12 (TMI only, Kummerow et al. 1996), 2A25 (PR only, Iguchi et al. 2000, Masunaga et al., 2002), and an empirical Z-M algorithm. The TRMM 2A12 provides hydrometeor profiles, while 2A25 provides attenuation corrected radar reflectivity and rainfall rate profiles. A series of theoretical Z-M relations based on the PSD assumption in 2A25 have been given by Masunaga et al. (2002). 2A25 hydrometeor profiles have been calculated by applying these Z-M relations to the attenuation-corrected PR reflectivity profiles for the 1-yr tropical cyclone database. The third algorithm uses the empirical Z-IWC (Black 1990) and Z-LWC (Willis and Jorgensen 1981) relationships (therefore Z-M method) to calculate IWC and LWC profiles from 2A25 radar reflectivity profiles. The Z-LWC relation given by Willis and Jorgensen (1981) is:

$$Z = 14610 LWC^{1.448} \tag{3.1}$$

The Z-IWC relations given by Black (1990) are:

$$Z = 219 IWC^{1.40}, \text{ for stratiform} \tag{3.2}$$

$$Z = 915 IWC^{1.51}, \text{ for convective} \tag{3.3}$$

$$Z = 670 IWC^{1.79}, \text{ for composite of all hurricane data} \tag{3.4}$$

In (3.1)—(3.4), Z is in mm^6m^{-3}, LWC and IWC are in g/m^3. In the two radar-only algorithms, the classification of rain type and the brightband height (or the freezing level) are determined by TRMM algorithm 2A23. For “others” rain type given by 2A23, (3.4) is used to calculate Z-M IWC. The top and bottom of the mixed phase region are defined at 500 m above or below the brightband height for stratiform region, at 750 m above or below the freezing level for convective or “others” region by following Iguchi et al.

(2000). In the Z-M and 2A25 algorithm, it is assumed that all particles above the top of the mixed phase region are ice and all particles below the bottom of the mixed phase region are liquid. Inside the mixed phase region, the values of IWC and LWC are interpolated from those at the top and bottom of the mixed phase region.

Fig. 3.1 gives the composite averaged LWC and IWC vertical profiles estimated by the above three algorithms in all regions of tropical cyclones, and in eyewall, inner rainband, and outer rainband regions for the 1-yr database. From the figure, a large variable range of LWC and IWC can be seen among the three methods, although 2A25 profiles are close to Z-M profiles in the rain region (below the melting level) and 2A12 profiles are close to Z-M profiles except for the lowest 2-3 km. The version 5 of 2A12 retrieval has a well-known problem in that region (C. Kummerow, personal communication). Because the version 5 2A12 algorithm uses a coupled radiative transfer model-cloud model database to statistically select rain rates and hydrometeor profiles best matched to microwave observations to create its rain rate and hydrometeor content profile estimates, the success of the version 5 of 2A12 algorithm is limited by the limited number of hydrometeor profiles in the cloud model database and the assumption of cloud model microphysics parameterization. It is obvious that 2A12 gives an unreasonable vertical shape of hydrometeor profiles at least in the lowest 2-3 km comparing to other 2 radar-only algorithms. The underestimation of 2A25 in the ice region is obvious. A similar underestimation of 2A25 (version 5) ice water content comparing with 2A12 for four representative tropical oceanic and tropical continental regions during July of 1998 and January of 1999 was found by Masunaga et al. (2002), who explained that the difference in the detectability of ice between TMI and PR results in the large discrepancy in the estimated ice amount. However, from our omparison, this explanation is

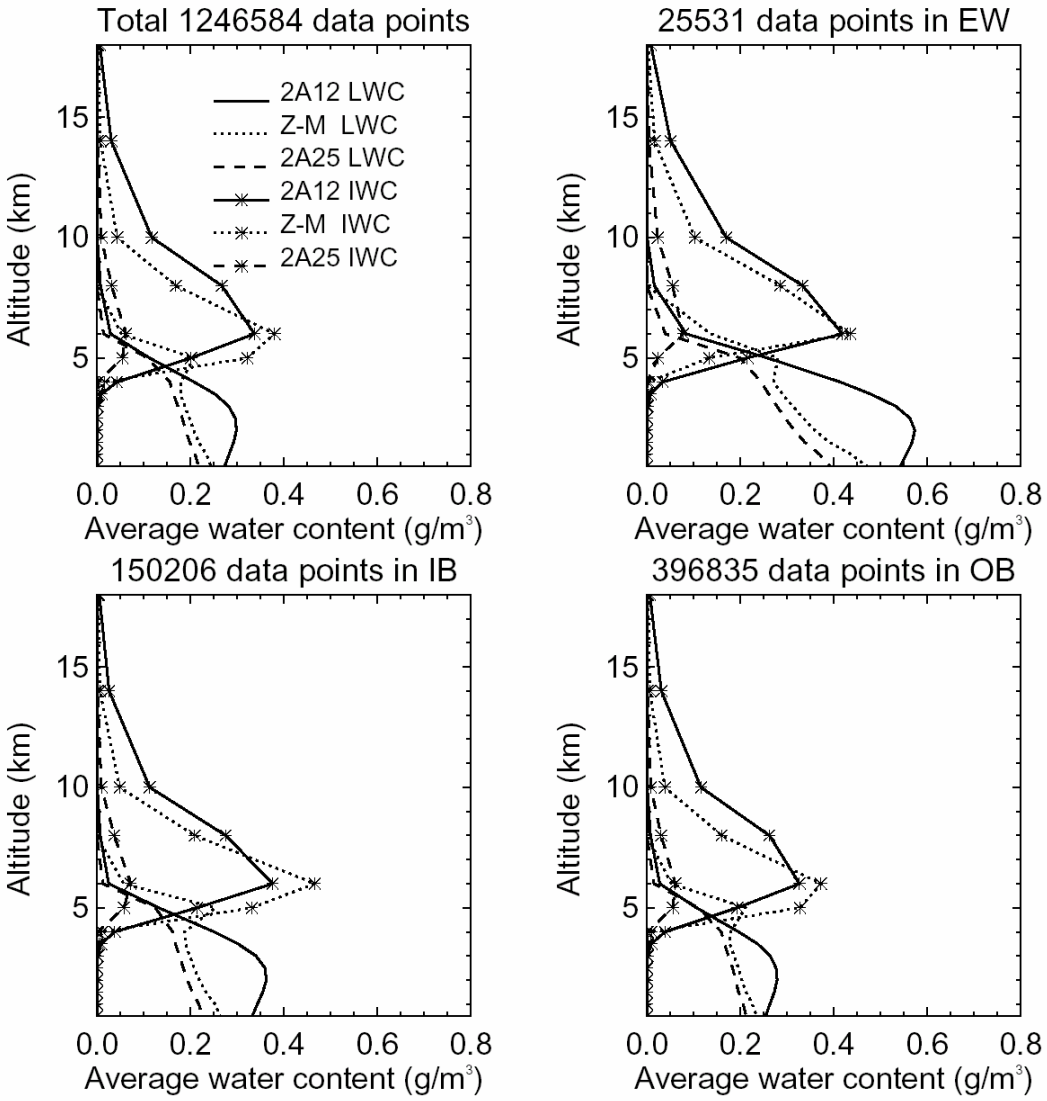

Figure 3.1. Hydrometeor vertical profile composites estimated by 2A12, Z-M, and 2A25 methods for (upper left) all regions in tropical cyclones, (upper right) eyewall regions, (lower left) inner rainband regions, and (lower right) outer rainband regions from the 1-yr TRMM tropical cyclone database.

misleading because the ice amount derived from Z-M method, which uses PR reflectivity as well, appears in agreement with TMI 2A12 algorithm. Uncertainty in the PR 2A25 Z-M relations is introduced by the algorithm's assumption of PSD, which likely has climatic biases; this is the most probable reason for the 2A25 underestimation. The Z-M method used here is derived from the aircraft microphysics data from three mature hurricanes, which could be biased when applied to other tropical cyclones in different stages. But generally, when applied to tropical cyclone databases, less uncertainty is expected for the Z-M method than for 2A12 and 2A25, because the latter two could be contaminated by having been derived using some precipitation systems other than tropical cyclones.

The average liquid water path (LWP) and ice water path (IWP) in Table 3.2 are the vertical integrals of IWC and LWC calculated from Fig. 3.1 (notice in both Fig. 3.1 and Table 3.2, the precipitation LWC and IWC from 2A12 are compared with the LWC and IWC derived from two other methods). We can see that the discrepancies of the total water content amount estimates between 2A12 and Z-M algorithms are within 7%, but the 2A25 is underestimated by about a factor of 6 for ice regions and about 20% for rain regions, when compared with the other two.

From this examination, the radiometer-only algorithm obtains an unrealistic estimate of the vertical profile shape, and the radar-only 2A25 algorithm gives a big underestimate of the total amount of ice water content because of the PSD assumption.

One thing we need to keep in mind is that in the radiative transfer model used by any radiometer-only (emission-based, scattering-based, and profiling) algorithms, the PSD must be assumed, similar as the radar-only algorithm. It is well-known that PSD

Table 3.2. Mean microphysical properties estimated by 2A12, Z-M, and 2A25 methods from the 1-yr TRMM tropical cyclone database (IWP and LWP in kg/m^2)

	All regions	Eyewall	Inner rainband	Outer rainband
2A12 IWP	1.49	1.90	1.52	1.45
Z-M IWP	1.39	1.76	1.60	1.34
2A25 IWP	0.24	0.33	0.27	0.24
2A12 LWP	1.25	2.49	1.50	1.17
Z-M LWP	1.16	1.98	1.26	1.14
2A25 LWP	0.94	1.60	0.97	0.94

variability is large, especially for ice particles. A fixed parameterization would cause uncertainties for any retrieval algorithm.

Airborne and satellite-borne radar and radiometer on the same platform, such as Tropical Rainfall Measuring Mission (TRMM) and Convection And Moisture EXperiement (CAMEX), provide a very powerful tool to estimate ice water content andliquid water content profiles in tropical precipitation systems. Recent studies demonstrate various ways in which the opportunities to estimate hydrometeor profiles and cloud characteristics improve by combining radar and radiometers (Olson et al. 1996; Viltard et al. 2000; Grecu and Anagnostou 2002; Marzano et al. (1999).

By combining radar and radiometer observations, the PSD parameters can be retrieved along with the hydrometeor profiles, which is the first advantage of a combined algorithm. Secondly, one of the biggest problems of emission-based radiometer algorithms is the determination of the freezing level (Wilheit et al. 1977, 1991, Kummerow et al. 2001). By adding radar observations, the freezing level can be estimated by the radar bright band height in stratiform regions and interpolated into neighboring convective regions, therefore minimizing uncertainties. Thirdly, the convective-stratiform separation represents another big uncertainty of a radiometer-only algorithm such as TRMM 2A12 (Kummerow et al. 2001). Although the rain type classification by radar data is also subject to some uncertainties, the separation based on the 3-D structure of the radar observation would definitely be better than that from the 2-D radiometer observations. Fourthly, a radiometer-only algorithm theoretically can give a good estimate of the integrated water content (IWP, LWP), but the radiometer observation is not enough to obtain the vertical shape of IWC and LWC because there are more independent variables within raining clouds than there are channels in the observing

systems. Instead radar can measure the vertical distribution of reflectivity. Therefore, a radar algorithm can give a reasonable vertical shape of the hydrometeor profiles. By combining these two observations, one can expect both a reasonable total amount of water content and vertical shape of the profiles. For developing a fully physical retrieval algorithm, it is likely that combining radar and radiometer information will lead to more realistic profiles and more accurate estimates.

Table 3.3 lists a subset of published combined radar-radiometer precipitation retrieval algorithms. One common characteristic of most of the combined approaches is that they are not fully based on physical models, but dependent on *a priori* statistical relationship (TRMM 2B31, Haddad et al. 1997) or *a priori* cloud model database (Marzano et al. 1999; Olson et al. 1996). Among a few fully physical algorithms, Skofronick-Jackson et al (2003)'s approach emphasizes high-frequencies (>150 GHz) and cannot be implemented to TRMM satellite observations; Grecu et al. (2004) provides a fully physical technique that has been applied to TRMM observations, but it uses the same N_0 [the interception coefficient in the particle size distribution (PSD] for rain, snow, and graupel, and cannot retrieve a reasonable hydrometeor profile in the ice region, although its rain rate retrieval is comparable with ground-base radar estimates.

3.2.3 Special Goals

In this chapter, we formulate and investigate a physical combined technique similar that estimates different N_0 values for rain, snow, and graupel, and which provides

Table 3.3. A subset of published combined radar-radiometer precipitation retrieval algorithms.

	Based on a priori database or relationship		Fully physical	
Published by	Haddad et al. (1997) TRMM 2B31	Olson et al. (1996), Marzano et al. (1999)	Skofronick-Jackson et al. (2003)	Grecu et al. (2004)
Physics	Use a statistical 10 GHz Tb and radar PIA relationship to constrain DSD in radar profile retrieval	Find the best match of simulated and observed reflectivity and Tb's from a cloud model database	Adjust PSD to get the best match between calculated and observed reflectivity and Tb's	Adjust PSD (N_0) to get the best match between calculated and observed reflectivity and Tb's
Advantages	Retrieve rainfall profiles; Application to TRMM	Retrieve Hydrometeor profiles	Emphasize ice water by using high frequencies (>150 GHz)	Retrieve rainfall profiles; Application to TRMM
Dis-Advantages	Not fully physical; Doesn't consider ice region	Sensitive to the representation of the cloud model database	Cannot be used for TRMM	Only retrieve N_0 for rain, poorly represent ice particles

* PIA: path integrated attenuation; Tb: brightness temperature.

physically meaningful estimates for both IWC and LWC profiles consistent with both radar and radiometer observations. This study concerns precipitation systems. The IWC and LWC in fact mean *precipitation* IWC and LWC in this whole Chapter. The precipitation microwave radar and radiometer at frequencies less than 85 GHz mainly detect precipitation-size particles. The contribution from cloud ice and liquid particles to the precipitation radar reflectivity is very small relative to the contribution from precipitation-size particles due to the Rayleigh scattering theory. The contribution from cloud ice and liquid particles to the radiometer T_b would cause some uncertainties in the retrieval and sensitivity tests about cloud IWC and LWC will be performed in section 3.5. Only the oceanic background is considered in this algorithm. The combined radar-radiometer retrieval algorithm developed here uses radar reflectivity derived hydrometeor profiles as input to a forward radiative transfer model to retrieve N_0's by minimizing the differences between observed brightness temperatures and calculated ones iteratively. The purpose of this chapter is:

(1) To formulate the combined radar-radiometer algorithm and analyze the error sources by doing the sensitivity tests using the radiative simulation. It is very important to understand the uncertainties for any algorithm.

(2) To implement this algorithm and apply it to tropical cyclone and convection data during CAMEX-4 observed by the NASA[1] EDOP[2] and AMPR[3] (also on the ER-2 aircraft). The advantage of airborne AMPR and EDOP data is that they have a higher surface resolution than TRMM sensors, which would average the signals from adjacent convective elements (Olson et al. 1996). For the

[1] NASA: National Aeronautics Space Administration.
[2] EDOP: ER-2 Doppler radar
[3] AMPR: Advanced Microwave Precipitation Radiometer

preliminary evaluation of the retrieval performance, the use of airborne data can avoid the complicating signal-averaging effects.

(3) To validate this algorithm by using independent aircraft *in situ* microphysical measurements and microwave radiometer measurements other than AMPR channels, and to compare the retrievals with radar-only and radiometer-only algorithms to understand the advantage and disadvantage of different methods.

(4) To apply the combined algorithm to a TRMM hurricane case, investigate the nonuniform beamfilling problem for satellite-based remote sensing retrievals, and compare the retrieval with radar-only, radiometer-only algorithms in different rain type regions inside the tropical cyclone.

3.3 Instrumentation

3.3.1 CAMEX-4

The Fourth Convection And Moisture Experiment (CAMEX-4) was based on Florida during Aug. 16 - Sept. 24, 2001 (Kakar et al., 2004). This cooperative NASA-NOAA experiment focused on the study of tropical cyclone development, tracking, intensification, and landfalling impacts using aircraft and surface remote sensing instrumentation. While remote sensing of the hurricane environment was the main objective of CAMEX-4, there were also separate flights to study tropical convection systems. During this field campaign, a large volume of data was collected from *in-situ* microphysical instruments and passive and active remote sensing instruments. With similar configuration as TRMM PR and TMI, the EDOP and the AMPR data have higher spatial and temporal resolution and are potentially very powerful tools to test an algorithm developed for TRMM since the beam-filling problem is minimized, especially

for some specific case studies. For evaluating the sources of uncertainties of IWC and LWC estimates from collocated EDOP and AMPR observations, microphysical sampling on the DC-8 aircraft and other microwave radiometer data could be used. Since EDOP has higher horizontal and vertical resolution, higher sensitivity, and longer wavelength (therefore less attenuation problem) than the TRMM PR, the shape of the radar reflectivity profile described by EDOP is more realistic than by the PR (Heymsfield et al. 2000). So a more realistic vertical hydrometeor profile could be obtained by using the combined algorithm on EDOP and AMPR observations.

Table 3.4 lists the instrumentation at CAMEX-4 used in this study. Below we discuss the CAMEX-4 instrumentation in some detail.

The EDOP is an X-band (9.6 GHz, 3.2 cm) Doppler radar with fixed nadir and forward pointing beams with a beam width of 2.9° (Heymsfield et al., 1996). It can map out the reflectivities and Doppler winds in the vertical plane along the aircraft path at a high spatial resolution (100 m horizontally, 37.5 m vertically). The ER-2 aircraft flies at a nominal high altitude of 20 km with a ground speed of about 200 m/s. With this satellite-like stable platform, the EDOP from the aircraft altitude directly measures the whole structure of vertical reflectivity and wind from deep convective systems, which is generally not possible with other low- and medium-altitude aircraft.

An X-band radar suffers from the attenuation problem, especially in intensive convective precipitation. Several methods have been developed to estimate the amount of radar attenuation. The classic attenuation-compensating method derived by Hitschfeld and Bordan (1954) gives a reasonable estimate if the attenuation effect is small, but its solution could be unstable when the attenuation is large. The surface reference technique

Table 3.4. CAMEX-4 instrument specifications

Instrument		Wavelength /frequency	Temporal/ spatial resolution	Observed or derived quantity
ER-2	ER-2 Doppler radar (EDOP)	9.6 GHz	Horizontal: 100 m, Vertical: 750 m	Reflectivity, Doppler velocity
	Advanced Microwave Precipitation Radiometer (AMPR)	10.7, 19.35, 37.1, 85.5 GHz	2.8, 2.8, 1.5, 0.6 km at surface	Brightness temperatures
	High Altitude MMIC Sounding Radiometer (HAMSR)	50.3, 51.76, 52.8, 53.481, 54.4, 54.94, 55.5, 56.2, 166.0, 183.31 ± 10, 183.31 ± 7.0, 183.31 ± 4.5, 183.31 ± 3.0, 183.31 ± 1.8, 183.31 ± 1.0 GHz	2 km at surface	Brightness temperatures
	ER-2 High Altitude Dropsonde (EHAD)	N/A	N/A	Vertical profiles of atmospheric temperatue, pressure, relative humidity, wind speed and direction
DC-8	2D-C, 2D-P image probes	N/A	1-s	Particle size distribution, ice water content
	DC-8 Dropsonde (D8D)	same as EHAD		

(SRT, Meneghini et al. 1983; Iguchi et al. 2000) uses a surface target (reflectivity of the ground in a precipitation-free area in proximity to the precipitation area) as the reference. The SRT can overcome the instability of the Hitschfeld-Bordan method. But the accuracy of radar attenuation estimate depends on the stability of the radar cross section of the surface. Unlike land surfaces, ocean surfaces have a relatively constant cross section and the SRT can provide a good estimate of the radar attenuation over ocean. Since this study focuses on precipitation over the tropical ocean, the EDOP attenuation correction is performed by using the SRT (Tian et al., 2002).

The AMPR is a four channel scanning passive microwave radiometer measuring fully or partially polarized radiation at 10.7, 19.35, 37.1, and 85.5 GHz (Spencer et al. 1994). The AMPR is also on the NASA ER-2 airplane. The antenna beamwidths are 8°, 8°, 4.2°, 1.8° for the 10.7, 19.35, 37.1, and 85.5 GHz channels, causing horizontal resolutions along the aircraft track at nadir of 2.8, 2.8, 1.5, 0.6 km, respectively, at a flight altitude of 20 km.

The AMPR detects precipitation and surface water by measuring natural microwave emission and scattering from cloud water, cloud ice, rainfall and surface water. The combination of low frequencies (< 37 GHz) and high frequncies (> 37 GHz) allows an estimate of both emission and scattering from precipitations. The high resolution AMPR observations have been used to describe the microphysical characteristics of tropical oceanic storms and to understand the nonhomogeneous beamfilling problem of low resolution satellite observations (McGaughey and Zipser 1996; McGaughey et al. 1996).

The High Altitude MMIC Sounding Radiometer (HAMSR) is a microwave atmospheric sounder recently developed by Jet Propulsion Laboratory flying also on the NASA ER-2 aircraft (Lambrigtsen and Riley 2002). It provides measurements that can be

used to infer the 3-D distribution of temperature, water vapor, liquid water and ice particles. Brightness temperatures are colletecd in 15 channels in 2 spectral bands during CAMEX-4, including the 8-channel 54-GHz temperature sounding band and the 7-channel 183 GHz humidity sounding band (see Table 3.3 for detailed frequencies). The HAMSR scans the plane perpendicular to the flight direction. At nadir, all channels detect a vertical polarization brightness temperature at a resolution about 2 km for both along-track and cross-track. In this study, HAMSR observations at 50 GHz (outermost wing of the 50-60 GHz oxygen emission band) are used as independent data to evaluate our algorithm. Although in oxygen emission band, 50 GHz channels can also be used in scattering studies because the ice-scattering processes in precipitation decreases the the observed brightness temperatures a certain amount in this channel. A sensitivity test of the radiance of this channel to the ice water path (IWP) and liquid water path (LWP) will be discussed in Section 3.5.

Cloud microphysics measurements by the Particle Measuring Systems (PMS) 2D-C and 2D-P probes on the DC-8 aircraft (Heymsfield et al., 2004a) are used as a validation data source. The 2D-C and 2D-P probes measured PSDs from about 30 μm to 6 mm in various increments (Heymsfield et al., 2004b). The uncertainty of the IWC calculation from PSD observations of 2D probes will be discussed in section 3.6.3. ER-2 and DC-8 dropsonde data (Halverson et al. 2004) are used as input to the algorithm.

3.3.2 TRMM

Launched in November 1997, the TRMM promises to provide critical information regarding the 4-D distributions of precipitation and latent heating in the Tropics (Simpson et al. 1988; Kummerow et al. 1996; Kummerow et al. 2000). The satellite's orbit is low

altitude (350 km) for relatively high resolution and low inclination (35°) in order to pass each sampling area in the tropics at a different hour of the day. This study uses data from the two chief sensors of TRMM: Precipitation Radar (PR) and TRMM Microwave Imager (TMI). PR is a three-dimensional precipitation radar with frequency of 13.8 GHz. The PR provides reflectivities from surface to 20 km above the earth ellipsoid with a 4.3 km × 4.3 km horizontal resolution and a 250 m vertical resolution at its nadir point. It has a 215 km swath width with a minimum detectable signal of nearly 17 dBZ. With relatively small wavelength (2.2 cm), the PR suffers a more severe attenuation problem than EDOP. For example, a 4.5 km column of rain with a rain rate of 10 mm/hr would attenuate the EDOP signal by 1.6 dB, while PR would be attenuated by 3.7 dB (Olson et al. 1996). This study uses the TRMM standard algorithm 2A25 (Iguchi et al. 2000) attenuation-correction reflectivity profiles. Absolute errors of the 2A25 reflectivity profiles due to uncertainties in the SRT attenuation correction could affect our retrieval, but it is unlikely that these errors are large and only the lowest part of each profile in rain regions is affected. This will have no effect for the retrieval of IWC. This study uses TRMM PR algorithm 2A23 (Awaka et al. 1998) to identify rain types, the bright band height, and the freezing level.

The TMI takes observations in nine channels at five frequencies – 10.7, 19.35, 21.3, 37.0, and 85.5 GHz – with corresponding resolutions of 63× 37, 30 × 18, 23 × 18, 16 × 9 and 7 × 5 km in the cross-track and down-track directions, respectively (Kummerow et al., 1998). All frequencies are measured independently in horizontal and vertical polarization planes except the 21.3 GHz channel, which measures the radiance in vertical polarization plane. The TMI scans conically at a constant off-nadir angle of 49°,

resulting in a boresight incidence angle of 52.8° from zenith at the earth's surface. The TMI 1B11 algorithm data are employed in this study.

A Precipitation Feature (PF) algorithm has been developed by Nesbitt et al. (2000) to identify individual storms within the combined TRMM dataset. A 5-yr (Dec. 1997 -- Dec. 2002) University of Utah (UU) PF database has been set up, in which PR and TMI data are collocated within the 215-km wide PR swath to identify contiguous areas of PR rainfall and TMI 85-GHz ice scattering. A nearest-neighbor matching technique was used to match every PR pixel with the nearest TMI pixel, with the PR used as the base grid. The criteria of the PF areas are: at least four contiguous pixels (~75 km^2) on the PR grid having at least 20 dBZ near surface reflectivity or TMI 85-GHz polarization corrected temperatures (PCTs, Spencer et al. 1989) of 250 K or less. The PFs were then classified by their radar and ice scattering properties into three categories: PF without ice scattering (warm rain), PF with ice scattering, and PF with a mesoscale convective system (MCS, readers are referred to Nesbitt et al. 2000 for the details of these definitions).

Meanwhile, a 1-yr (Dec. 1997 -- Dec. 1998) tropical cyclone database of collocated TRMM, PR, and Lightning Imaging Sensor (LIS) observations was created and analyzed by Cecil et al. 2002. The tropical cyclone was subdivided into three separate regions: eyewall, inner rainband, and outer rainband. The categorizations were made subjectively, based on the horizontal fields of PR reflectivity and 85-GHz ice scattering. In this database, the mean radii for eyewall region, inner rainband region, and outer rainband region are 50, 135, and 350 km, respectively. Inside above regions, PFs were identified. Inside any PF, stratiform, convective, and "others" are separated by TRMM PR algorithm 2A23 (Awaka et al. 1998). This 1-yr TRMM tropical cyclone database consists of *648*

TRMM overpasses of 79 tropical cyclones, i.e., each cyclone was observed on an average of eight overpasses.

These two databases are very powerful and allow the investigation of the various properties of PFs in different regimes and compare the properties of tropical cyclones and other rainfall systems over Tropics (Nesbitt et al. 2000, Toracinta et al. 2002, Cecil and Zipser 2002, Cecil et al. 2002, Yorty 2001, Mota 2003, Nesbitt and Zipser 2003, Nesbitt et al. 2004). For the purpose of this study, these databases not only provide an easy-to-use combined PR and TMI dataset, they also allow us to examine the performance of the retrieval algorithm in different PFs.

3.4 Algorithm Description

The CAMEX and TRMM datasets with the combination of radar and radiometer data from the same platform provides an excellent opportunity to use a combined radar-radiometer algorithm to improve hydrometeor profile retrievals. Preliminary radiative transfer calculations using collocated aircraft radar and radiometer observations have been performed by Zipser et al. (2000). Based on their approach that uses a radar-derived hydrometeor profile as an input to a forward radiative transfer model (RTM), the combined radar-radiometer algorithm developed here estimates hydrometeor profiles in tropical cyclones and convection by minimizing the differences between observed and calculated T_b's iteratively. The plane parallel microwave radiative transfer code used here was developed by Kummerow et al. (1996). In this RTM, the PSD is assumed to be exponential:

$$N(D) = N_0 e^{-\lambda D} \tag{3.5}$$

where D is the equivalent spherical particle diameter, N_0 is the intercept parameter and λ is the slope parameter. Substituting (3.5) to definition equations of the water content M (1.19) and the radar reflectivity Z (1.21):

$$M = \frac{\pi \rho N_0}{\lambda^4} \tag{3.6}$$

$$Z = \frac{720 \alpha N_0}{\lambda^7} \tag{3.7}$$

where ρ is the particle density and in g/mm^3, Z is in $mm^6\ m^{-3}$, N_0 is in $m^{-3}\ mm^{-1}$, M is in g/m^3. (3.7) is obtained following (Braun 2004; Fovell and Ogura 1988). α is the ratio of the backscattering cross sections σ_b for the frozen particles and liquid water. As pointed out in section 1.2.3, the standard radar system determines the water equivalent Z. Due to the difference of the refractive index between ice and liquid water, σ_b for ice particles is ~4.7 time less than that for liquid water. So α is 0.213 for snow and graupel, 1 for rain. Then λ can be expressed as a function of (N_0, M) or (N_0, Z):

$$\lambda = \left(\frac{\pi \rho N_0}{M}\right)^{0.25} = \left(\frac{720 \alpha N_0}{Z}\right)^{1/7} \tag{3.8}$$

In the combined algorithm, the iteratively adjusted parameters would be the interception coefficients N_{0r}, N_{0s}, and N_{0g} for rain, snow, and graupel, respectively in (3.5). The slope parameter λ would be adjusted along with N_0 because λ can be determined by any two of the following three parameters: N_0, M, and Z. Although the PSD is assumed

to be exponential for the entire retrieval, the intercept parameter N_0 would be retrieved profile by profile. Notice that N_{0r}, N_{0s}, and N_{0g} are assumed to be constant for any individual vertical profile in all layers. This assumption would not cause large uncertainties because the horizontal variation of the PSD is much larger than its vertical variation and the use of different N_0 for rain, snow, and graupel can also overcome part of this problem.

The flow chart for the algorithm is shown in Fig. 3.2. Input fields for the radiative transfer model are built from various observation data sources. Initial hydrometeor content profiles are estimated from radar reflectivity Z measurements by using an N_0 scaled Z-M relationship derived from microphysics data fitting. An iterative inversion is performed to retrieve the hydrometeor profiles by minimizing the difference between observed and calculated brightness temperatures.

3.4.1 The RTM

A radiative transfer model (RTM) is needed to calculate the microwave upwelling brightness temperature. The original RTM used here was described by Kummerow et al. (1988). It is not our purpose to review in detail the principles of this RTM, but its main characteristics are described here. It is based on the one-dimensional Eddington approximation for a multilayered plane parallel medium by solving the general microwave radiative transfer equation given in (1.11). The emissivity of sea surface is calculated according to the incidence angle and polarization of the radiation, the sea surface temperature, the salinity, and the surface roughness induced by driven waves. For

the atmospheric absorption, water vapor, molecular oxygen and cloud water are taken into account. The Rayleigh approximation is used to compute the absorption coefficient

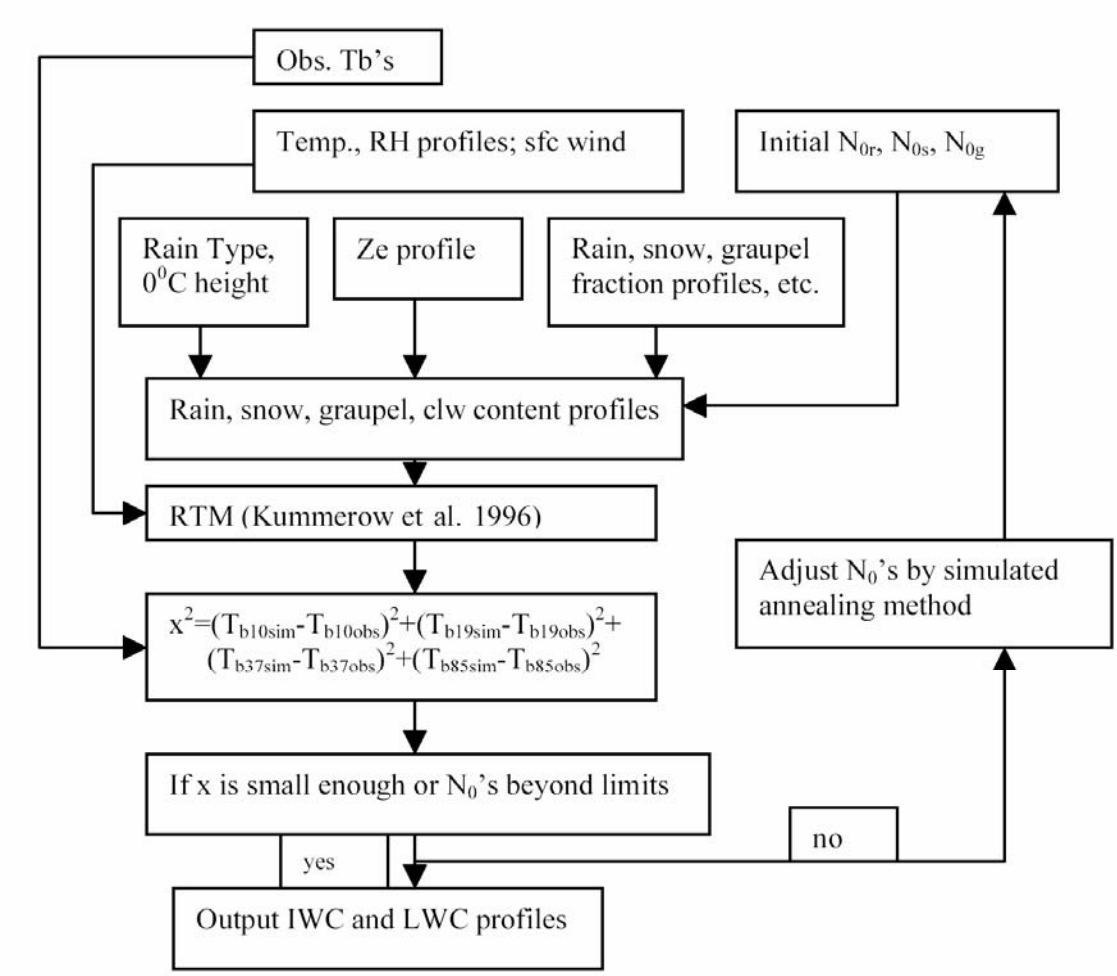

Figure 3.2. The retrieval algorithm flowchart.

of the cloud water. The Mie theory is employed to compute the absorption and scattering by precipitation-size hydrometeors.

As given by Kummerow et al. (1996), the mean errors of this Eddington approximation relative to a Monte Carlo scheme model are generally small (about 2.7 K at 85 GHz and 1.2 K at 19 GHz). But the maximum errors can reach 12 K at 85 GHz and 5.3 K at 19 GHz in very strong precipitation. Based on their Fig. 2, these large departures occur at the region with IWP greater than 20 kg/m^2. In tropical oceanic rainfall systems such as tropical cyclones, this large IWP is very rare. So the brightness temperature calculation from the 1-D Eddington approximation would cause uncertainties as small as 1-3 K for most tropical oceanic storms. These differences are of the same order as those obtained in the inversion procedure of this algorithm. However, this type of model is easy to operate and efficient.

This RTM allows for six hydrometeor types (e.g., cloud ice, cloud liquid water, rain water, snow, graupel, and hail). In this application to tropical cyclones and convection systems, only four hydrometeor types (e.g., cloud liquid water, rain water, snow, and graupel) are considered. The cloud ice is not taken into account because of its negligible influence in most cases (Viltard et al. 1998). The sensitivity test about the uncertainty caused by the cloud ice will be provided in section 3.5. And updrafts are generally weak and therefore hail is very rare in oceanic tropical convective systems (LeMone and Zipser 1980; Zipser and LeMone 1980) and in hurricanes (Jorgensen et al. 1985). Densities are assumed as of 1.0 g/cm^3 for rain, 0.1 g/cm^3 for snow, and 0.4 g/cm^3 for graupel. In fact, a more reasonable retrieval could be done by using a density-diameter relationship for

frozen particles instead of using a fixed density assumption. But it is hampered by the lack of a suitable density-diameter relationship from microphysics measurements.

In the RTM, flexibility exists in that the user can input the cloud profile and select the viewing angle, frequency and polarization. It requires as input instrument specifications, the sea surface temperature, sea surface wind speed, vertical profiles of temperature, height, relative humidity, and PSD of the hydrometeors in the cloud. In the RTM, the cloud liquid water distribution is assumed to be mono-disperse. The distributions of rain, snow, and graupel are assumed to follow an exponential shape. All particles are assumed to be spherical in shape because it is extremely difficult to consider nonspherical particles from a computational point of view. While the use of spherical particles is somewhat idealized, this simplification allows the important effects of particle size distribution to be considered separately from that of aspherical particles.

3.4.2 Hydrometeor Content Calculations

To derive water content M from radar reflectivity factor Z, a Z-M relationship is needed. Any specific Z-M relationship is dependent on the PSD. For the exponential PSD as given (3.5), we can get a N_0 scaled Z-M relationship by combining (3.6) and (3.7) and canceling out λ as follow:

$$Z = 720\alpha(\pi\rho)^{-1.75} N_0{}^{-0.75} M^{1.75} \tag{3.9}$$

(3.9) can also be expressed:

$$M = (720\alpha)^{-0.57} \pi\rho N_0{}^{0.43} Z^{0.57} \tag{3.10}$$

Note that the parameters in (3.9) and (3.10) have the same physical meanings and units as those in (3.6) and (3.7). We can rewrite (3.10) into:

$$M = m' N_0^{(1-n')} Z^{n'} \tag{3.11}$$

where m' is a constant for a specific particle density and particle phase, n' is a constant. Note that there is no dependence of m' and n' on λ. This is the theoretical N_0 scaled Z-M relation based on the exponential PSD, from which we see that the Z-M relation is only dependent on N_0 for a specific particle density and particle phase. One thing we have to be aware is that (3.6)-(3.10) are obtained by integrating the PSD from diameter D equal 0 to infinity. This represents an ideal condition of nature. For actual conditions, the power format of (3.11) will hold (see the following paragraph), but m' and n' might be different from the constants given in (3.10).

Joss and Gori (1978) noted that if after accumulation during long intervals, the rain PSD is generally found to be close to the exponential, but the "instant" PSD departs markedly from the exponential. The gamma distribution has been introduced to account better for the shape of the distribution at high rain rate observed by disdrometers. The gamma PSD is referred as to:

$$N(D) = N_0 D^{\mu} e^{-\lambda D} \tag{3.12}$$

where μ is the shape parameter. We see that when $\mu = 0$, a gamma PSD becomes an exponential PSD. A drawback of the gamma distribution is that the intercept parameter N_0 can no longer be considered to be a physical quantity, because its *dimension itself*

($m^{-4-\mu}$) is ill defined. Testud et al. (2001) developed a normalization approach to overcome this difficulty. They defined N_0^* as a normalized N_0 for the gamma PSD. N_0^* is equivalent to N_0 for an exponential PSD, therefore it is physically meaningful. With this approach, any two integrated rainfall parameters (*X*, *Y*) can be expressed as:

$$X = mN_0^{*(1-n)}Y^n \tag{3.13}$$

We can substitute *M* for *X* and *Z* for *Y*, then (3.13) is very similar to (3.11). But here the coefficients *n* is dependent on μ, m is dependent on μ and the particle density ρ. Both theoretical and observational evidence (Testud et al. 2001) indicates that *m* and *n* are only weakly dependent on μ, therefore most precipitation-related relationships (e.g., radar reflectivity vs precipitation water content, radar reflectivity vs rain rate, reflectivity vs attenuation) strongly depend on N_0^* and only weakly dependent on μ for a specific particle density. This property has been exploited in many radar-only and radar-radiometer combined profiling algorithms (Ferreira et al. 2001; Grecu and Anagnostou 2002; Grecu et al. 2004; Viltard et al. 2000), including the official TRMM PR 2A25 algorithm (Iguchi et al. 2000).

For the gamma PSD, the μ-dependent *m* and *n* in (3.13) can be computed from fits to experimental data. For instance, Viltard et al. (2000) gives a *Z-LWC* relationship scaled by N_0^* as:

$$LWC = 3.1\times10^{-6} N_0^{*0.455} Z^{0.545} \tag{3.14}$$

where LWC is in gm^{-3}, N_0^* is in m^{-4}, Z is in mm^6m^{-3}. This relation is valid for temperatures between 273 and 293 K and μ=1.

In this study, for the rain region, we use a *Z-LWC* relationship developed by Mircea Grecu (personal communication) using polarimetric radar observations from Florida to obtain the rain water content. This Z-LWC relation has coefficients very close to those above:

$$LWC = 2.5 \times 10^{-6} N_0^{*0.412} Z^{0.588} \tag{3.15}$$

The cloud liquid water content is assumed to be 10% of the rain water content following the assumption of Tesmer and Wilheit (1998). The uncertainty caused by this assumption will be tested in the sensitivity test (section 3.5).

In the ice region, we develop a N_0^* scaled *Z-IWC* relation by fitting 2D probe microphysics measurements during CAMEX-4 for temperatures below 253 K and applying it into all ice regions by assuming that this relationship is very weakly sensitive to the temperature (Viltard et al. 2000). The analysis of aircraft size distribution data is provided by Dr. Andy Heymsfield, who uses an assumption of the density-diameter relationship derived by Heymsfield et al. (2002a) to calculate the IWC from the PSD measurements. In this fitting, 26,249 size distribution samples are used from DC-8 flights Sept. 6, 7, 9, 15, 19, 22, 23, 24, 2001. For keeping the validation study independent on this fitted *Z-IWC* relationship, the 2D probe samples in the EDOP-AMPR-PMS dataset (see section 3.6.1) have been removed from these 26,249 samples. Based on the normalization approach by Testud et al. (2001), dN is defined by the ratio of the actual

N_0^* to a reference N_0^* (say 8×10^6 m $^{-4}$ as in Marshall-Palmer PSD, actual value does not really matter as long as it is in reasonable magnitude), then the ratio of specific water content, IWC here, to dN, or IWC/dN, and the ratio of reflectivity to dN, or Z/dN, should be linearly related in a log-log representation. Fig. 3.3(a) shows this linear fitting by using aircraft microphysical measurements with the correlation coefficient equal to 0.99. Notice that in this fitting dataset, 10log10 (dN) has a mean value of about 20, so the y-axis corresponds to a range of radar reflectivity from –20 to 40 dBZ. Although there is some scatter in the fitting, this N_0^* scaled Z-IWC regression is still better than traditional N_0^*-independent Z-IWC regression, which is shown in Fig 3.3(b). The linear relationship shown on Fig. 3.3(a) can be converted into a Z-IWC relationship as follow:

$$IWC = 2.3\times 10^{-5} N_0^{*0.412} Z^{0.588} \tag{3.16}$$

where N_0^* can be N_{0s}^* (for snow) or N_{0g}^* (for graupel). Note that the coefficient m depends on the particle density also. In (3.16), $m = 2.3\times 10^{-5}$ represents the composite effect from all ice particles. Different Z-IWC relations for snow and graupel, respectively, are needed for a more reasonable retrieval. But it is very difficult to obtain this kind of microphysical measurements.

By comparison with the Z-IWC relations given by Black (1990), (3.16) can also be written as:

$$Z = 8\times 10^7 N_0^{*-0.7} IWC^{1.7} \tag{3.17}$$

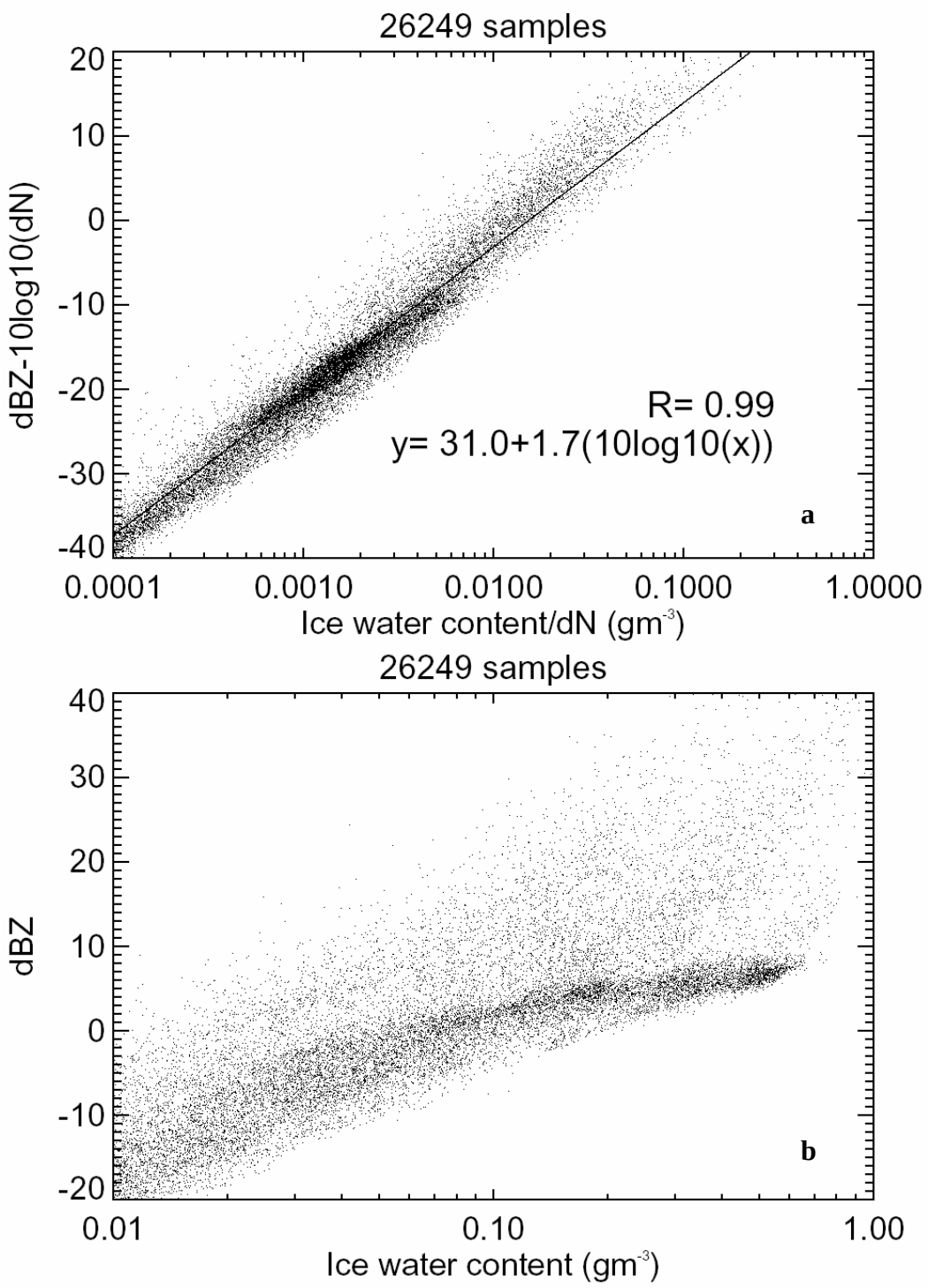

Figure 3.3. Relationships between reflectivity and ice water content from aircraft 2D probe microphysics measurements during CAMEX-4: (a) N_0^* normalized reflectivity plotted against normalized ice water content, (b) original reflectivity plotted against ice water content.

The slope of this Z-IWC relation is close to that in (3.4) derived for a composite of all hurricane data by Black (1990). But the a-coefficient is dependent on N_0^*, which allows us to retrieve N_0^* values that are consistent with radiometer measurements. Notice that (3.4) will be very close to (3.17) when $N_0^* = 1.4 \times 10^6$ m^{-4}. In the following text, we will still use N_0 instead of N_0^* to represent the adjusted intercept parameter in the algorithm because the PSD is assumed to be exponential in the RTM, therefore N_0 and N_0^* have the same physical meaning.

Since we are concerned with both ice water and rain water, a parameterization of the snow and graupel fraction profile is needed to simulate brightness temperatures at 37 and 85 GHz. From microphysical measurements in field programs, Stith et al. (2002) found that stratiform precipitation above the melting layer has no graupel in significant amounts, so we assume all snow. In the convective rain region, the amount of graupel varies from case to case, so we refer to the hurricane modeling results by Lord et al. (1984) and assume that graupel reaches its maximum at 6 km, and snow reaches its maximum at 12 km. The specific value of the snow fraction (f_s) is set to vary based on the intensity of the convection. A sensitivity test about snow/graupel fraction will be performed in Section 3.5.

A 100% liquid water is assumed below the bottom of the melting layer for all rain types. A linear interpolation is used to set the fraction of rain, snow, and graupel within the melting layer for all rain types. The freezing level is found based on the radar bright band height for CAMEX-4 data, and 2A23 output is used for TRMM data. The top (bottom) of the melting layer is 500 m for stratiform and 750 m for

convective/intermediate regime above (below) the freezing level similar to Iguchi et al. (2000).

3.4.3 Inversion Procedure

We iteratively look for the set of N_0^*'s that leads the RTM to calculate simulated brightness temperatures as closely as possible to the observed ones. The inversion is done iteratively from the initial values. At each iteration, the error function is defined by the sum of the square errors in 4 channels at 10, 19, 37, and 85 GHz:

$$\chi^2 = \sum_{i=1}^{N_f} q_i (T_{bsimi} - T_{bobsi})^2 , \tag{3.18}$$

where N_f is the number of independent frequencies used in this retrieval, which corresponds to the number of independent brightness temperatures to adjust. The T_{bsimi} and T_{bobsi} are respectively the calculated and observed brightness temperatures for the *i*th frequency. In application to CAMEX-4 data, T_b represents the nadir viewing brightness temperature without polarization effect. The coefficient q_i is a weighting factor that allows us to control the contribution from a given frequency.

This inversion is performed by searching for the minimum of the error function numerically. The simulated annealing technique (Goffe et al. 1994) is used in this inversion. The features of this technique are: (1) it explores the function's entire surface and tries to optimize the function while moving both uphill and downhill; (2) it is largely independent of the initial values and step lengths; (3) it can escape from local optima and go on to find the global optimum. Its code is flexible to allow users to set the upper and

lower limits of the iteration parameters, adjust the running speed by adjusting different parameters.

As pointed out by Viltard et al. (1998), this inversion must be overdetermined due to the noise in the measurements and possible ambiguity of the solution. So the four independent brightness temperatures only allow us to retrieve three variables, which are the N_0's for rain, snow, and graupel in this algorithm.

3.5 Sensitivity Test

To understand the effects of the input parameters on the microwave radiation and to predict the error for our retrievals, we simulated the AMPR nadir T_b uncertainties associated the sea surface wind speed, vertical profiles of the temperature and relative humidity, cloud ice, cloud liquid water below the freezing level, the snow/graupel fraction in ice regions, and the supercooled liquid water above the freezing level. Those retrieval inputs along with the instruments noise are the major error sources. Although a lack of the melting layer representation in the RTM could also cause some uncertainties (Nesbitt et al. 2004), the effect of melting particles is currently not considered in this algorithm because there is not enough observational evidence to suggest how to simulate the bright band. Although some idealized simulation studies in this issue have been done by Olson et al. (2001a,b), many uncertainties exist when applied to real data.

Our final retrievals are LWC and IWC profiles. But here we test the sensitivities by using only the integral values LWP and IWP since the vertical distribution (or shape) of LWC and IWC is determined by the radar reflectivity profile in this algorithm. To provide sensitivity tests of individual error sources, all parameters (e.g., surface wind

speed and the profile of temperature and relative humidity), except the one to be tested, used in the RTM are fixed at the mean values of observations in tropical cyclones during CAMEX-4. The brightness temperature errors are then determined from an uncertainty in the tested parameters. For the snow fraction (f_s , therefore the graupel fraction is 1- f_s), since there are no reference values, a series of f_s from 100% to 0% will be tested. In this sensitivity test, the Marshall-Palmer (1948, therefore MP) PSD distribution is assumed for rain and snow, and the Rutledge and Hobbs (1984, therefore RH) PSD is assumed for graupel. This strategy is similar as the one used in Prasad et al. (1995), in which the MP distribution is used for rain and for ice at upper levels of the cloud (above 6 km) and the RH scheme for ice at lower layers of the cloud (below 6 km). In the RH PSD, N_0 is 0.04 cm^{-4} to represent a flatter slope due much larger particles. Input hydrometeor profiles to the simulation are selected from EDOP-derived profiles of observations of tropical oceanic precipitation systems with both the rain layer and the ice layer (e.g. not warm rain profiles) during CAMEX-4. Since in the selected profiles, a small (large) LWP corresponds to a small (large) IWP, the following figures only show either LWP or IWP as the x-axis parameter.

Before looking the sensitivity test results, we need to estimate how much uncertainty could be caused by the RTM and the instrument errors. As mentioned in section 3.4.1, the accuracy of the RTM-calculated T_b is estimated at about 1-3 K, depending on the atmospheric situation, and accuracy of the different channels of the radiometers is estimated at about 3-5 K. Therefore, the total uncertainty is about 4-8 K.

Fig. 3.4 shows the absolute value of the T_b error (DT_b) caused by an error ± 5 m/s in the surface wind speed (WS). Uncertainties of T_b's are exponentially decreased with

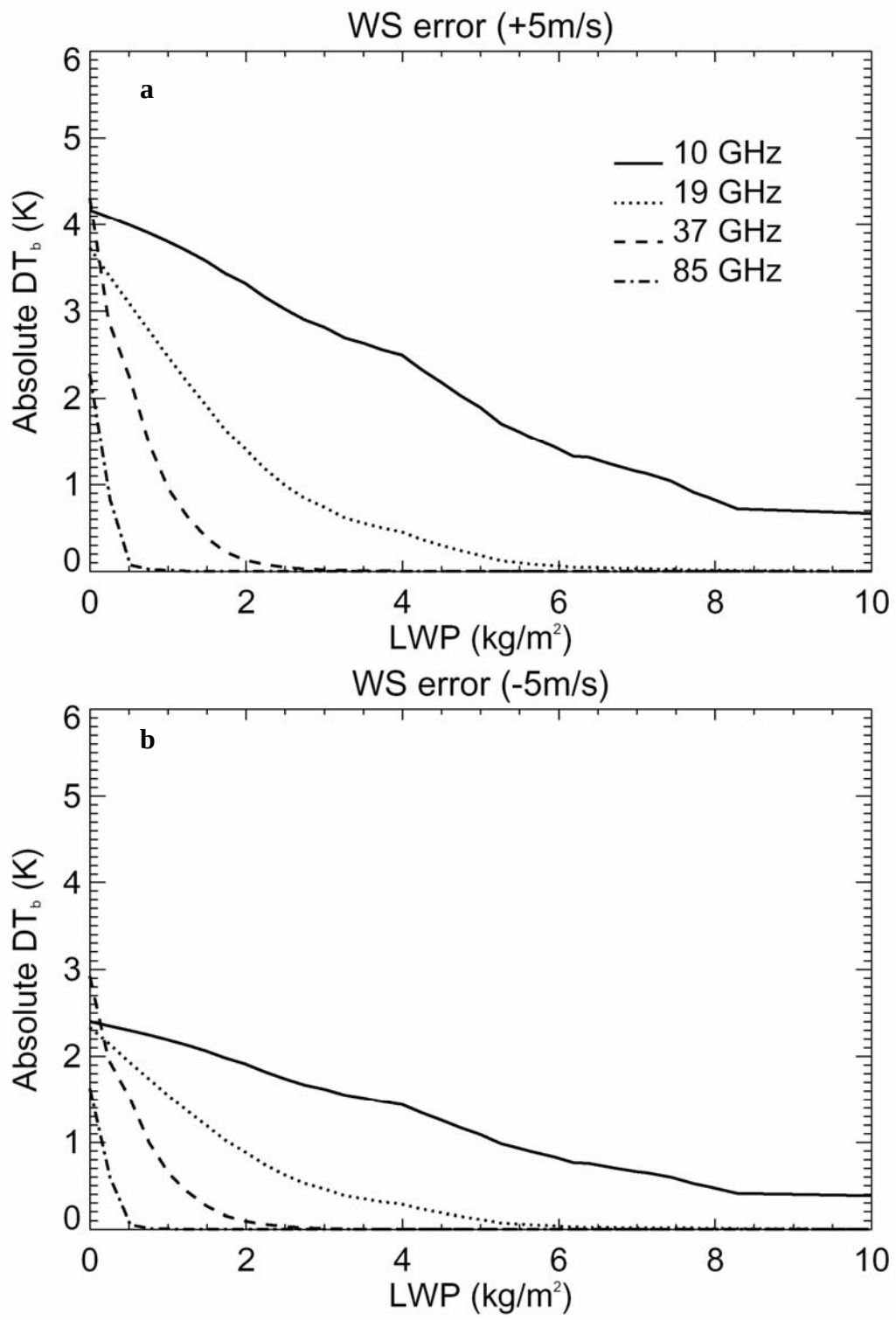

Figure 3.4. Simulated absolute values of uncertainties of 10, 19, 37, and 85 GHz nadir brightness temperatures (T_b) due to errors of (a) +5 m/s and (b) –5 m/s near sea surface wind speed.

the intensity of the precipitation. As the LWP value reach 3 kg/m^2 (mm), all DT_b's are below 3 K, which is within the RTM Eddington approximation error. It is also noticed that the uncertainties at high frequencies (85 and 37 GHz) caused by this wind error are usually very small for LWP greater than 1 kg/m^2 (mm) and can be neglected. The unequal absolute value of DT_b between +5 m/s and –5 m/s WS errors shown in Fig. 3.4a and Fig. 3.4b are produced by the nonlinear relationship between sea surface emissivity and near-surface wind speed. However, in the tropical cyclone environment, the variation of wind speed could be large, so would be the DT_b's at 10 and 19 GHz, which will cause errors in LWC retrievals, especially in medium intensity of precipitations. Fortunately, the largest surface wind speed variation usually occur around the eyewall area in which the convection is very intensive, so we believe the uncertainty is not very big.

Fig. 3.5 shows the effect of ± 2 K error in the temperature profile (including sea surface temperature). The 85 GHz T_b is most sensitive to the error of temperature profile and its uncertainty even slightly increases with the increase of LWP, while other frequencies have the opposite effect. Considering that the variability of the temperature profile is not very large over tropical ocean (less than 3-4 K by checking all the dropsonde data during CAMEX-4), the largest uncertainty (about 3-4 K from Fig. 3.5) at 85 GHz is still within the RTM Eddington approximation error.

Fig. 3.6 shows the absolute value of the T_b error (DT_b) caused by an error $\pm 10\%$ in the relative humidity (RH). Since in precipitating clouds, the relative humidity doesn't vary as much as that in non-precipitation clouds, a $\pm 10\%$ error of RH is typical. The T_b uncertainties caused by RH error have the similar behavior as those caused by temperature error, but they are much smaller. In precipitation clouds (LWP greater than 1

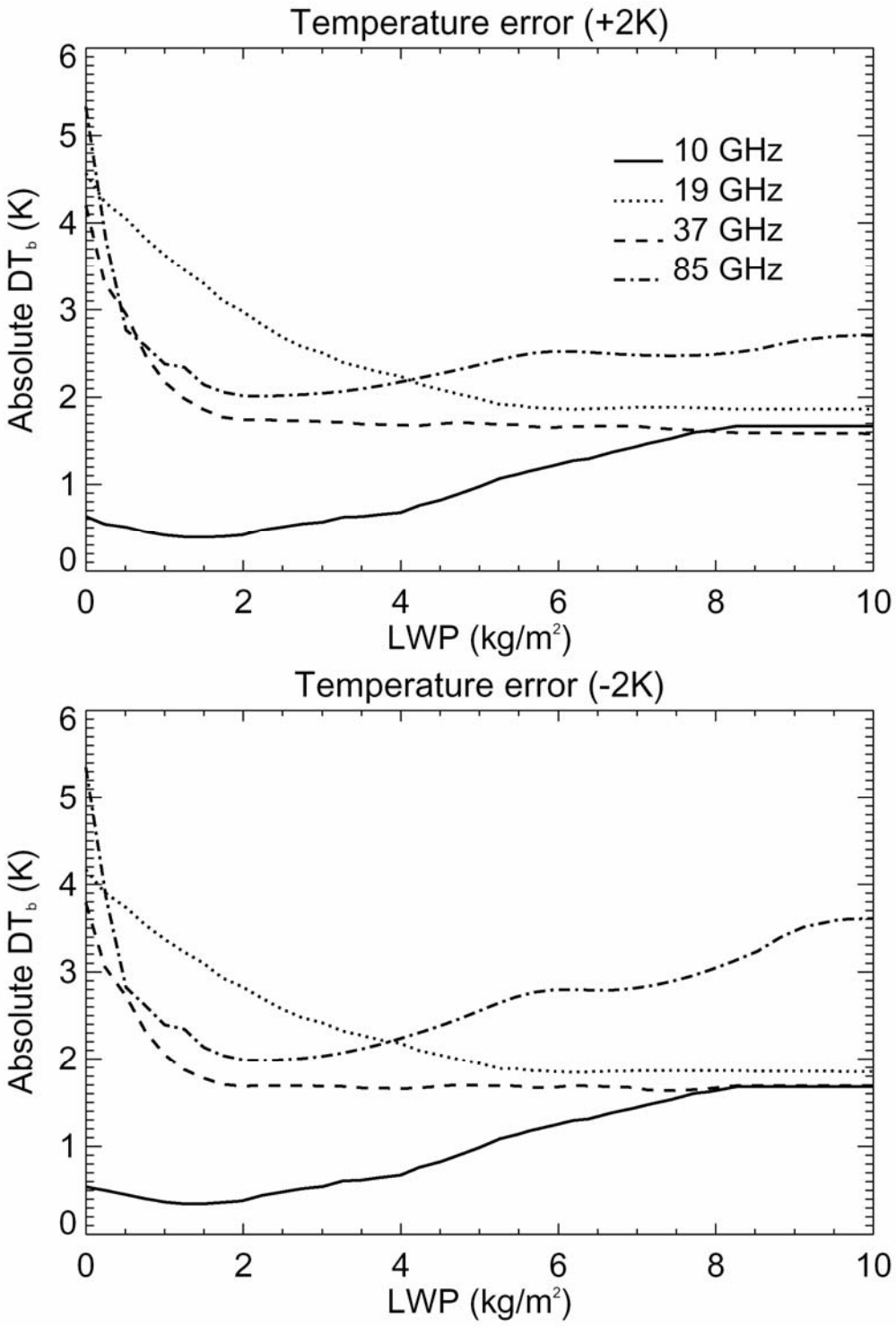

Figure 3.5. Simulated absolute values of uncertainties of 10, 19, 37, and 85 GHz nadir brightness temperatures (T_b) due to errors of ± 2 K in the whole temperature profiles.

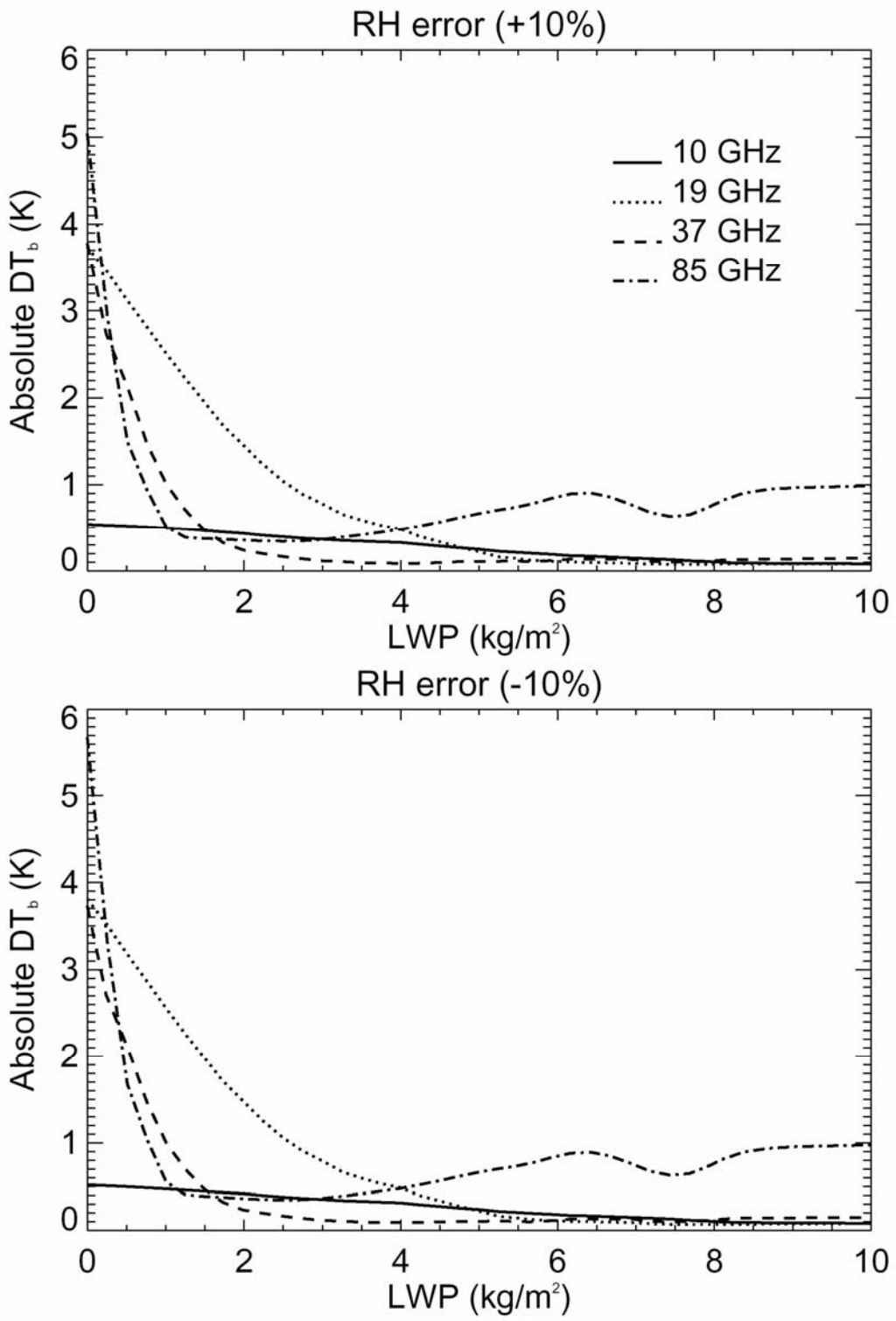

Figure 3.6. Simulated absolute values of uncertainties of 10, 19, 37, and 85 GHz nadir brightness temperatures (T_b) due to errors of $\pm$ 10% relative humidity.

kg/m^2), DT_b's for 10, 19, and 37 GHz are much less than 1 K, DT_b at 85 GHz is around 1 K.

In the algorithm, we neglect the effect from the cloud ice. To determine the uncertainty caused by this assumption, Fig. 3.7 presents the absolute value of the T_b error caused by the existence of 1, 3, 5 kg/m^2 cloud ice water path (cloud IWP) at 10, 19, 37, and 85 GHz, respectively. By examining the 2A12 output for the 1-yr TRMM tropical cyclone data (see section 3.3.2), we estimate that the maximum and mean cloud IWP values for tropical cyclones are 5 and 0.4 kg/m^2. From Fig. 3.7, we see that the largest uncertainty caused by the cloud ice is at 85 GHz. For a 5 kg/m^2 cloud IWP, the absolute 85 GHz DT_b could reach 7 K at the precipitation IWP value of 10 kg/m^2, which is still within the total uncertainty of RTM and instrument errors.

In the retrieval, the could liquid water is assumed to be 10% of the rain water in the tropical oceanic precipitation system. This will cause some uncertainties because the extinction coefficient is proportional to the liquid water mass for sufficiently small particles at the microwave band, and the amount of the cloud liquid water varies case by case. It could be as low as only 5% or as high as 20% of the rain water content as shown in the 2A12 output for the 1-yr tropical cyclone database. Fig. 3.8 shows the absolute value of DT_b caused by the cloud liquid water path (cloud LWP) errors of 10-50% of precipitation LWP at 10, 19, 37, and 85 GHz, respectively. In the could liquid water sensitivity test, the cloud liquid water is present mainly below the freezing level. The effect of the supercooled liquid water will be examined later. From Fig. 3.8, we see that the largest uncertainty is at 10 GHz, and it is less than 8 K.

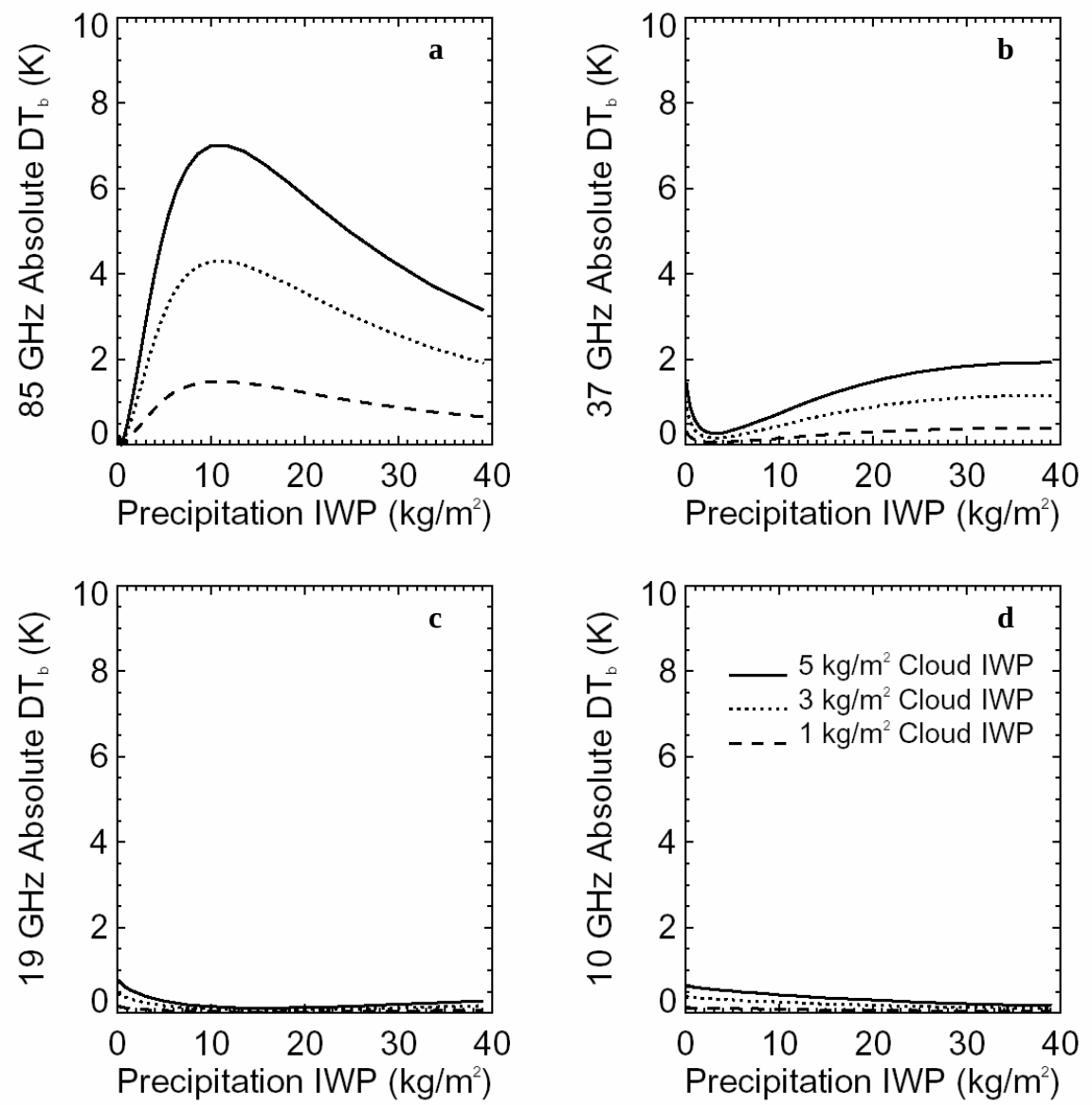

Figure 3.7. Simulated absolute values of uncertainties of (a) 10, (b) 19, (c) 37, and (d) 85 GHz nadir brightness temperatures (DT_b) due to the existence of 1, 3, 5 kg/m^2 cloud IWP.

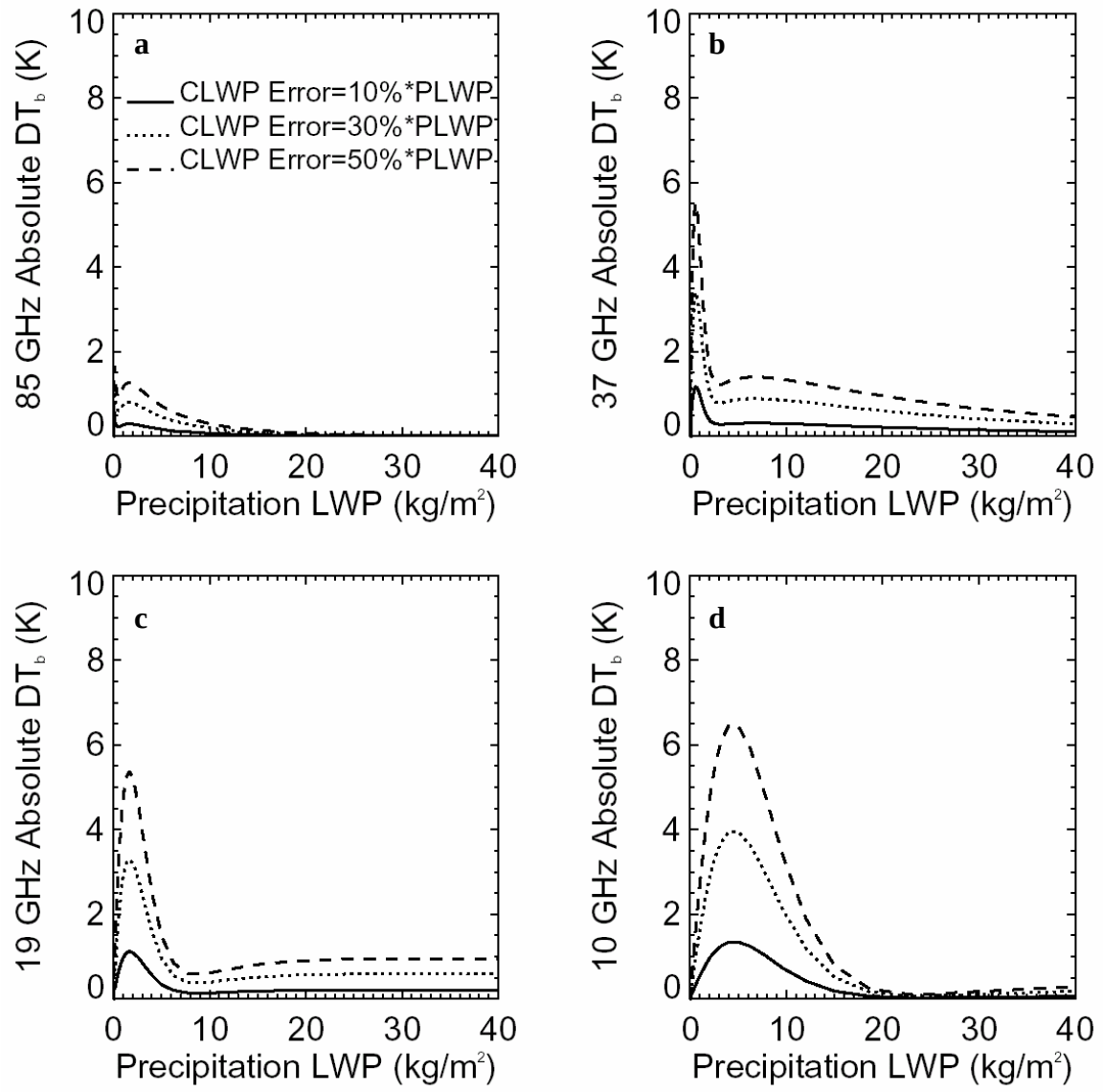

Figure 3.8. Simulated absolute values of uncertainties of (a) 10, (b) 19, (c) 37, and (d) 85 GHz nadir brightness temperatures (DT_b) due to the cloud liquid water path (cloud LWP) errors of 10-50% of precipitation LWP.

In simulating the effect of the variation of snow/graupel fraction, we keep graupel in lower layers (maximum at 6 km) and snow in upper layers (maximum at 12 km), but change the total fraction of snow in this sensitivity test. It is found that the variation of f_s has no significant effect on T_b's at 10 and 19 GHz, so we examine this effect only for higher frequencies based on IWP. Besides 37 and 85 GHz, which are the channels we use for the retrieval, the T_b's at 50 and 52 GHz (HAMSR channels) are also investigated because we want to use the HAMSR observations in these channels to validate our retrieval indirectly. Since these channels are around the oxygen emission lines and originally designed for measuring the temperature sounding (Lambrigtsen and Riley 2002), it is necessary to determine if they are sensitive to rain emission or ice-scattering. If not, then this kind of validation would be not meaningful.

Fig. 3.9 shows the T_b's at 85, 52, 50, and 37 GHz as a function of IWP for the snow fraction at 100%, 90%, 75%, 50%, 25%, 10% and 0%, with a f_s =100% representing pure stratiform rain regions. Variability of the T_b depressions with the snow/graupel fractions is evident, with the 85 GHz channel representing the largest change. Similar relations were found by Vivekanandan et al. (1991), in which the 85 GHz T_b is a different function of 85 GHz optical thickness for different bulk ice densities from 0.2 to 0.9 g/cm^3 for a simulation of a continental hail storm. In their model, only one frozen hydrometeor was assumed, so the bulk ice density effect there is similar to the snow/graupel fraction effect in our simulation here. Notice that the equivalent bulk ice densities in this study range only from 0.1 to 0.4 g/cm^3 because we only consider tropical oceanic storms and hail is very rare in this kind of system.

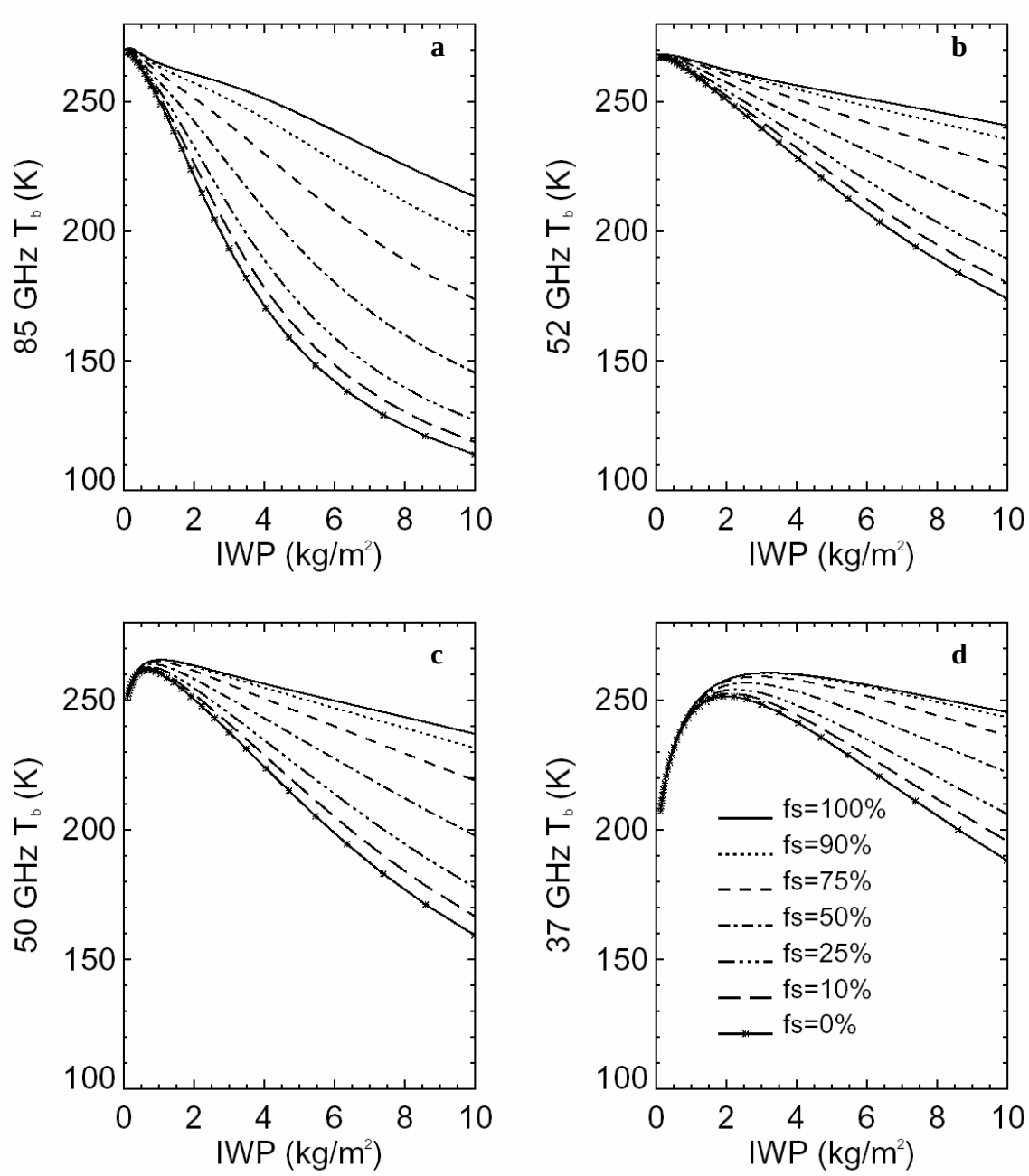

Figure 3.9. Simulated nadir-view brightness temperatures at (a) 85 GHz, (b) 52 GHz, (c) 50 GHz, and (d) 37 GHz as a function of ice water path (IWP) for snow fractions of 100%, 90%, 75%, 50%, 25%, 10% and 0%.

It is pretty clear that the snow/graupel fraction represents the dominant error sources in this retrieval. In stratiform regions, this effect is minimized because observational studies have shown that graupel is not present in tropical oceanic precipitations in significant amounts (Stith et al. 2002; Black and Hallett 1986, 1999). However, in convective regions, graupel may be present, but its relative amount is uncertain. A convective intensity dependent snow/graupel fraction scheme is needed to decrease this uncertainty. Fiorino (2002) examined the microphysics data during KWAJEX and concluded that on average, graupel contributes from about 70% at 4-5 km to 20% at 9-10 km of the total ice water content. This result corresponds to about 50% graupel fraction on average. In this study, we use 85 GHz T_b as the indicator of the convective intensity. For 85 GHz T_b less than 200 K, f_s =25% is assumed; for 85 GHz T_b greater than 200 K but less than 230 K, f_s =50% is assumed; for 85 GHz T_b greater than 230 K, f_s =75% is assumed. Here f_s refers to the integral snow fraction corresponding to the total IWP. We keep the vertical distribution of snow maximized at 12 km and graupel at 6 km as mentioned in previous section. Above 85 GHz T_b thresholds are decided by looking some examples of AMPR/EDOP observations. They are somewhat arbitrary.

From Fig 3.9 (b) and (c), in convective situations, the T_b depression at 52 GHz and 50 GHz could reach 60 K and 65 K respectively for IWP = 10 kg/m^2 and f_s =50%. The corresponding values for 85 GHz and 37 GHz are 120 K and 40 K, respectively. So it can be concluded that the radiative transfer characteristics of 50 and 52 GHz are in between those of 85 and 37 GHz and could be a good indicator for ice-scattering in convective situations. But it is noticed that the T_b depression at 52 GHz is less than that for 50 GHz.

This is a sign that shows the 52 GHz radiation is contaminated by the oxygen emission line at about 54 GHz. Although we could use the 52 GHz channel to identify ice-scattering in convective regions, we should use it with caution in stratiform regions because in these situations, the T_b depressions are not very large and are easily contaminated by oxygen emission. For the 50 GHz channel, the oxygen emission contamination is minimized and could be used as an independent validation source.

The combined algorithm assumes no supercooled liquid water above the freezing level. This may be true for most cases because the strength of updrafts in tropical cyclones is generally very weak (Zipser and LeMone 1980; Jorgensen and LeMone 1989; Jorgensen et al. 1985; Lucas et al. 1994; Zipser and Lutz, 1994; Cecil et al. 2002; Toracinta et al. 2002). However, for some extreme cases, "hot towers" might be exist in hurricanes (Simpson 1963; Black et al. 1994; Herman and Heymsfield 2003; Black et al. 2003; Heymsfield et al. 2001). The strong updraft in this region could bring some liquid water aloft. In the ice region, in addition to snow and graupel species, there could be a certain amount of supercooled water. Fig. 3.10 shows the effect of the existence of 0.2, 1.2, and 2.4 kg/m^2 supercooled liquid water path (supercooled LWP) between 6-10 km. We see that the increase of T_b's at four channels due to the existence of the supercooled water is evident. For example, at 85 and 37 GHz, the T_b increases are up to 40 K due to 2.4 kg/m^2 supercooled LWP. Therefore, the no-supercooled water assumption in the combined algorithm could cause some uncertainties for both ice and liquid water amounts.

Error sources from radiometer observations are analyzed above. The uncertainty for radar measurements is mainly from the attenuation, which will only affect the LWC

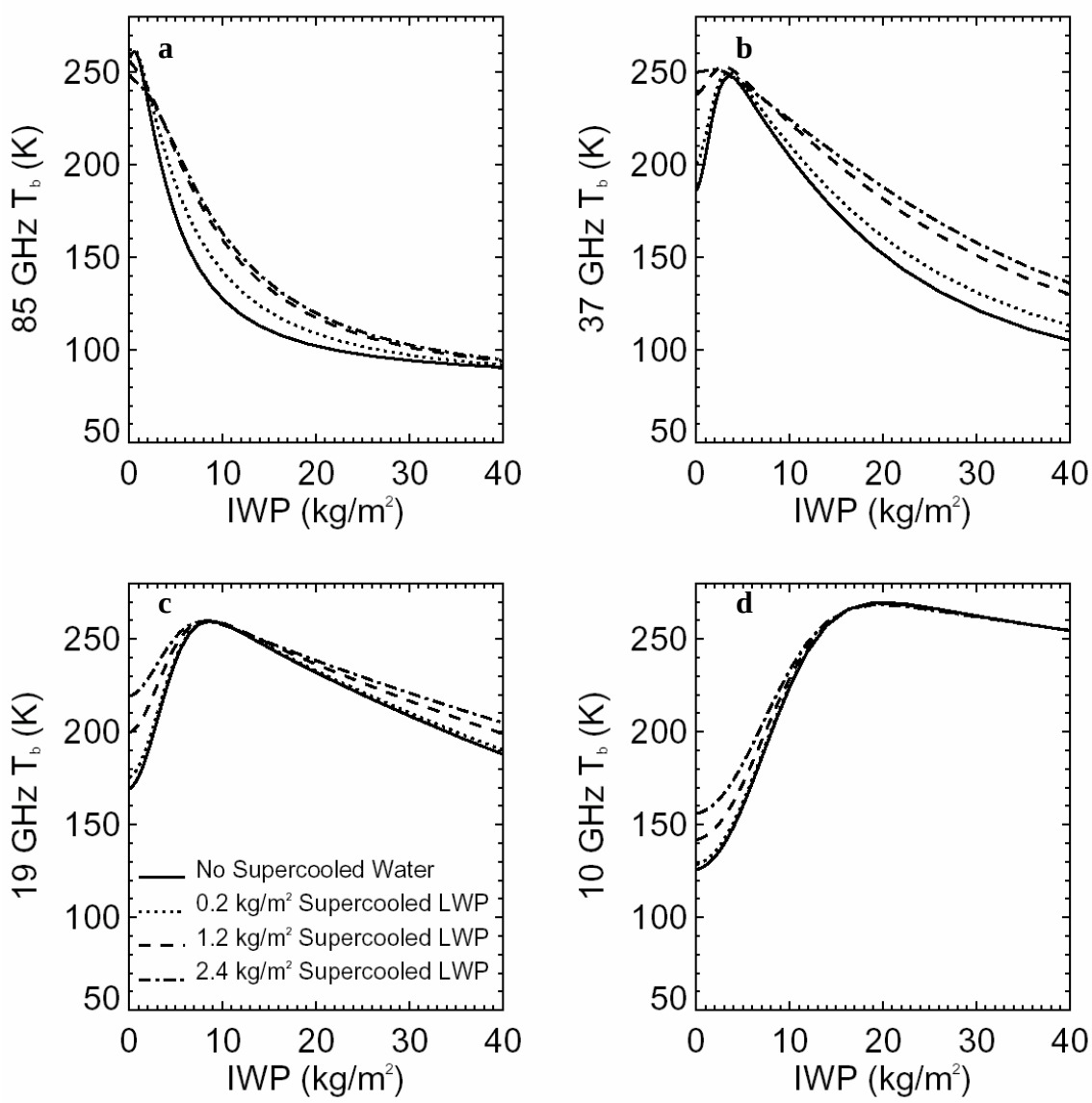

Figure 3.10. Simulated nadir-view brightness temperatures at (a) 85 GHz, (b) 37 GHz, (c) 19 GHz, and (d) 10 GHz as a function of IWP for supercooled liquid water paths (supercooled LWPs) of 0, 0.2, 1.2, and 2.4 kg/m^2.

retrieval. According to (3.15), a series of LWC absolute and percentage errors caused by ± 5 dBZ attenuation correction error at reflectivity equal to 40 dBZ and N_0 equal to 0.08, 0.16, 0.32 cm^{-4} are calculated and shown in Table 3.5. The error in nonlinear and is upto 97% for +5 dBZ attenuation correction error.

Another error source of this algorithm is the exponential coefficient *n* in the N_0 scaled Z-LWC and Z-IWC relationships given in (3.15) and (3.16). Usually, the retrieval could be very sensitive to the exponent in an empirical relationship (Gerald Mace, personal communication). Although the variation of *n* is expected to be very small due to its weak dependence μ (see section 3.4.2 for details), we need to examine the sensitivity of retrievals due to small changes of *n*. In this test, we choose two typical EDOP radar reflectivity profiles, one from stratiform regions and one from convective regions in hurricanes. These radar reflectivity profiles along with the AMPR T_b values are input to the algorithm. Given *n* changes (delta(n)) of ± 0.01 and ± 0.02, variations of retrieved LWC and IWC profiles are plotted in Fig. 3.11. Generally, the sensitivity for both LWC and IWC is larger in the convective region than that in the stratiform region. The largest uncertainties of the LWC and IWC for delta(n) = ± 0.02 are about 22%. This implies that the exponential coefficient *n* in the N_0 scaled Z-LWC and Z-IWC relationships should be a suitable value for the current situation, otherwise, even a 0.02 uncertainty of *n* could cause up to 22% error on the LWC and IWC retrieval.

Table 3.5. Liquid water content (LWC) absolute (abs) and percentage (%) errors caused by ± 5 dBZ attenuation correction error at reflectivity equal to 40 dBZ and N_0 equal to 0.08, 0.16, 0.32 cm^{-4}.

		N_0 (cm^{-4})					
		0.08		0.16		0.32	
		abs error (g/m^3)	% error	abs error (g/m^3)	% error	abs error (g/m^3)	% error
Reflectivity attenuation correction error (dBZ)	+5	0.38	97	0.50	97	0.67	97
	+4	0.28	72	0.37	72	0.50	72
	+3	0.20	50	0.26	50	0.35	50
	+2	0.12	31	0.16	31	0.22	31
	+1	0.06	14	0.08	14	0.10	14
	-1	0.05	13	0.07	13	0.09	13
	-2	0.09	24	0.12	24	0.16	24
	-3	0.13	33	0.17	33	0.23	33
	-4	0.16	42	0.22	42	0.29	42
	-5	0.19	49	0.26	49	0.34	49

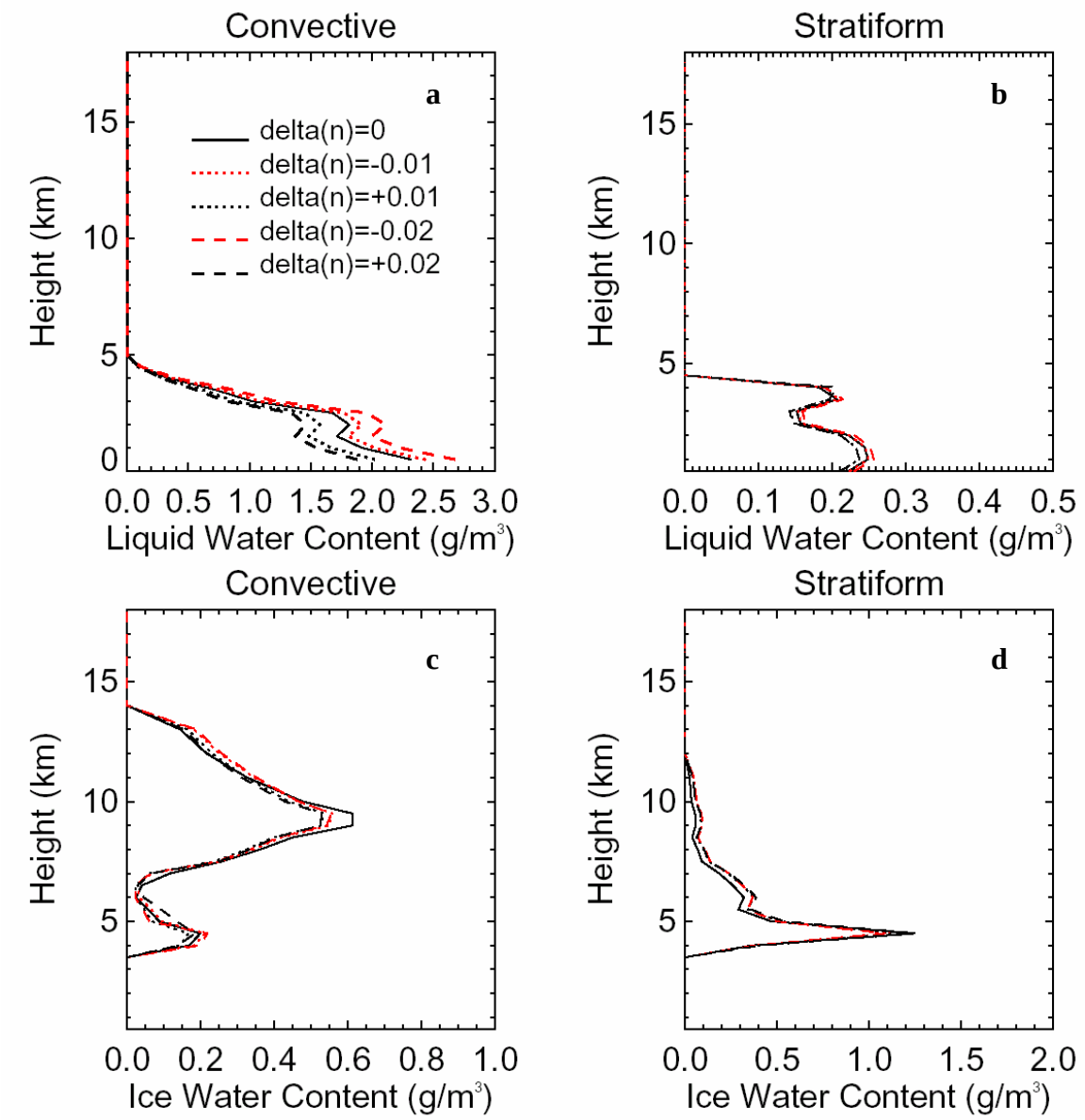

Figure 3.11. Variation of the retrieved (a) convective LWC profile, (b) stratiform LWC profile, (c) convective IWC profile, (d) stratiform IWC profile for the n change (delta (n)) equal 0, ± 0.01 and ± 0.02.

3.6 Application to CAMEX-4 Observations

3.6.1 Dataset

Observations from CAMEX-4 (Kakar et al. 2004) are used in the retrieval algorithm. A collocated dataset is obtained from 7 flights during Sept. 09, 10, 22, 23, 24, 2001, 3 of them are from Hurricane Erin (Sept. 10), 2 of them are from Hurricane Humberto (Sept. 23, 24), one of them from Tropical storm Humberto (Sept. 22), and one from a Gulf of Mexico thunderstorm (Sept. 09). A dominant part of this dataset is from tropical cyclones. To facilitate collocation of passive and active microwave measurements from the AMPR and EDOP, only the nadir-view data from these instruments are considered. At nadir, the AMPR measurements represent an equal mix of horizontal and vertical polarization. When matching EDOP and AMPR data, 1 km horizontal grid is chosen, which is close to the EDOP surface footprint (1.1 km). EDOP and AMPR data are averaged/interpolated into the 1-km grid points. The rain type is classified subjectively, using the EDOP reflectivity and Doppler velocity observations. A Gaussian fit to the vertical reflectivity profile (L. Belcher and G. Heymsfield, personal communication) is used to identify the bright band height in stratiform regions, therefore determining the freezing level. For convective regions, the freezing levels determined from neighboring stratiform regions are used and interpolated.

For the seven flights, a total of 1646 collocated samples are found, of which 1019samples are from 3 Erin flights and with HAMSR observations available (therefore EDOP-AMPR-HAMSR dataset); the remaining 627 samples are from Sept. 09, 22, 23, 24 flights and with DC-8 aircraft in-situ PMS 2D-C and 2D-P microphysics data available at about 9-11 km altitude (therefore EDOP-AMPR-PMS dataset). Table 3.6 shows a

Table 3.6. Characteristics of the 7 CAMEX-4 flights

	Flight Date	Time (UTC)	Storm	DC-8 Altitude (km)	Total sample	Stratiform sample	Convective sample	No rain sample
EDOP-AMPR-PMS dataset	010922	19:32-19:40	Humberto	8.5	104	72	32	0
	010923	20:33-20:53	Humberto	10.6	240	188	52	0
	010924	21:28-21:42	Humberto	11.2	170	145	25	0
	010909	18:33-18:42	Thunderstorm	8.9	113	88	25	0
EDOP-AMPR-HAMSR dataset	010910	16:50-17:15	Erin	N/A	301	257	20	24
	010910	17:54-18:22	Erin	N/A	325	157	70	98
	010910	19:14-19:47	Erin	N/A	393	313	17	63
Total number of samples					1646	1220	241	185

summary of these seven-flight datasets. The parameters derived from *in situ* measurements are averaged into 1 km grid to match with EDOP/AMPR data. For comparison with the retrieval, the LWC and IWC profiles are also calculated by applying empirical Z-M relations to EDOP reflectivity measurements, in which Z-IWC relationship is from Black (1990) and Z-LWC relationship is from Willis and Jorgensen 1981 (therefore radar-only or Z-M algorithm).

3.6.2 Quality of Inversion

Numerous tests of the simulated annealing inversion procedure tend to demonstrate the stability of the method and its independence of initial values. As mentioned in section 3.5, the total uncertainty from the RTM and instrument errors is about 4-8 K.

The statistical difference between retrieved and observed T_b's (DT_b) obtained from the retrieval of total 1646 data points are presented in Table 3.7. The magnitude and sign of the differences depends upon the frequency and the observed situation (e.g., stratiform, convective, or no rain). Because there is theoretically no interaction with water particles, it may be considered roughly that the no-rain situation represents an estimation of the error of instrument calibration, of sea surface and atmospheric characteristics (sea surface wind speed, vertical profiles of temperature and relative humidity). In this dataset, no rain samples are mostly from the eye region of Hurricane Erin. Because the large variation of sea surface wind speed in eye regions and the large sensitivity of the simulated brightness temperatures at low frequencies to the wind speed as discussed in section 3.5, it is not surprising that the absolute mean and standard deviation of the differences are around 10-15 K at 10, 19, 37 GHz. In addition, the no rain situations in this study are not precisely

Table 3.7. Statistical results for the differences between retrieved and observed T_b's. Here DT_b stands for $T_{bretrieved} - T_{bobserved}$ and $\sigma\, DT_b$ stands for standard deviation of the above-mentioned difference.

Total number of samples (1646)	No rain (185 samples)	Stratiform (1220 samples)	Convective (241 samples)
Mean $DT_{b\,10}$	-10.09	-0.40	-1.57
Mean $DT_{b\,19}$	-10.82	1.66	-1.68
Mean $DT_{b\,37}$	-12.15	-4.03	-5.28
Mean $DT_{b\,85}$	-5.44	2.64	-0.18
σ $DT_{b\,10}$	11.29	5.53	7.25
σ $DT_{b\,19}$	12.66	5.65	7.70
σ $DT_{b\,37}$	15.55	6.61	8.04
σ $DT_{b\,85}$	5.71	3.81	4.49

identifiable and thus can be cloudy or slightly precipitating, which adds more uncertainties.

All DT_b's in stratiform and convective regions are below 7-8 K, within the total uncertainty of RTM and instrument errors. The absolute mean values and standard deviations of DT_b's in convective situations are mostly larger than those for stratiformsituations, showing that there are the more variations of microphysics characteristics in convective conditions and it is harder to simulate. Among these frequencies, the 37 GHz T_b is the most difficult one to be adjusted because this channel is influenced by both rain emission and ice scattering, so it is highly sensitive to simulation errors. The melting layer crudely taken into account in this simulation may lead to a systematic error. However, the T_b's at 10 and 85 GHz are the ones that correspond to the best fit, whatever the considered situations. This result is probably due to the fact that the 10 GHz channel is only sensitive to the rain emission and the 85 GHz frequency is essentially sensitive only to the ice precipitation and therefore they are easy to adjust.

3.6.3 Comparisons of IWC and N_0 Retrievals with Aircraft *In Situ* Measurements and Radar-Only Retrievals

Several factors make it difficult to make comparisons of remotely obtained precipitation microphysical parameters with direct *in situ* measurements from aircraft. First, the sample volumes are vastly different. At a normal DC-8 aircraft speed of 210-245 m/s, the 2D-C and 2D-P probes sample the air at the rate of 0.007 m^3/s and 1 m^3/s respectively (Heymsfield et al. 2004b). So it takes about 2.5-min to sample 1 m^3 air. For EDOP, the sample volume for each pulse at 11 km altitude (the normal DC-8 flight

height during CAMEX-4) is about $2x10^6$ m^3. AMPR samples the whole layer of the precipitation in its beam-width, so the sample volume is much larger than for EDOP. Compared with aircraft measurements, the results from aircraft remote sensing are averaged over a much larger volume. Second, it is very difficult to get exact matching ER-2 and DC-8 flight tracks for both distance and time. We carefully choose EDOP and DC-8 flight tracks that match with each other closely in distance (mostly within 1-2 km for the 627 collocated samples), but with the time differences up to 4-min. The inhomogeneous nature and the time evolution of the precipitating clouds, especially in convective cores, makes the different sample volumes a serious problem for intercomparison purposes. The third difficulty arises from the large variation of ice particle densities, which makes the estimation of bulk parameters, such as IWC, from the size distribution measurements subject to uncertainties. In this study, the analysis of aircraft size distribution data is provided by Dr. Andy Heymsfield, who uses an assumption of density-diameter relationship derived by Heymsfield et al. (2002a) to calculate the IWC. The uncertainty of this IWC estimate is about 25% as given by Heymsfield et al. (2002b). The fourth difficulty is mainly related to the different physical interpretation of retrieved and aircraft measured N_0 . In our retrieval, N_{0s} and N_{0g} are assumed to be constant vertically for each profile. So they represent the average value in the whole profile. In stratiform regions, only N_{0s} is retrieved, while both N_{0s} and N_{0g} are obtained in convective regions. But N_0 derived from aircraft in-situ measurements corresponds to a fixed altitude and represents the PSD characteristics at this height. In addition, the fitting procedure to derive N_0 from the aircraft size distribution

measurements could fail because of the very low correlation coefficients for a few points. The N_0 derived from the exponential PSD fitting is used in this study.

Despite the uncertainties in aircraft measurements and difficulties inherent in sampling the same cloud volume with 2D probes and aircraft remote sensors, comparisons between retrieved results with *in-situ* measurements are widely used to judge the performance of algorithms (Mace et al. 1998; Wang and Sassen 2002a; Skofronick-Jackson et al. 2003). However, an awareness of the limitations helps us better understand the differences in the results from aircraft and remote sensing measurements. The traditional point-to-point comparison is based on the assumption that they have sampled the same cloud volume. The statistical comparisons, such as probability density function (PDF), have the advantage that minimizes the sample volume issues. Both approaches will be used to make IWC comparisons, but only the latter will be used for N_0 comparisons because the physical meaning between retrieved and measured N_0 is different.

Fig. 3.12 shows the scatter plot of radar-radiometer retrieved and radar-only estimated IWC versus 2D probes derived IWC at DC-8 flight altitude from 8.5 to 11 km for the 627 samples in the EDOP-AMPR-PMS dataset. From Fig. 3.12a, the mean difference (MD) of retrieved and 2D derived IWC is very small, only 0.006 g/m^3, and the standard deviation (STD) is 0.195 g/m^3. But the correlation coefficient is only 0.75; a lot of scatter might be due to the mismatch of the two airplanes and the very different sample volumes.

For comparison, Fig. 3.12b is same as Fig 3.12a, but y-axis is for the IWC derived by the radar-only Z-M method. It is apparent that the radar-only method, with a MD of

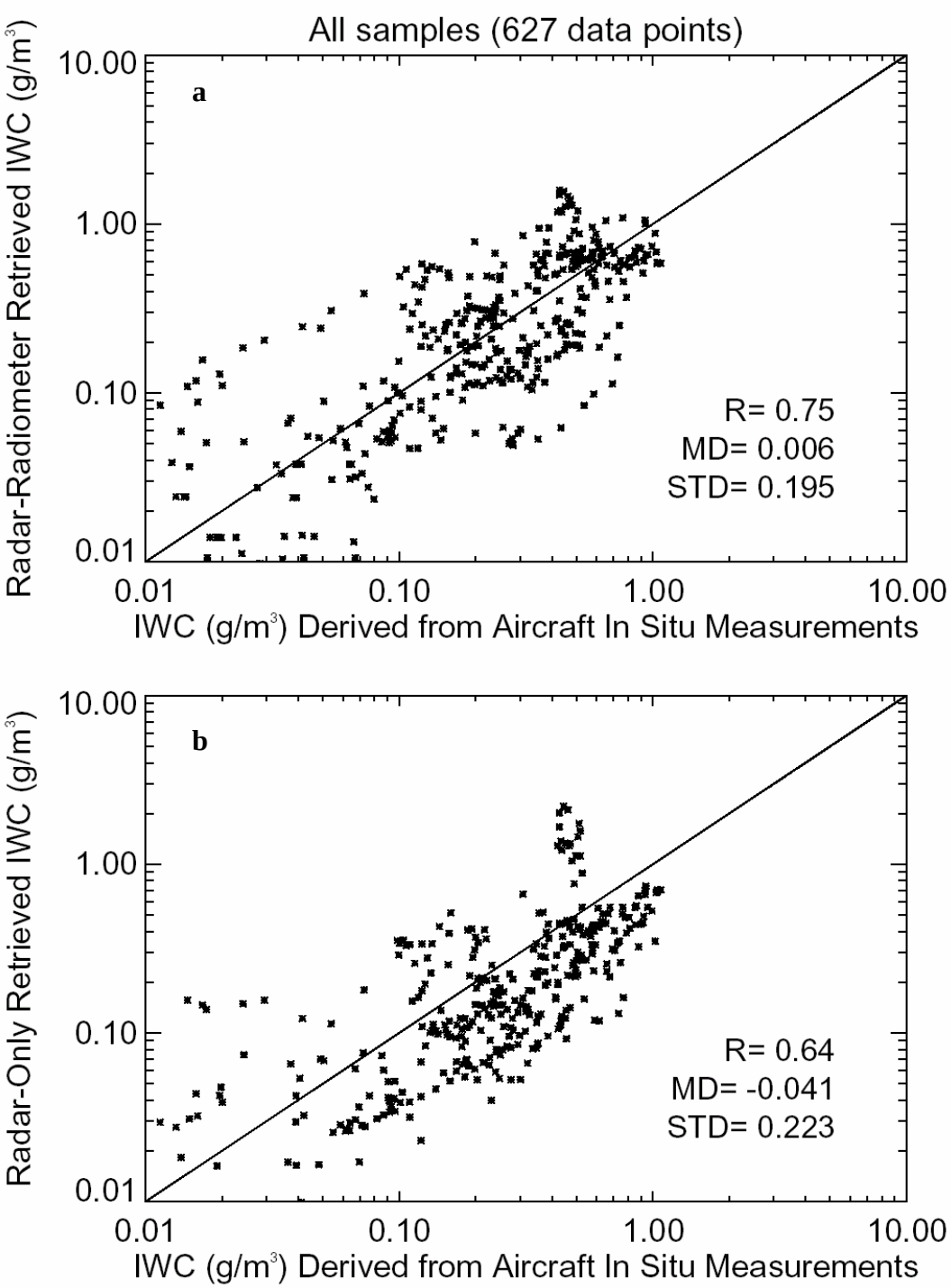

Figure 3.12. Comparisons of radar-radiometer (a), radar-only (b) retrieved and 2D probes derived ice water content for all matched samples at DC-8 flight altitude. Correlation coefficient R, mean difference MD, and standard deviation (STD) are indicated.

-0.041 g/m^3, systematically underestimates the IWC comparing to 2D probe measurements and the combined radar-radiometer retrievals. As the classical Z-IWC relation in hurricanes, Black's (1990) regression was obtained from very limited aircraft datasets at flight altitude about 6 km; it is impossible to represent all the situations in nature. However, the EDOP in 3.2 cm wavelength has a tendency of missing some of small ice particles that could be detected by the AMPR high frequency channels (85 GHz equivalent to 3.52 mm wavelength). The combined radar- radiometer algorithm adjusts the PSD for each profile to obtain a best agreement with radiometer observations; this kind of physical adjustment represents a promising improvement over radar-only empirical retrievals.

To check the effect of mismatch on the comparisons, Fig. 3.13 shows the same comparisons as in Fig. 3.12, but only for the samples with ER-2 and DC-8 matching with each other within 1 km in distance and 1 min in time. The comparison is clearly less scattered. From Fig. 3.13a, a higher correlation coefficient (0.85) and lower MD (-0.004 g/m^3) and STD (0.18 g/m^3) are also obtained, which confirms the spatial and temporal variation of the precipitation clouds. From Fig. 3.13b, however, the underestimate of the radar-only method is more severe for these 192 within 1km/1min samples.

Considering the uncertainties in calculating IWC from *in situ* samples and the limitations of the comparison discussed above, we can conclude from Fig. 3.12a and Fig. 3.13a that the agreement between radar-radiometer retrieved and aircraft measured IWC is reasonably good.

Now let us examine the retrieval performance for different rain types. Fig. 3.14 shows the point-to-point comparison between retrieved and 2D probes measured IWC for

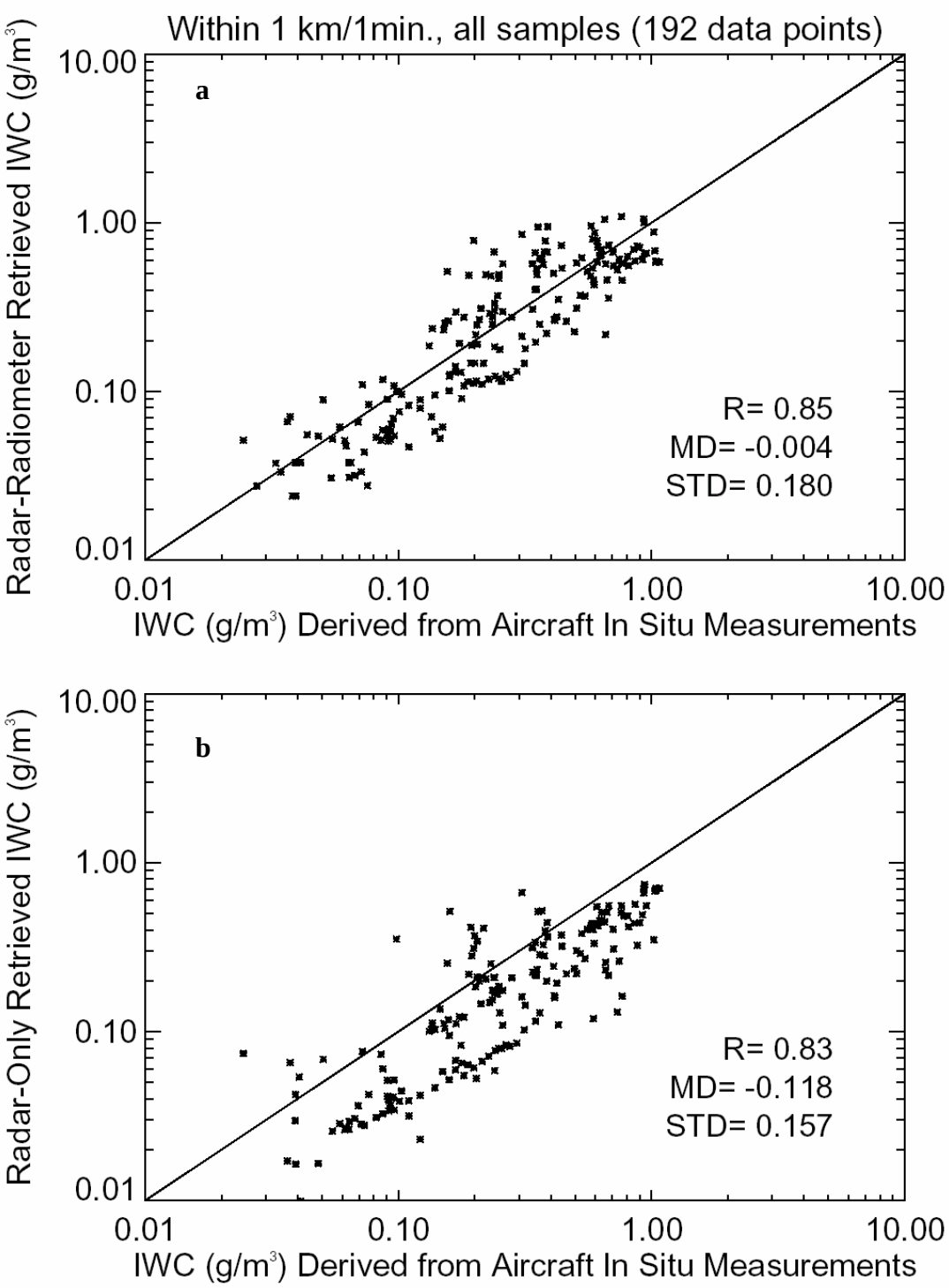

Figure 3.13. Comparisons of radar-radiometer (a), radar-only (b) retrieved and 2D probes derived ice water content for samples with ER-2 and DC-8 matching with each other within 1 km in distance and 1 min in time at DC-8 flight altitude. Correlation coefficient R, mean difference MD, and standard deviation (STD) are indicated.

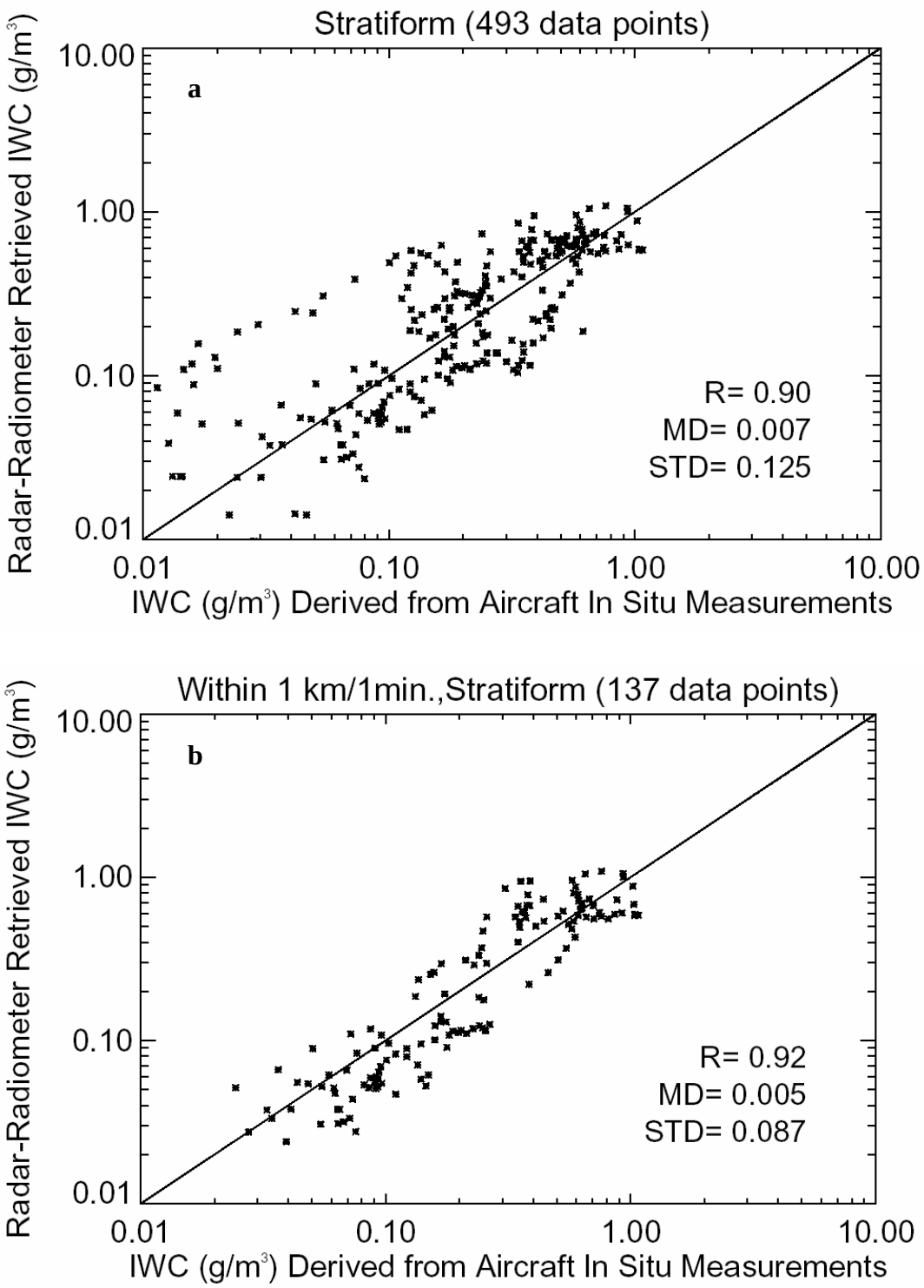

Figure 3.14. Comparisons of radar-radiometer retrieved and 2D probes derived ice water content at DC-8 flight altitude for (a) all stratiform samples and (b) ER-2/DC-8 matching within 1 km/1 min stratiform samples. Correlation coefficient R, mean difference MD, and standard deviation (STD) are indicated.

stratiform situations for both the 493 samples from the original 627 total samples and the 137 samples from the total 192 within 1km/1min samples. The correlation coefficients are 0.9 and 0.92, respectively, the MDs are 0.007 and 0.005 g/m^3, and the STDs are 0.125 and 0.087 g/m^3, respectively. Even in stratiform regions, the inhomogeneous nature is obvious because the comparison in Fig. 3.14a is more scattered than that in Fig. 3.14b; and the standard deviation is larger too. However, the higher correlations and lower standard deviations than those for the total samples shown in Fig. 3.12a and 3.13a mean that the radar-radiometer retrieval has a better performance in stratiform situations.

The comparisons between retrieved and 2D probes derived IWC for convective situations for both the original samples and the within-1km/1min samples are shown in Fig. 3.15. In general, there is a lot of scatter in convective regions, although it is a little bit better for the within 1 km/1min samples, but the improvement is small. The correlation coefficients are only 0.47 and 0.66, respectively, while the standard deviations are high (up to 0.354 and 0.193 g/m^3). Considering the nature of life cycle and dimension characteristics of convective cells (only several minutes and several kilometers), this result is not surprising. The different sample volume issue is maximized in this condition. At the same time, the snow/graupel fraction assumption in our algorithm also contributes some uncertainties in convective regions.

The point-to-point comparison is largely limited by the different sample volume and mismatch issues as discussed above. Now we can make comparisons statistically by looking the frequency distributions to minimize the different sample volume problems. Fig. 3.16 shows the PDFs of the radar-radiometer retrieved, radar-only estimated, and 2D probes derived IWC for all the 627 samples. The underestimate of the radar-only IWC is

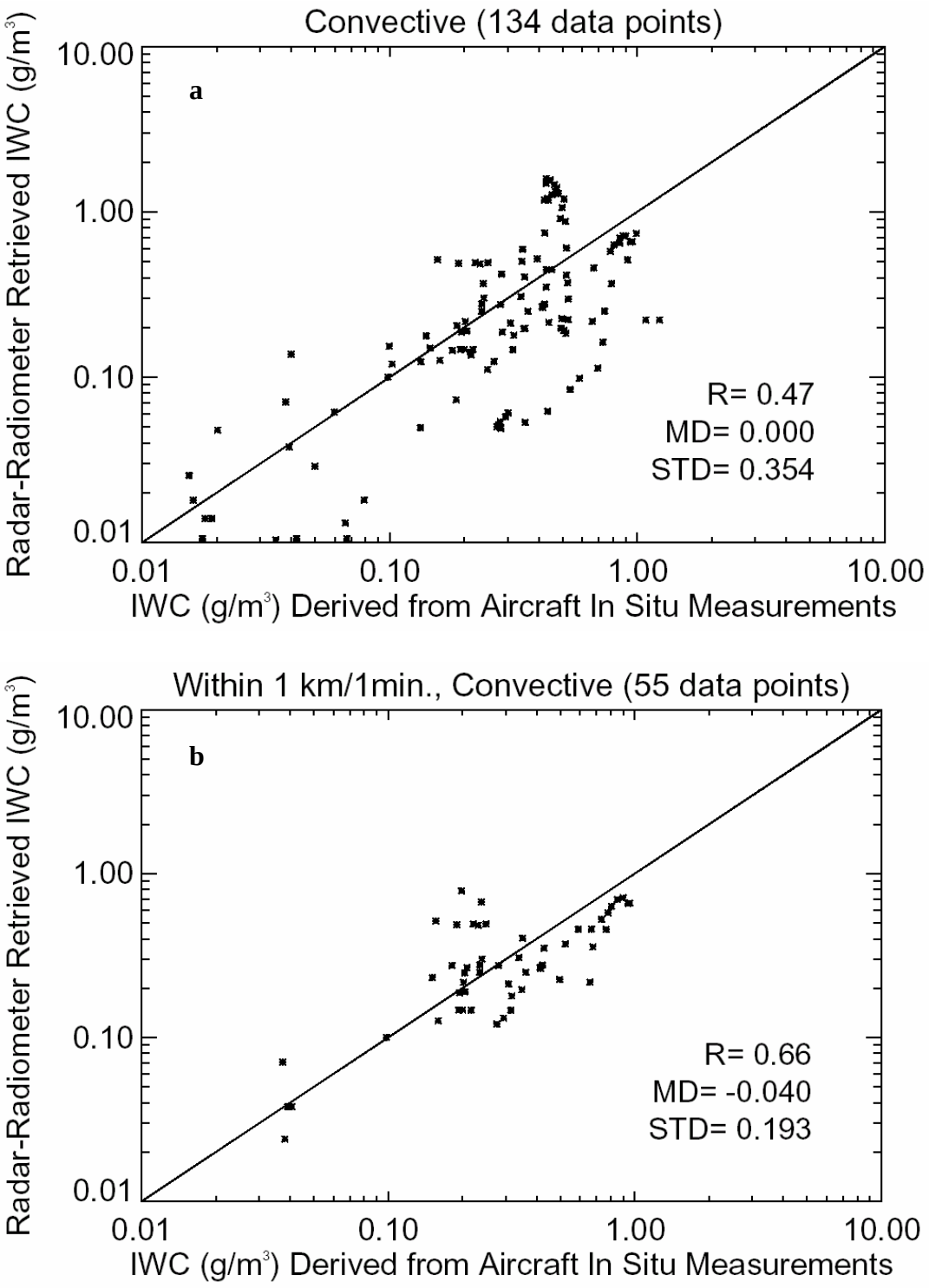

Figure 3.15. Comparisons of radar-radiometer retrieved and 2D probes derived ice water content at DC-8 flight altitude for (a) all convective samples and (b) ER-2/DC-8 matching within 1 km/1 min convective samples. Correlation coefficient R, mean difference MD, and standard deviation (STD) are indicated.

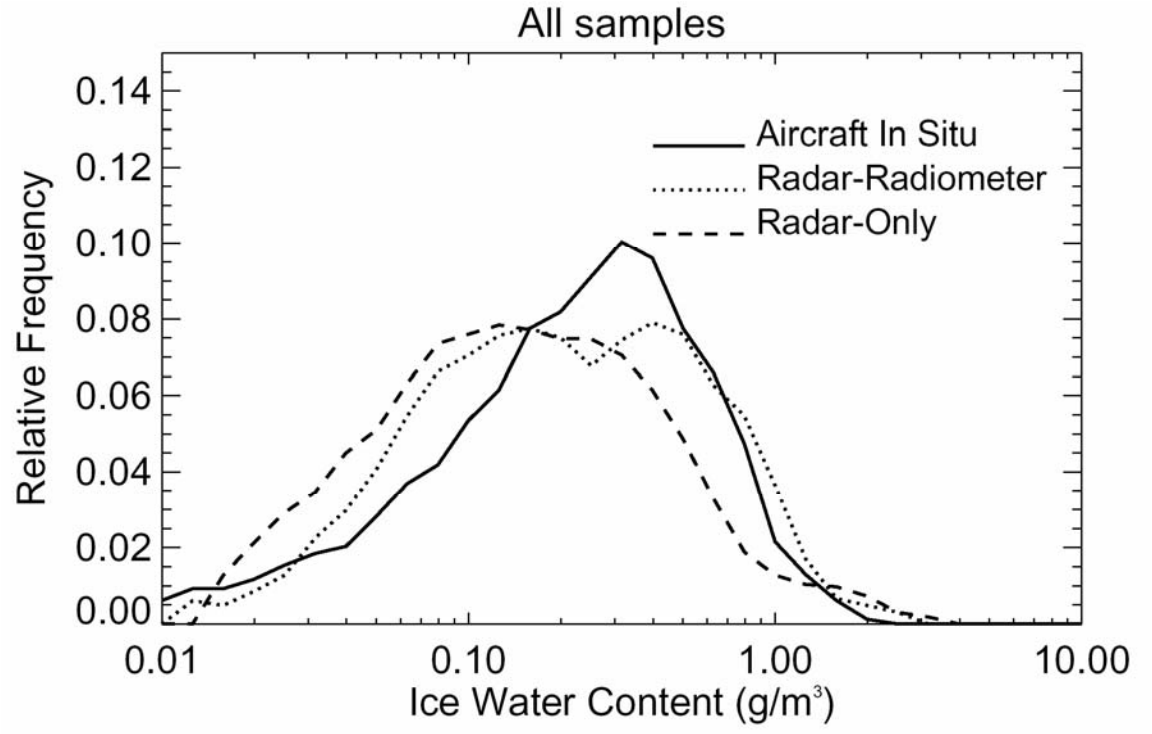

Figure 3.16. PDFs of radar-radiometer retrieved, radar-only estimated, and 2D probes derived IWC for all the 627 samples.

still obvious. But the PDFs of IWC derived from two remote sensing methods tend to be more spread than that of 2D-probes derived IWC. Fig. 3.17 shows the PDFs for stratiform and convective samples respectively. The separation of rain types make the differences easy to explain. Again, in stratiform regions, radar-radiometer retrievals have a good agreement with the aircraft *in situ* measurements, and the spread frequency distribution mainly comes from convective samples. Considering the advantage of statistical comparison, we conclude that this variation is mainly from the uncertainties caused by the snow/graupel fraction assumptions in the radar-radiometer algorithm.

By comparing with aircraft *in situ* observations by both approaches, it is clear that the combined radar-radiometer algorithm has a quite good performance in stratiform situations. In convective precipitation, although there is no systematic under- or over-estimation, the retrievals tend to have large variations around *in situ* measurements. It can partly be explained by the mismatch and different sample volume issues in these comparisons, but the main reason is the assumptions in the algorithm.

The N_0 comparisons are shown in Fig. 3.18. Fig. 3.18a shows the PDFs of retrieved N_0 for snow and measured N_0 for stratiform samples. The 0.5 order of magnitude of the N_0 difference is not surprising considering the limitations discussed in the beginning of this section 3.6.3 and the large range variation of N_0 itself. At the typical DC-8 altitude of 11 km, a lot of small ice particles are expected, therefore a large N_0 ; but the retrieved N_0 is much smaller as shown in this figure because it is an average value for the whole ice layer. Bigger particles in a smaller amount are expected in the low level of the ice part of the precipitation cloud, which makes the average N_0

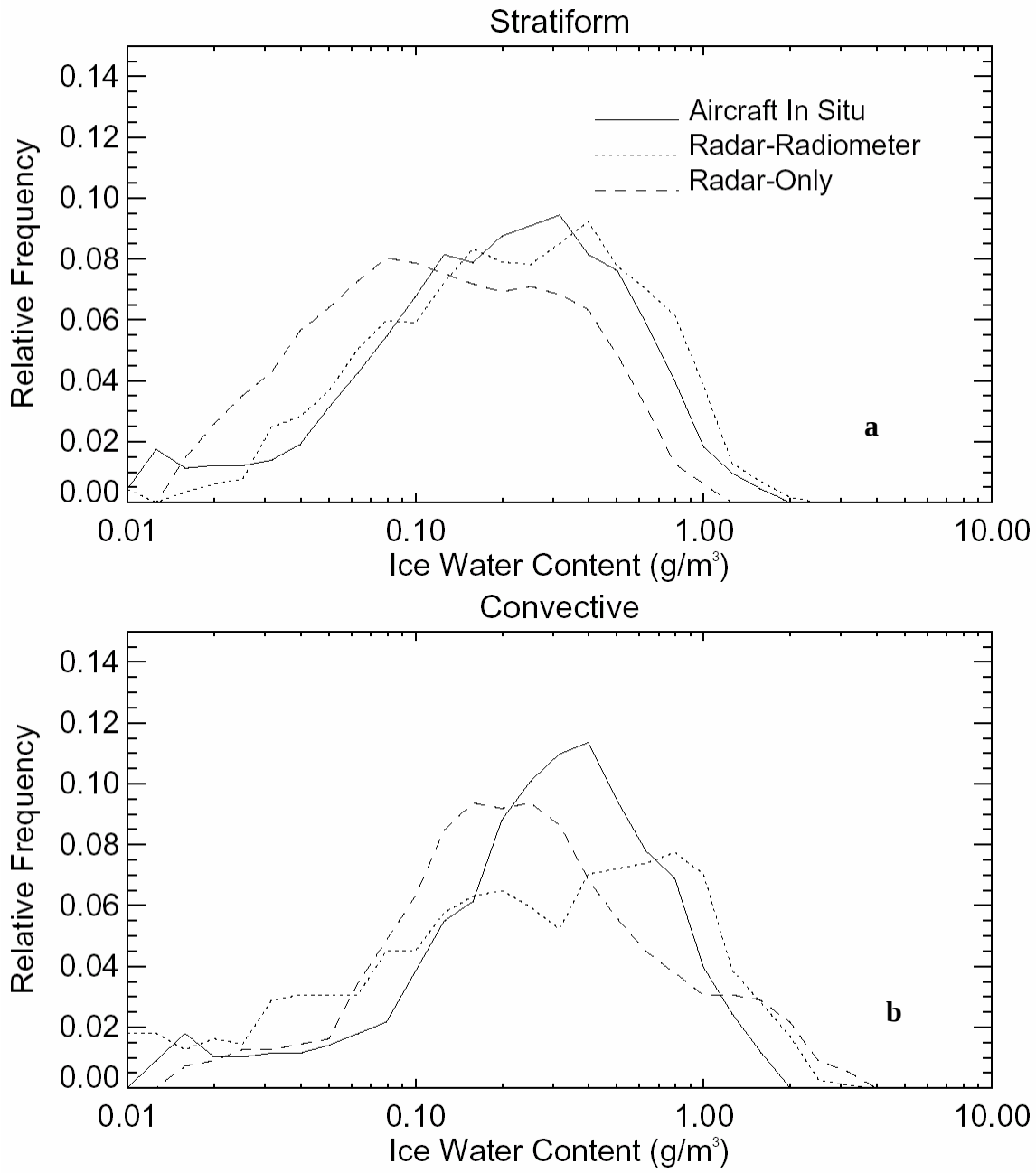

Figure 3.17. PDFs of radar-radiometer retrieved, radar-only estimated, and 2D probes derived IWC for (a) stratiform and (b) convective samples, respectively.

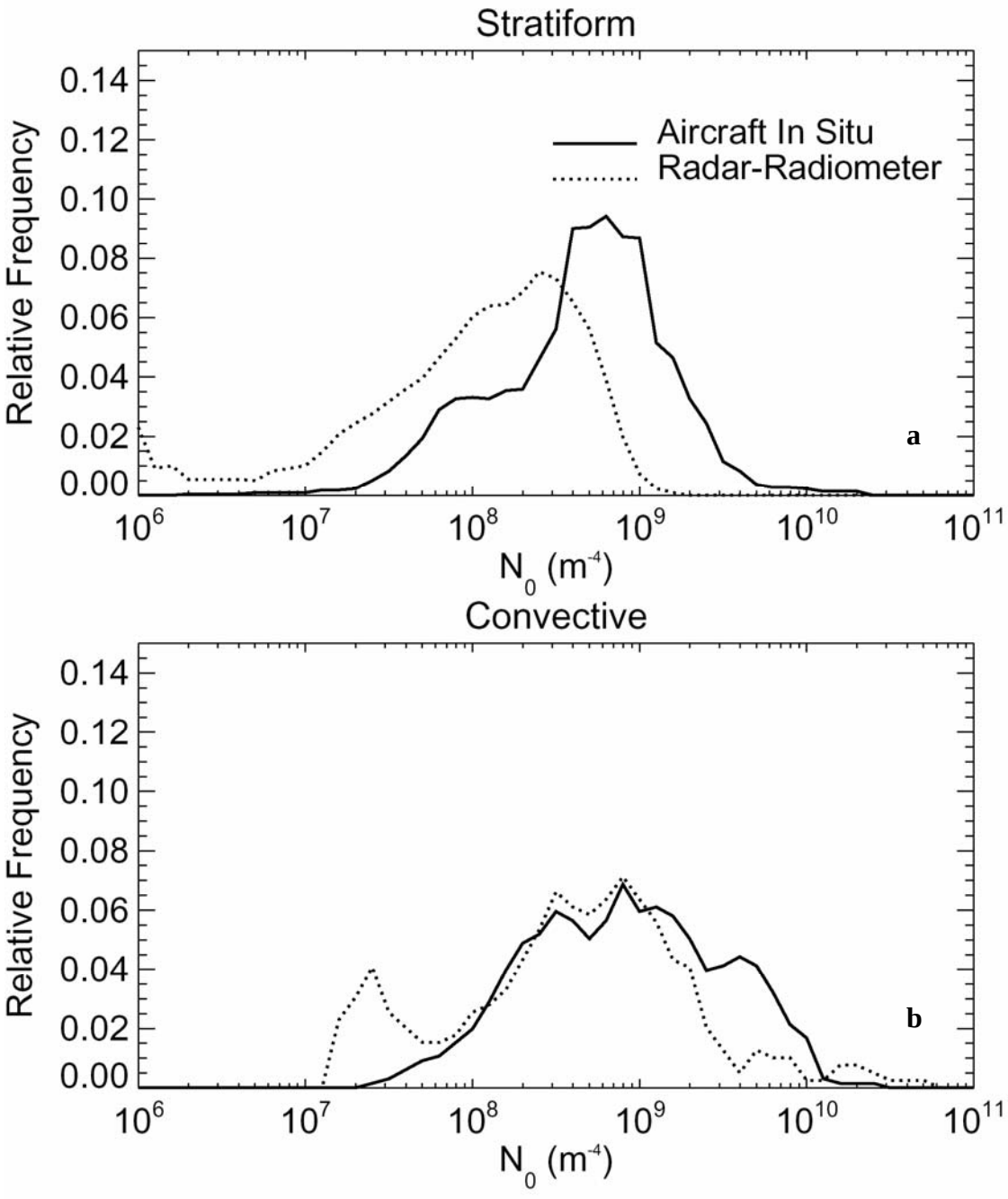

Figure 3.18. PDFs of retrieved and measured N_0 's. (a) PDFs of retrieved N_0 for snow and measured N_0 for stratiform samples, (b) PDFs of retrieved N_0 for snow and graupel (see the text for detail) and measured N_0 for convective samples.

much smaller. Fig. 3.18b shows the PDFs of retrieved N_0 for snow and graupel and measured N_0 for convective samples. For the PDF of the retrieved N_0 , the first peak at about $2*10^7$ m^{-4} represents the distribution of N_{0g} , while the second peak is the distribution of N_{0s} . In our retrieval scheme, for convective regions, snow is assumed to be at upper layers around 12 km, while graupel is at lower layers around 6 km. So the magnitude of retrieved N_{0s} is comparable with that of measured N_0 (at about 11 km) as shown in Fig. 3.16b. But the N_{0g} has a much smaller magnitude.

3.6.4 Comparisons of 50 GHz Brightness Temperature Calculations with HAMSR Observations

Although the sensitivity test in section 3.5 using RTM simulations has shown that the 50 and 52 GHz channels are sensitive to the hydrometeors, especially in convective regions, we still carefully check the HAMSR observations to see if the actual T_b variations in these channels are large enough. Fig. 3.19 shows the scatter plot of HAMSR observed 50 and 52 GHz T_b's versus AMPR observed 85 GHz T_b for stratiform samples and convective samples in the EDOP-AMPR-HAMSR dataset during 3 flights of the Hurricane Erin on Sept. 10, 2001. In convective regions, as T_b85 varies from 225 K to 285 K with storm intensities, T_b50 varies from 245 K to 285 K, while T_b52 varies only from 250 K to 275 K. The 40 K and 25 K variation at 50 and 52 GHz is larger than the simulation error (about 10 K) as discussed above. But in stratiform regions, a 30 K and 18 K variation at 50 and 52 GHz is found as T_b85 varies from 230 K to 290 K. The 18 K variation is unacceptable. As it is found in the sensitivity test, 52 GHz T_b shows much

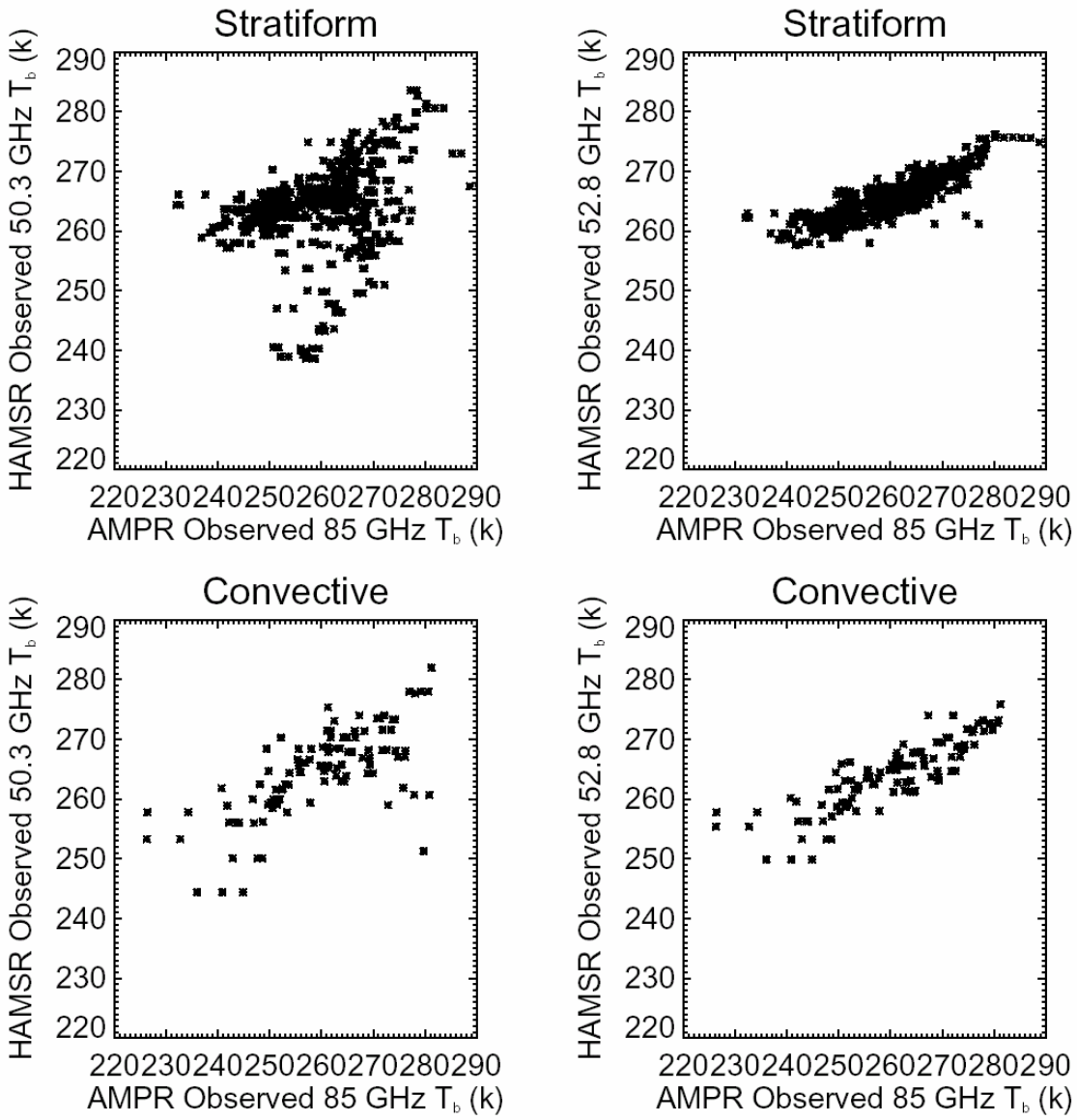

Figure 3.19. The scatter plot of HAMSR observed 50 and 52 GHz T_b's versus AMPR observed 85 GHz T_b for stratiform samples and convective samples in the EDOP-AMPR-HAMSR dataset during three flights of the Hurricane Erin on Sept. 10, 2001.

less sensitivity on hydrometeor radiation, because of contamination by the oxygen emission. So we only use the 50 GHz channel as an independent validation source because it belongs to the outermost wing of the 50-60 oxygen bands. A similar validation at 50 GHz was used in Skofronick-Jackson et al. (2003)

To make a direct comparison with the independent measurement at 50 GHz, we have calculated T_b50 from the RTM using as input the set of retrieved hydrometeor profiles and N_0 's for the 1019 EDOP-AMPR-HAMSR matched samples during three Hurricane Erin flights. Fig. 3.20 shows the point-to-point comparison between observed and retrieved 50 GHz T_b's for stratiform and convective samples. The qualitative agreements is good, the absolute mean differences are less than 10 K. The mean difference depends on the considered situation: –2.4 K for stratiform regions and –1.7 K for convective regions. The bias is always negative, indicating a weak underestimate of the retrieved T_b50. But notice that the underestimates are mainly in high brightness temperature regions (greater than 270 K). Checking the dataset, these points are mainly located around the eye region. They might be biased by the uncertainties of the sea surface temperature and wind speed. The standard deviation of the Tb difference is 3.7 K in stratiform regions, and it increases to 4.5 K in convective regions. Again, this is due to uncertainties caused by the snow/graupel fraction assumption in the algorithm.

Nevertheless, the global agreement of the measured and retrieved brightness temperatures at an independent channel allows us to consider that both the inversion procedure and the retrieved parameters are consistent with the 50 GHz observations.

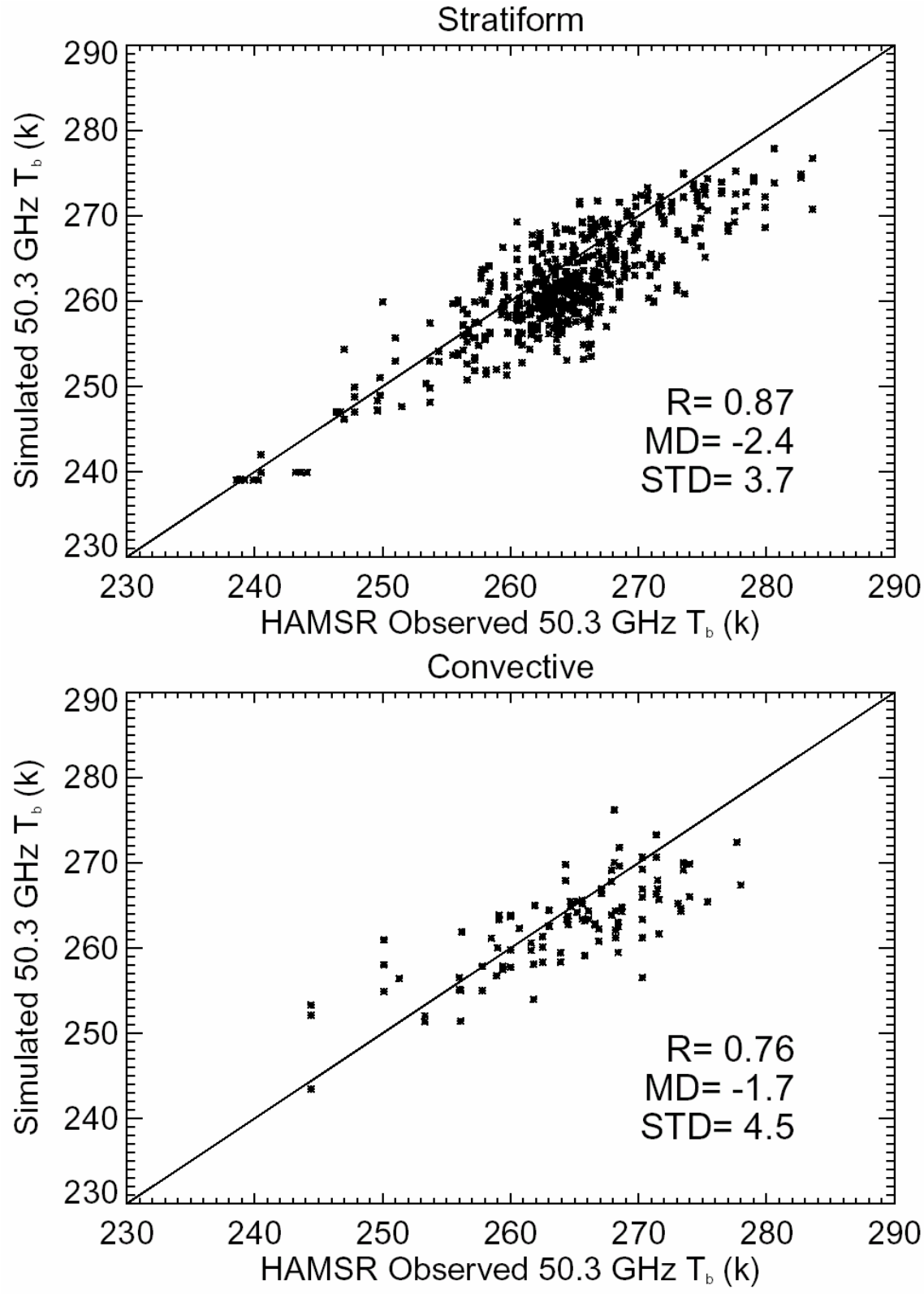

Figure 3.20. The point-to-point comparison between observed and retrieved 50 GHz T_b's for stratiform and convective samples.

3.6.5 Comparisons of LWC and Surface Rain Rate Retrievals with Radar-only and Radiometer-only Retrievals

Above we have compared the retrieved IWC, N_0 , and 50 GHz brightness temperature with independent measurements. The combined radar-radiometer algorithm also has the ability to retrieve the LWC profile and therefore to derive the surface rain rate. But there are no direct measurements in this CAMEX-4 dataset available to evaluate LWC and rain rate retrievals. However, radar-only and radiometer-only algorithms can be compared. Comparisons between different algorithms will help us understand the advantages and disadvantages of the various algorithms.

An easy-to-apply radar-only algorithm to estimate LWC is the empirical Z-LWC relationship. Here the radar-only Z-M algorithm mentioned in section 3.2.2 is used. The Z-LWC relationship shown in (3.1) is given by Willis and Jorgensen (1981), which was derived from aircraft measurements of hurricane raindrop spectra at altitude less than 3 km. This relation corresponds to Z-R relation (R in mm/hr) of:

$$Z = 300R^{1.35}, \tag{3.19}$$

which is given by Willis and Jorgensen (1981) and Jorgensen and Willis (1982) and widely used for the hurricane situation. This relation is for both stratiform and convective regions in hurricanes. Jorgensen and Willis (1982) and Houze et al. (1992) find that in hurricanes, on average the raindrop size distribution is mixed by the strong horizontal winds and that no significant difference exists between stratiform and convective situations. Results described in Chapter 2 provide same independent certification of this conclusion.

Fig. 3.21 provides a comparison of LWC retrieved by the combined algorithm and the radar-only algorithm using (3.1), based on the seven-flight dataset. 2-D frequency maps rather than scatter plots are used, given the large number of points considered in this analysis. The radar-radiometer estimates and radar-only estimates are well correlated. From Fig. 3.21a, in stratiform regions, there is a systematic overestimation of low intensity LWC (less than 0.1 g/m^3) relative to radar-only estimates by the combined algorithm. From Fig. 3.21b, in convective regions, an underestimate of the high intensity LWC by the combined radar-radiometer method is found relative to radar-only method. A possible reason for this disagreement is the PSD variation for stratiform and convective regions, which is not taken into account in the Z-LWC relationship. The nonuniform beamfilling problem (Chiu et al. 1990; Short and North 1990) for the combined algorithm could also cause some underestimation in convective regions since the AMPR's footprint at 10 and 19 GHz is 2.8 km, which is much larger than the EDOP footprint at surface (1.1 km). For very intense convective regions, the EDOP attenuation correction problem could also contribute to this disagreement between the radar-radiometer and radar-only algorithms.

The PDFs of LWCs retrieved by the combined algorithm and the radar-only algorithm are shown in Fig. 3.22 for stratiform and convective regions respectively. The lack of extreme LWC values in the combined radar-radiometer retrievals is obvious for both situations. This is similar as what is found in Fig. 3.21. The mean LWCs derive from the combined and the radar-only algorithm in stratiform regions are 0.171 and 0.166 g/m^3, in convective regions are 0.593 and 0.751 g/m^3, respectively. The total mean values for the two regions (0.22 and 0.23 g/m^3) are very close to each other.

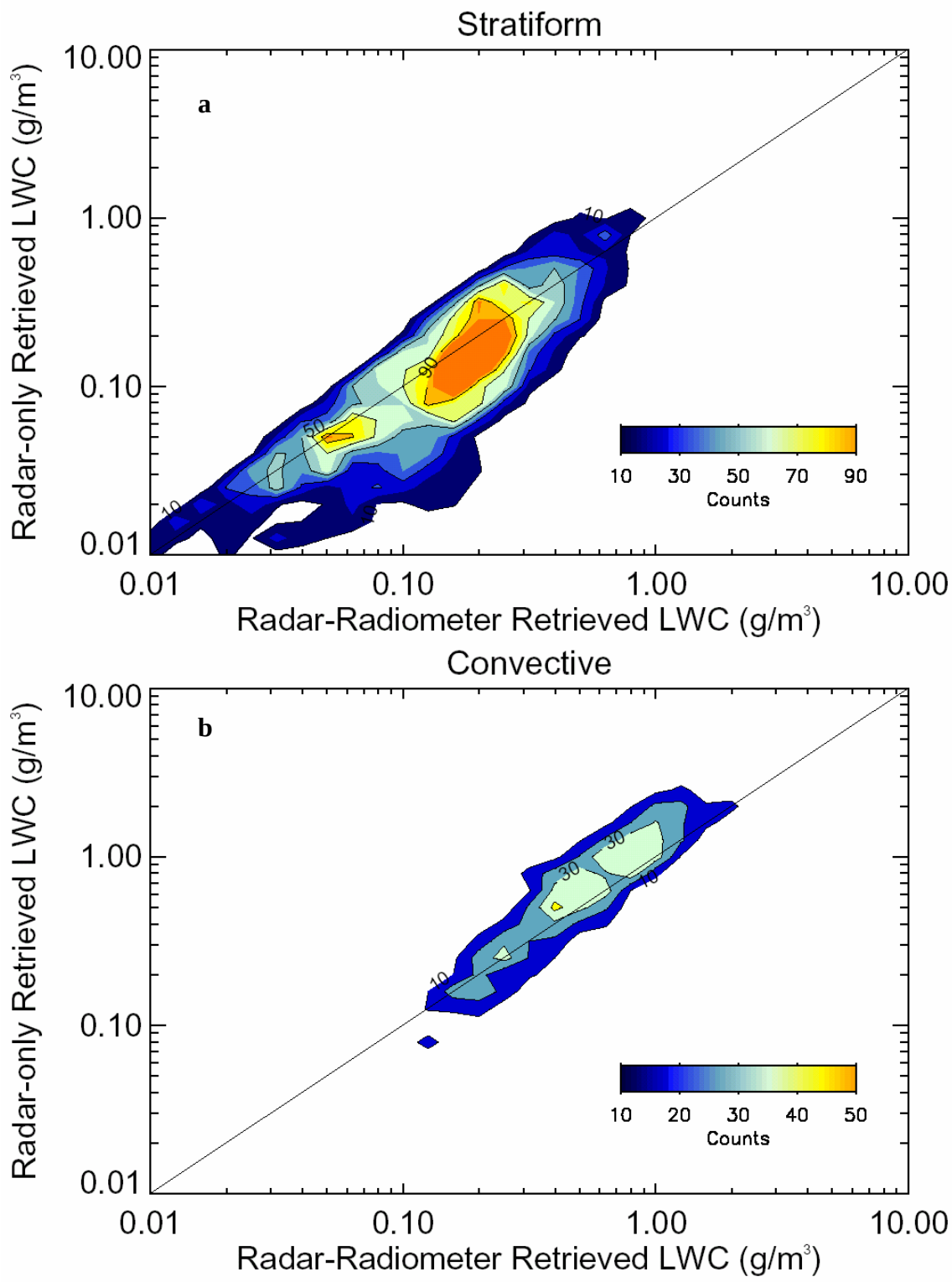

Figure 3.21. 2-D frequency of radar-radiometer and radar-only retrieved liquid water content for (a) stratiform and (b) convective samples.

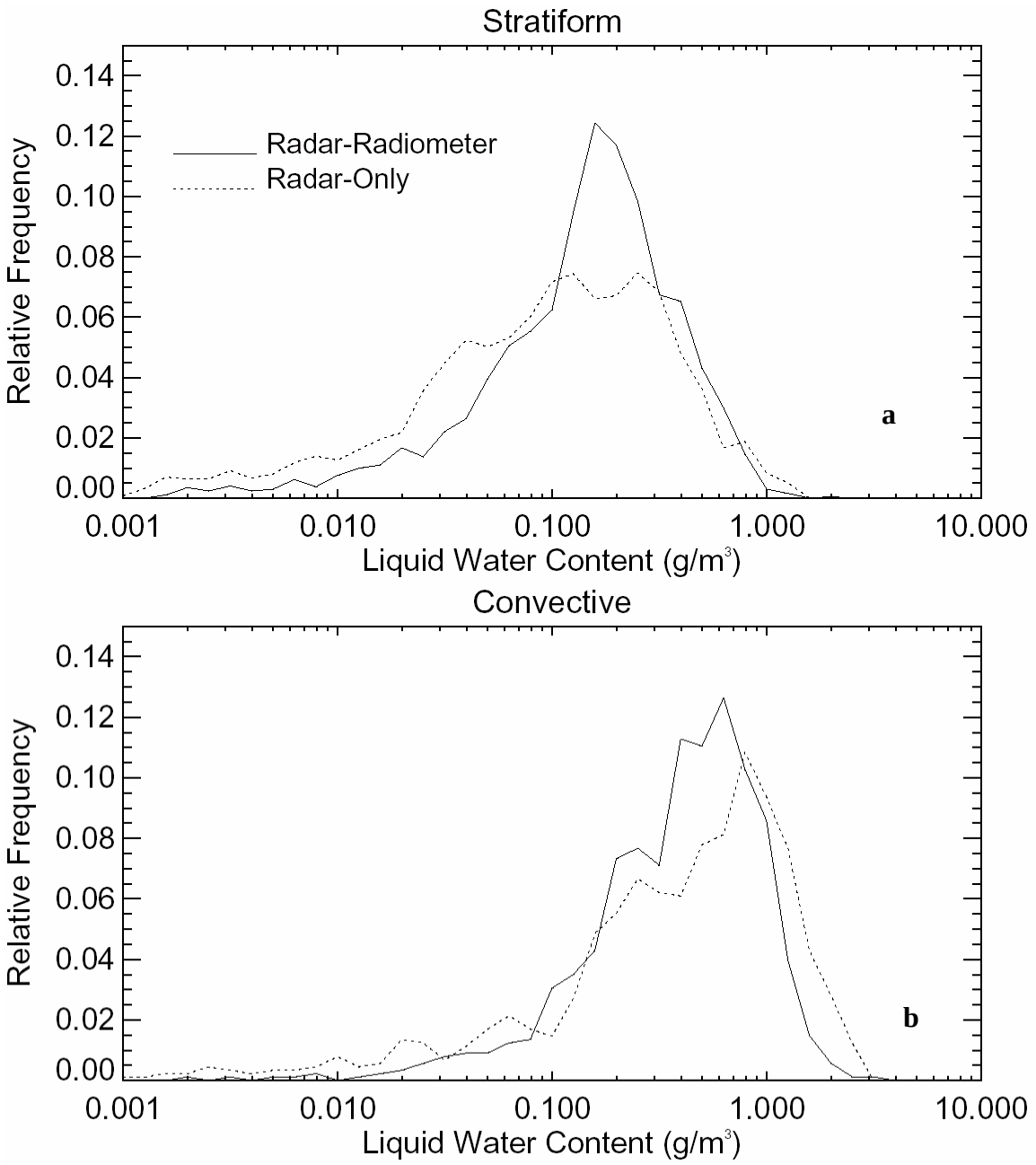

Figure 3.22. PDFs of liquid water contents retrieved by the combined algorithm and the radar-only algorithm for (a) stratiform and (b) convective samples.

The emission-based radiometer algorithm developed by Wilheit et al. (1977) has been used in many studies (Adler and Rodgers, 1977; Chiu et al. 1990; Shin et al., 1990). This algorithm is not designed to retrieve LWC directly, but to calculate surface rain rate from brightness temperatures at low frequencies. Here we will show the comparison of the rain rate retrievals by this emission-based radiometer-only algorithm with the combined algorithm developed in this study. The emission-based technique used in this comparison is that of Chiu et al. (1990):

$$R = -\ln[(274 - T_{b19})/102]/0.19 \quad \text{(mm/hr)} \tag{3.20}$$

where T_{b19} is the brightness temperature at 19 GHz. McGaughey et al. (1996) also give a gross look-up table for estimating of rain rate from AMPR 10 GHz brightness temperature derived from the radiative transfer simulation. This gross rain rate estimate from AMPR 10 GHz observations will also be used for the comparison.

However, direct comparisons cannot be made because the combined algorithm generates liquid water contents while the emission-based method derives the surface rain rates. An equivalent surface rain rate is obtained for the combined retrievals by applying a radar reflectivity-fall speed (Vt) relationship given by Joss and Waldvogel (1970) at near surface:

$$V_t = -2.6Z^{0.107} \quad \text{(m/s)} \tag{3.21}$$

Then rain rate can be expressed by LWC and V_t (Lhermitte 2002):

$$R = 3.6 \times LWC \times V_t \quad \text{(m/hr)} \tag{3.22}$$

Fig. 3.23 shows the comparison of surface rain rates derived by the emission-based radiometer-only algorithm from AMPR 19 GHz observations and the combined algorithm from EDOP and AMPR observations for stratiform and convective regions. These two estimates are well correlated to each other, with correlation coefficient of 0.85 and 0.66 for stratiform and convective regions respectively. It is also seen that for a rain rate less than 10 mm/hr, the two retrievals are in good agreement. But for larger rainfall rates, the retrievals from the emission-based radiometer-only method are underestimated relative to the combined algorithm. Possible reasons for the underestimate of AMPR 19 GHz derived rain rates are 1) There is a nonuniform beamfilling problem by the radiometer-only algorithm because the footprint for AMPR 10 and 19 GHz channel is much larger than that for EDOP; 2) The radiation at 19 GHz actually becomes saturated for a rain rate larger than 10-15 mm/hr.

Because 10 GHz will be saturated at a larger rain rate of about 50 mm/hr (Tesmer and Wilheit 1998; McGaughey et al. 1996), the comparison of surface rain rates derived by the gross look-up table given by McGaughey et al. (1996) from AMPR 10 GHz brightness temperatures and by the combined algorithm is presented in Fig. 3.24. The underestimate of the AMPR 10 GHz rain rate relative to the combined retrieval is more severe than that of the AMPR 19 GHz rain rate. Although the gross look-up table between AMPR 10 GHz brightness temperature and the surface rain rate could contribute some of the uncertainties, we still can rule out the saturation issue by 19 GHz observations. The main reason for the underestimation by the emission-based radiometer-only algorithm is the beamfilling problem. In convective regions, there are more variations in the precipitation intensity in small scales than that in stratiform regions, so

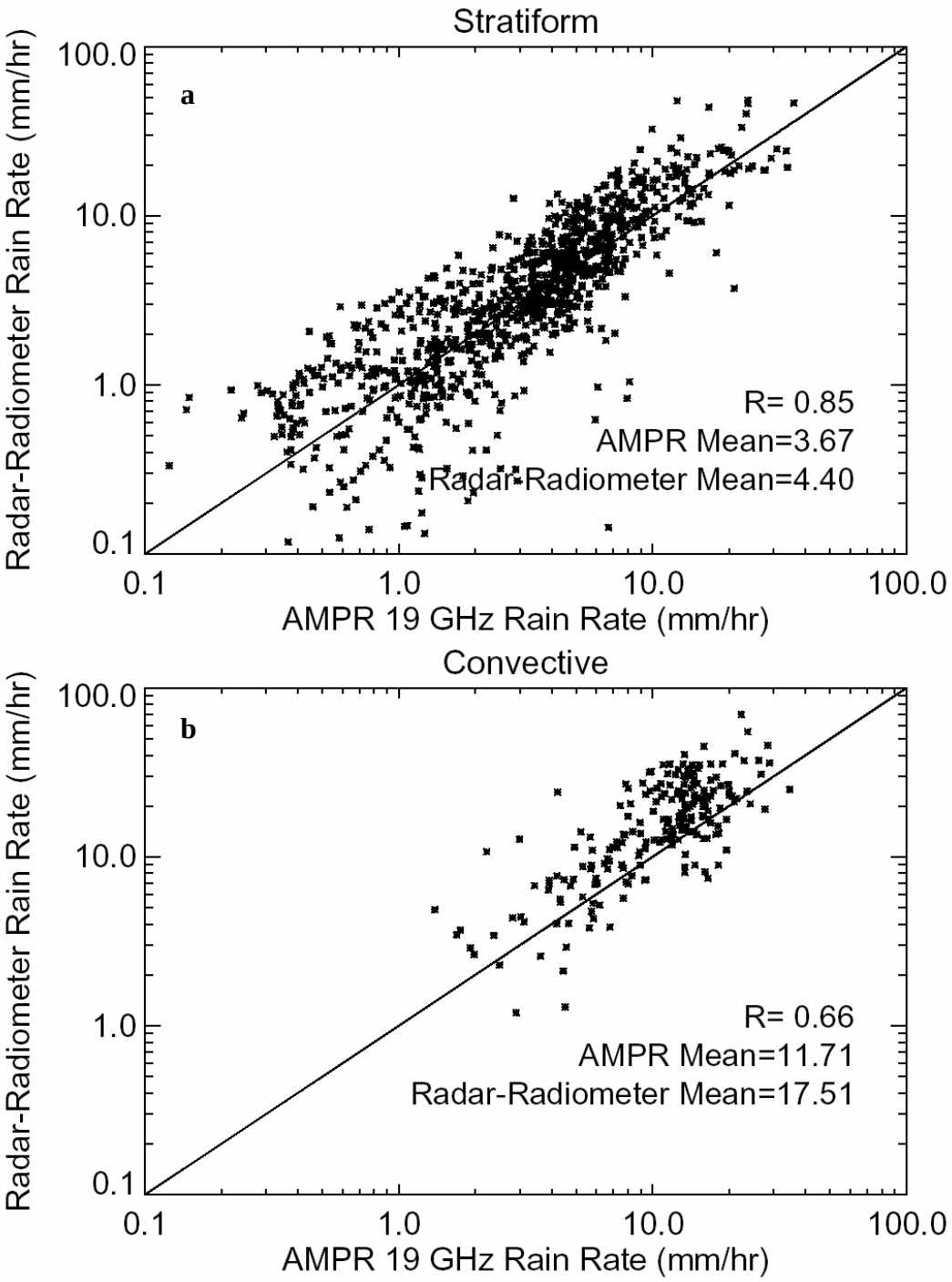

Figure 3.23. Comparisons of surface rain rates derived by the emission-based radiometer-only algorithm from AMPR 19 GHz observations (AMPR 19 GHz rain rate) and the combined algorithm from EDOP and AMPR observations (radar-radiometer rain rate) for (a) stratiform and (b) convective regions.

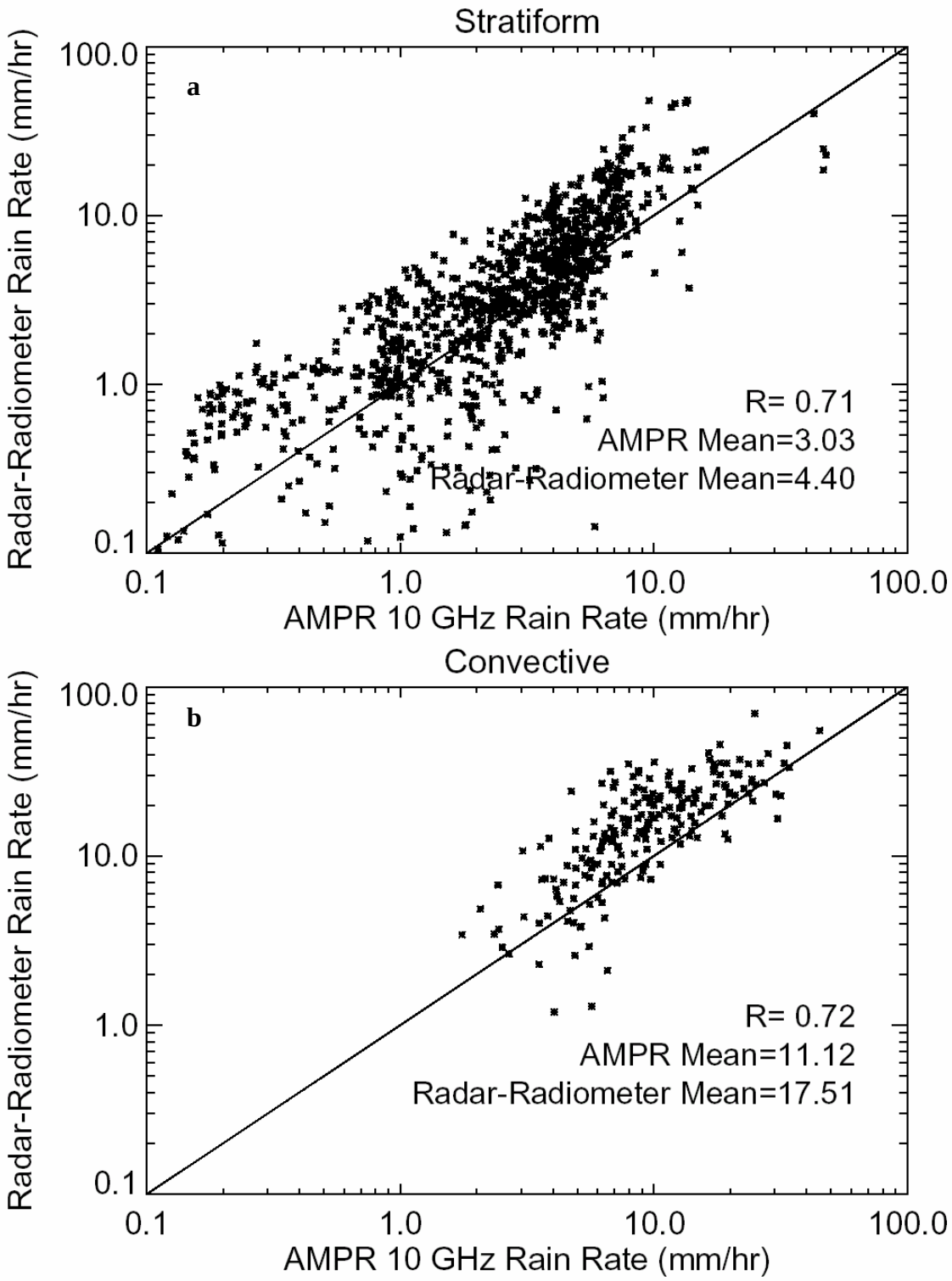

Figure 3.24. Comparisons of surface rain rates derived by the emission-based radiometer-only algorithm from AMPR 10 GHz observations (AMPR 10 GHz rain rate) and the combined algorithm from EDOP and AMPR observations (radar-radiometer rain rate) for (a) stratiform and (b) convective regions.

the beamfilling problem is more severe in convective regions. This can explain that the mean rain rates are close in stratiform rain regions for the three algorithms (4.40, 3.67 and 3.03 mm/hr), but in convective regions, the mean value from the emission-based algorithms (11.71 and 11.12 mm/hr) is much smaller than that from the combined algorithm (17.51 mm/hr). The beamfilling issue will be discussed more in later sections.

3.7 Application to TRMM Observations

TRMM can provide about 700 tropical cyclone overpasses each year, which is impossible coverage for aircraft observations. This tremendous amount of satellite-based observation represents the only way to obtain extensive coverage for tropical cyclones worldwide. Aircraft radar (EDOP) can only sample the cross section of a storm, but the TRMM PR can sample the whole 3-D structure and make it possible to study both the eyewall and rainband features in a storm. In addition to tropical cyclones, other tropical rainfall systems are also observed by TRMM, providing a source for investigating the algorithm performance in different rainfall systems. Therefore, it is very important to implement this algorithm using TRMM observations.

3.7.1 Implementation

For applying the algorithm to TRMM observations, TRMM PR 2A25 attenuation corrected reflectivity profiles and TMI 1B11 brightness temperatures are used as input to the algorithm. PR and TMI observations are matched with each other by a nearest-neighbor matching technique (Nesbitt et al. 2000). As described in section 3.3.2, brightness temperatures observed by TRMM TMI are not from nadir view but from a

view angle of 52.8°, including both horizontal and vertical polarized measurements. When applying the combined algorithm to TRMM observations, the error function (3.18) needs to be reformulated. At 10 and 19 GHz, the *normalized polarization difference* (P) is used instead of the brightness temperature to single out precipitation (liquid water) emission by decoupling it from the impact of scattering and variations in atmospheric temperature, column water vapor, and surface emissivity. P is defined by Petty (1994a,b) as:

$$P = \frac{T_{bV} - T_{bH}}{T_{bV,clear} - T_{bH,clear}} \tag{3.23}$$

where T_{bV} and T_{bH} are the vertically and horizontally polarized brightness temperatures and $T_{bV,clear}$ and $T_{bH,clear}$ are background brightness temperatures interpolated from brightness temperatures in adjacent rain-free area. The use of P in low frequencies is similar to that of Grecu et al. (2004). At 37 and 85 GHz, the Polarization Corrected Temperature (PCT) is used instead of the brightness temperature to minimize the radiometrically cold sea surface scattering effect (notice that Petty (1994a) defined a scattering index S, which has the similar behavior as PCT). PCT is defined by Spencer et al. (1989) as:

$$PCT = (\beta T_{bh} - T_{bv})/(\beta - 1) \tag{3.24}$$

where β is the ratio of T_{bV} warming to T_{bH} warming due to only atmospheric gaseous absorption. As pointed out by Spencer et al. (1989), the absolute accuracy for β is not as important as keeping it constant. For 85 GHz, the value for β is 0.45 (Spencer et al.

1989); for 37 GHz, the value for β is 0.55 (Cecil et al. 2002). Notice that P and PCT have different magnitudes. In the retrieval, a weighting factor is added to (3.18) for each frequency to keep the contribution approximately equivalent from each channel.

The atmospheric parameters such as sea surface wind speed and vertical profiles of temperature and relative humidity are also needed as input to the algorithm. Since there is no direct sounding observation available for TRMM overpasses, NCEP reanalysis data (http://www.cru.uea.ac.uk/cru/data/ncep/) are used.

3.7.2 TRMM Beamfilling Problem and Analysis Method

Unlike aircraft instrumentation, the instruments on TRMM are flying at an above sea surface altitude of about 350 km (402.5 km after TRMM boost during Aug., 2001 for fuel savings) and have relatively large footprints. Table 3.8 gives the comparison of PR and TMI footprints before and after TRMM boost. This “boost” resulted in a decrease in the areal resolution of the sensors by roughly 30 percent. From Table 3.8, the footprints of TMI at 10 and 19 GHz are extremely large compared with AMPR footprints at these channels (2.8 × 2.8 km). Even at 37 and 85 GHz, the footprints are as large as 16 × 9 and 7 × 5 km before boost and 18 × 10 and 8 × 6 km after boost. So the TMI sensor field-of-view (FOV) is large enough to encompass substantial precipitation inhomogeneity. The combination of a nonlinear rain rate (or LWC/IWC)--microwave brightness temperature (or radar reflectivity) relation and the nonuniform rainfall within a FOV results in retrieved rain rates being lower than true rain rates (Chiu et al. 1990; Short and North 1990). This is so-called beamfilling (or nonuniform beamfilling) problem of satellite retrievals (Bell 1987). Chiu et al. (1990) used GATE [GARP (Global Atmospheric

Table 3.8. Comparison of PR and TMI footprints (km × km) before and after TRMM boost during Aug. 2001.

	PR	TMI				
		10 GHz	19 GHz	21 GHz	37 GHz	85 GHz
Before Boost	4.3 × 4.3	63 × 37	30 × 18	23 × 18	16 × 9	7 × 5
After Boost	5.0 × 5.0	72 × 43	35 × 21	26 × 21	18 × 10	8 × 6

Research Program) Atlantic Tropical Experiment] rain-rate data to show that for a footprint size of 40 km, the beamfilling bias is the order of 40% of the actual rain rate, and that the standard deviation of the random beamfilling error is about the same size for an individual retrieval. While many studies have addressed the issue of how to best deal with the beamfilling problem in satellite radiometer-based quantitative precipitation algorithms (e.g., Chiu et al. 1990; Short and North 1990; Petty 1994a,b; Graves 1993; Kummerow and Giglio 1994; Kummerow 1998; Ha and North 1995) and TRMM radar-based rainfall algorithm (Kozu and Iguchi 1999; Durden et al. 1998), it is still an unsolved research issue.

The beamfilling error has not been corrected in the combined algorithm developed in this study. For the CAMEX-4 field program data application, it is not a significant problem. But for the TRMM application, we understand that the beamfilling error could not be neglected and the nonuniform beamfilling would have different effects for stratiform and convective precipitation regions and for LWC and IWC retrievals. For nearly uniform stratiform regions, the beamfilling problem would not be very large because the inhomogeneity of rainfall is minimized. But for convective regions, even the PR footprint size of 4.3 km (5.0 km after TRMM boost) is larger than the typical size of convective rain cells. Sauvageot et al. (1999) reviewed the studies on rain cells (Dennis and Fernald 1963; Miller et al. 1975; Konrad 1978; Goldhirsh and Musiani 1986; and Tenorio et al. 1995) and reported that minimum and maximum diameters of a convective cell are 1-2 km and 18-20 km, respectively, with a mean value of about 2.5 km. A rather small range for the convective cell diameter is defined as 1-5 km by LeMone and Zipser (1980), Szoke et al. (1986), and Lucas et al. (1994). This implies that the rainfall within

PR and TMI footprints may often be highly variable when observing convective rainfall. Therefore the beamfilling error in convective rainfall retrievals would be large. Consider the difference for IWC and LWC retrievals. The IWC retrievals are mainly obtained from the radar and high frequency radiometer observations. Among the TMI high frequency channels, 85 GHz would dominate the IWC estimation. The footprint sizes of PR, and the TMI 85 GHz channel are not larger than 4-8 km. According to Chiu et al. (1990), the rain rate bias is about 25% for a footprint size of 8 km. The error of IWC retrievals would be small. In the rain region, the LWC retrieval might be largely biased by the beamfilling problem considering the large 10 and 19 GHz FOV (60 km and 30 km) and the inhomogeneity of precipitation in hurricanes.

Combining the effects from different rain types and different retrieval parameters, it is reasonable to say that the beamfilling error for IWC in stratiform regions would be the smallest, and that this kind of error for LWC in convective regions would be the largest. Even in convective regions, the beamfilling bias for IWC would not be very large. The problem would be in the LWC retrieval in both stratiform and convective precipitation. So we ask, "*Would the magnitude of the beamfilling bias from the combined radar-radiometer LWC retrieval be as same as that from the radiometer-only LWC retrieval given that the footprint of PR is much smaller than those of the low frequency channels of TMI? How would the beamfilling errors of LWC retrievals be different for different rain type regions?* " We are not attempting to find the absolute beamfilling error, but instead we compare the different beamfilling bias for the combined and radiometer-only algorithm relative to the radar-only algorithm.

Based on the above hypothesis, we carefully choose a hurricane case with wide spread stratiform regions around rainbands and strong convective regions in the eyewall to test the algorithm performance in IWC and LWC retrievals. The case selected is the TRMM orbit on Sept. 08, 2003 for Hurricane Isabel (2003) over the North Atlantic Ocean (orbit number 33151). The retrieval results will be compared with TRMM 2A12 (radiometer-only, Kummerow et al. 1996) and Z-M (radar-only) algorithms (see Section 3.2.3 for details of these algorithms). Retrieval results from 2A25 are also derived but not shown here because the original algorithm developer Dr. Iguchi (personal communication) has confirmed that the PSD assumption of 2A25 in the ice region is very crude and will not be improved until version 7. As checked, the ice water content retrieved from 2A25 for this Isabel orbit is about 1 order of magnitude less than other retrievals (similar results can be seen in Fig. 3.1 and Table 3.2), and the liquid water content retrieved from 2A25 is similar to that from Z-M algorithm.

3.7.3 Case Study for Stratiform Regions in Hurricane Isabel (2003)

Hurricane Isabel (2003) was a long-lived hurricane over the North Atlantic Ocean that reached category 5 on Sept. 11, 2003 and made landfall on North Carolina as a category 2 hurricane on Sept. 18, 2003. Fig 3.25 shows its best track positions during Sept. 6-19. TRMM provided an unprecedented 10 overpasses of Isabel. The orbit that we choose to study here was obtained on 21:55 UTC Sept. 8, during which period Isabel was a category 3 hurricane and in its intensifying stage. The best track maximum sustained surface wind speed is shown in Fig. 3.26.

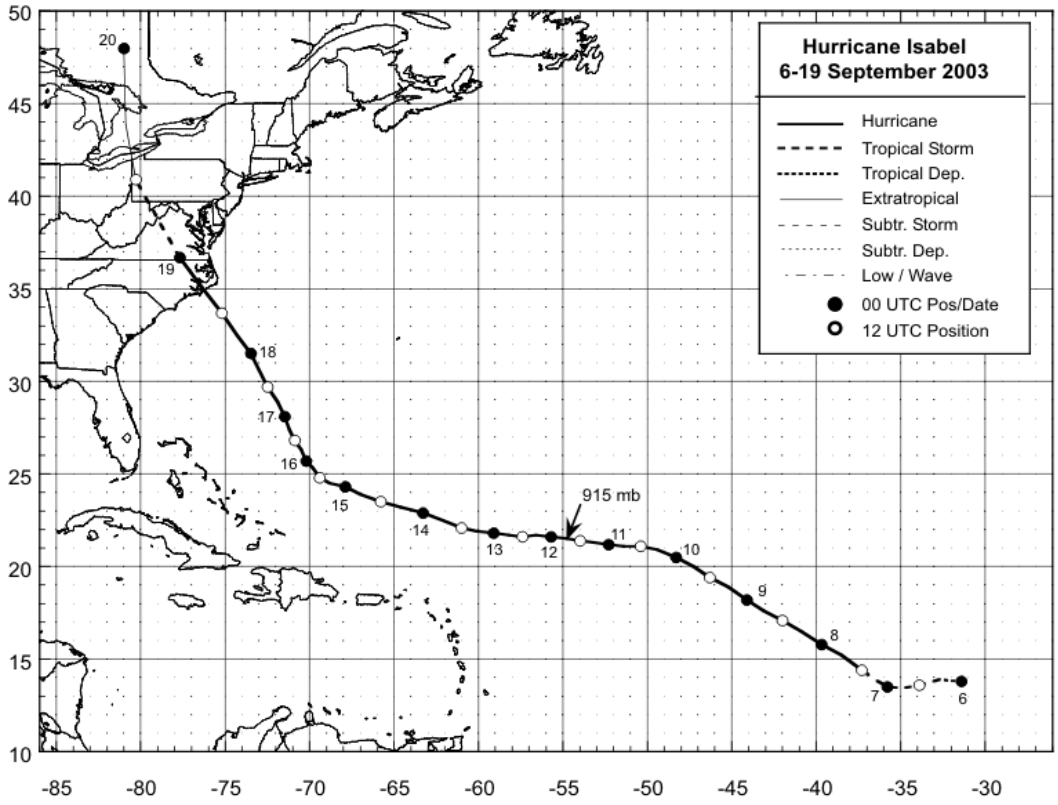

Figure 3.25. Best track positions for Hurricane Isabel, 6-19 Sept. 2003. Reprinted from National Hurricane Center homepage [Available online at http://www.nhc.noaa.gov/].

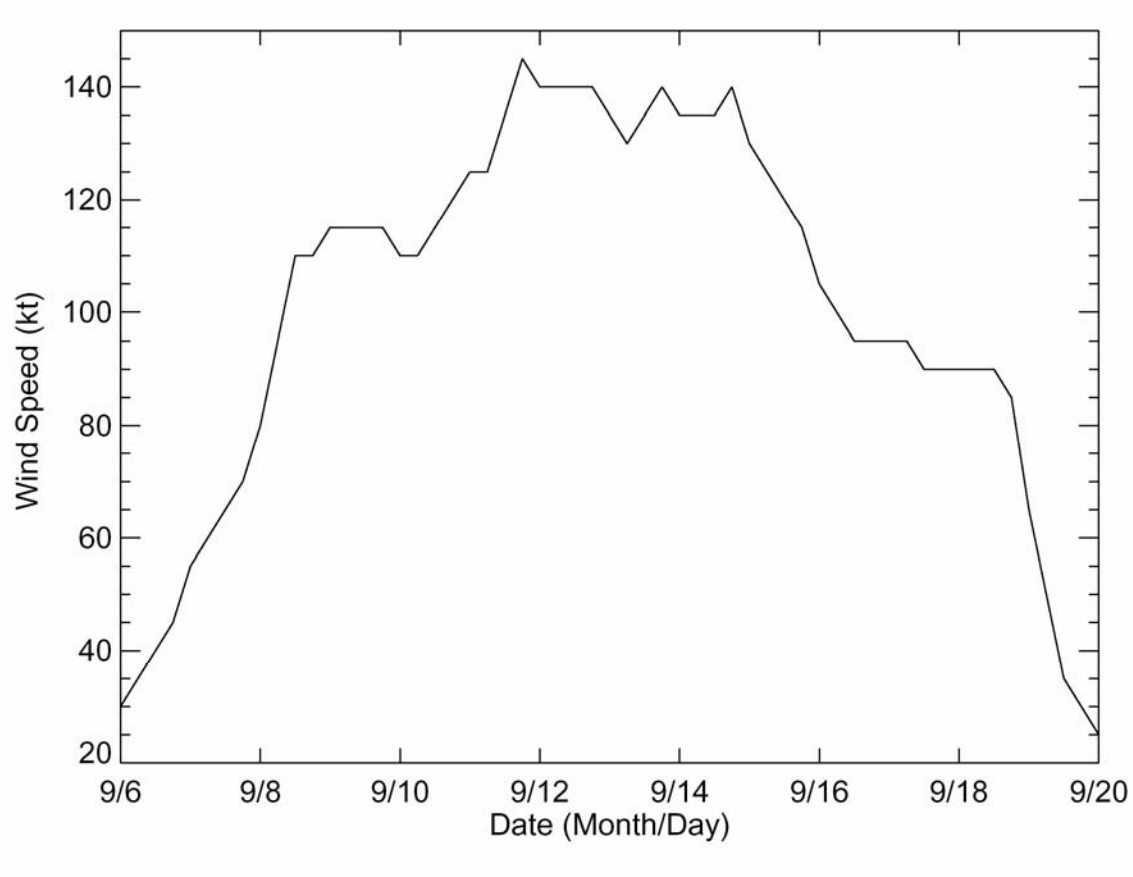

Figure 3.26. Best track maximum sustained surface wind speed curve for Hurricane Isabel, 6-20 Sept. 2003.

Fig. 3.27 shows this Isabel TRMM overpass as seen by the PR and TMI on Sept. 08, 2003. The TMI 85 and 37 GHz PCT are shown in panel (a) and (b), respectively. They show considerable ice scattering depressions in the eyewall region at 85 GHz down to 150 K and at 37 GHz down to 250 K, and in the outer rainband region at 85 GHz down to 200 K and at 37 GHz down to 260 K. The TMI 19 and 10 GHz vertical polarization brightness temperatures (d) and (e) show the rain emission warming at 19 GHz up to 275 K and at 10 GHz up to 240 K. The PR 2A25 near surface reflectivity field (c) shows a convective arc-shape eyewall with maximum intensity of 50 dBZ. An inner rainband with maximum intensity of 45 dBZ is also seen in (c), which has not much ice- scattering as shown in (a) and (b). The outer rainband with a lot of ice aloft as observed by the TMI 85 and 37 GHz only has the maximum near surface reflectivity of 35 dBZ, indicating relatively low near surface rain rate. The beamfilling problem at low frequencies of TMI can be seen clearly by comparing (a), (b), (c), (d), and (e). A clear eye feature is shown in PR near surface reflectivity field (c) and TMI 85 GHz PCT field (a). But the eye shown in 37 GHz PCT field (b) is smaller, it is much smaller in 19 GHz [not clear but can be identified as the small yellow low brightness temperature region in (d)], and in 10 GHz it almost disappears (e). The PR 2A23 rain type classification is shown in (f). It should be noted that the classification shown here is only a gross overview of rain types and only consists of stratiform (blue), convective (red), others (green), and no-rain (gray). In the original 2A23 data, there are more detailed types available (e.g., “stratiform certain,” “probably stratiform,” “maybe stratiform,” “convective certain,” “probably convective,” and “others”).

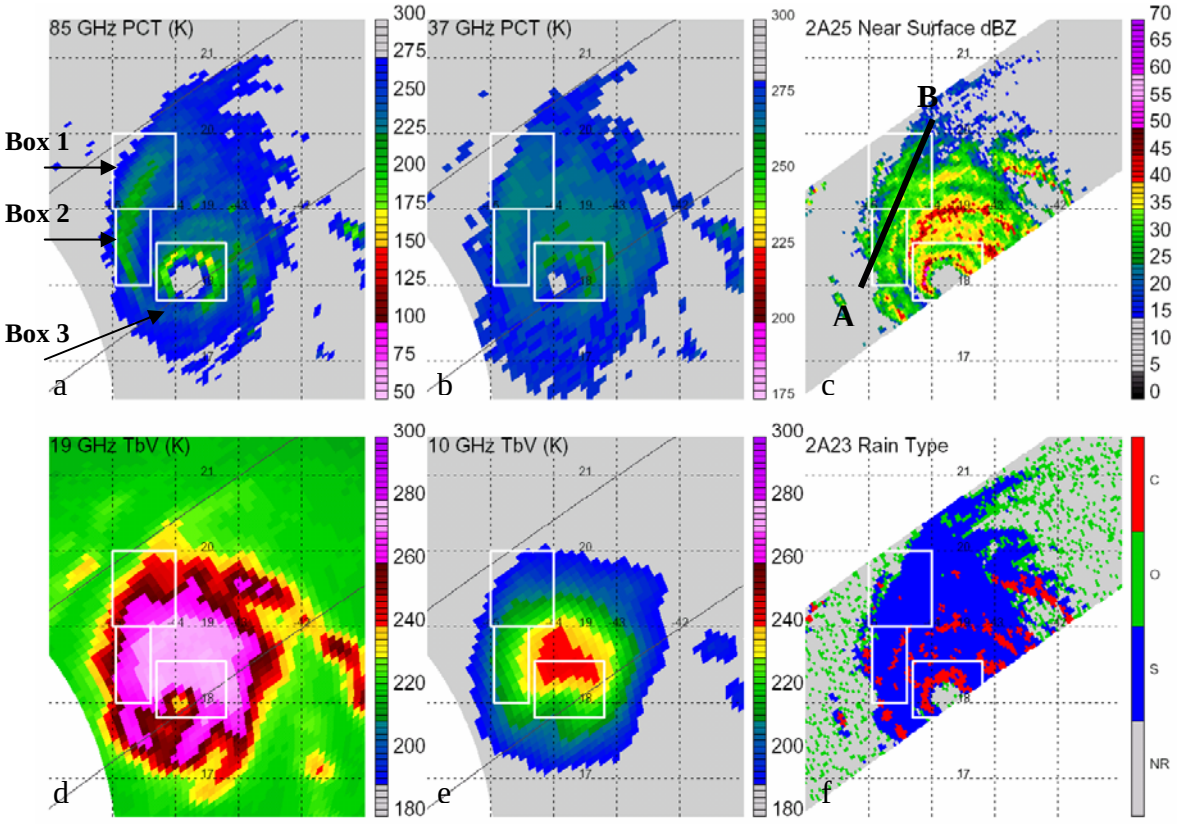

Figure 3.27. TMI and PR observations of the Hurricane Isabel over North Atlantic Ocean on Sept. 8, 2003. Each panel shows (a) TMI 85 GHz PCT (shaded, K), (b) TMI 37 GHz (shaded, K), (c) PR 2A25 near surface reflectivity (shaded, dBZ), (d) TMI 19 GHz vertical polarization T_b (shaded, K), (e) 10 GHz vertical polarization T_b (shaded, K), (f) PR 2A23 rain types: stratiform (blue), convective (red), others (green), and no-rain (gray).

Three boxes are chosen to represent the nearly uniform stratiform rain region (box 1 and 2 in Fig. 3.27) and the eyewall convective region (box 3 in Fig. 3.27, it will be analyzed in the following section). Box 1 is a $1^\circ \times 1^\circ$ box located between 19 – 20 N and 44 – 45 W. Except for 1-2 convective pixels identified by the PR 2A23 algorithm, its rain region is uniformly filled by stratiform precipitation. Box 2 is a $1^\circ \times 0.6^\circ$ box adjacent to box 1 located between 18 – 19 N and 44.4 – 45 W. This box contains more convective pixels than box 1, but the stratiform rain still dominates. It is also noted that the 2A23 convective pixels are located in the region without significant ice scattering (85 GHz PCT around 250 K), so they probably count mainly of warm rain showers. In any case, it would not be a problem to identify box 2 as a nearly uniform stratiform region. Fig. 3.28 shows an example of the cross section of the PR 2A25 attenuation corrected reflectivity across box 1 and 2 (AB line shown in Fig. 3.27c). The bright band feature demonstrates that it is mainly a stratiform precipitation region.

Fig. 3.29 shows the retrieval results of IWP in box 1 and 2. The 85 GHz PCT and PR 2A25 7 km reflectivity are presented in panel (a) and (b) respectively, which are the two main inputs for the combined radar-radiometer IWC retrieval. Inside box 1 and 2, the relatively high reflectivity values (about 30 dBZ) at 7 km correspond to the 85 GHz ice scattering signature (PCT less than 220 K). Panels (c) – (f) are the retrieved IWP by the combined algorithm, version 5 (V5, current version of TRMM standard product) of 2A12, version 6 (V6, future version of TRMM standard product, will be available in late 2004) of 2A12, and Z-M algorithm.

There is a general agreement in the spatial pattern of the combined, Z-M, and 2A12 V6 IWP fields. They are consistent with the TMI 85 GHz PCT and PR reflectivity

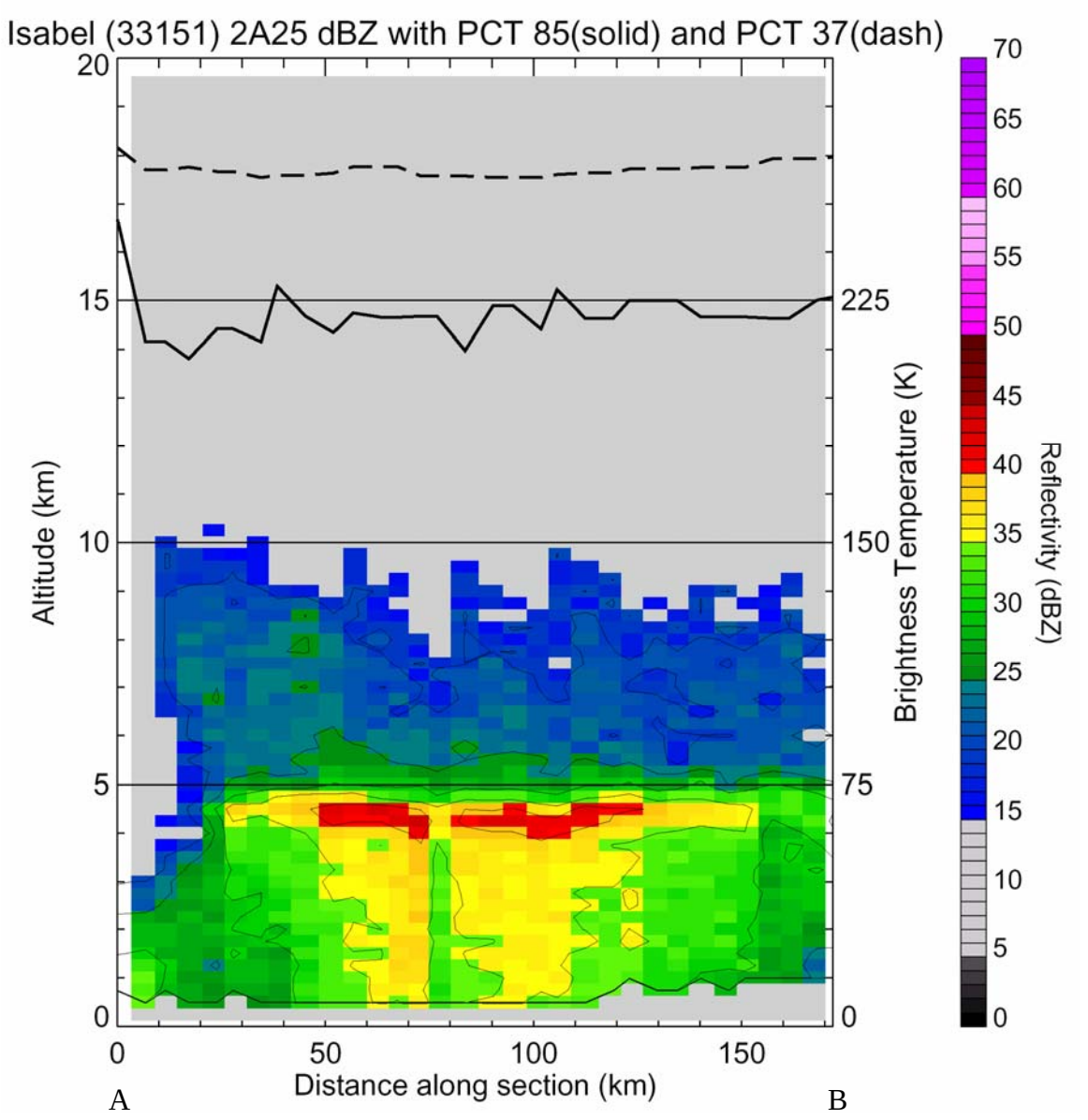

Figure 3.28. A cross section of PR 2A25 reflectivity along AB line on of Fig. 3.27 (c). The 85 GHz PCT (black solid) and 37 GHz PCT (black dash) are overplotted.

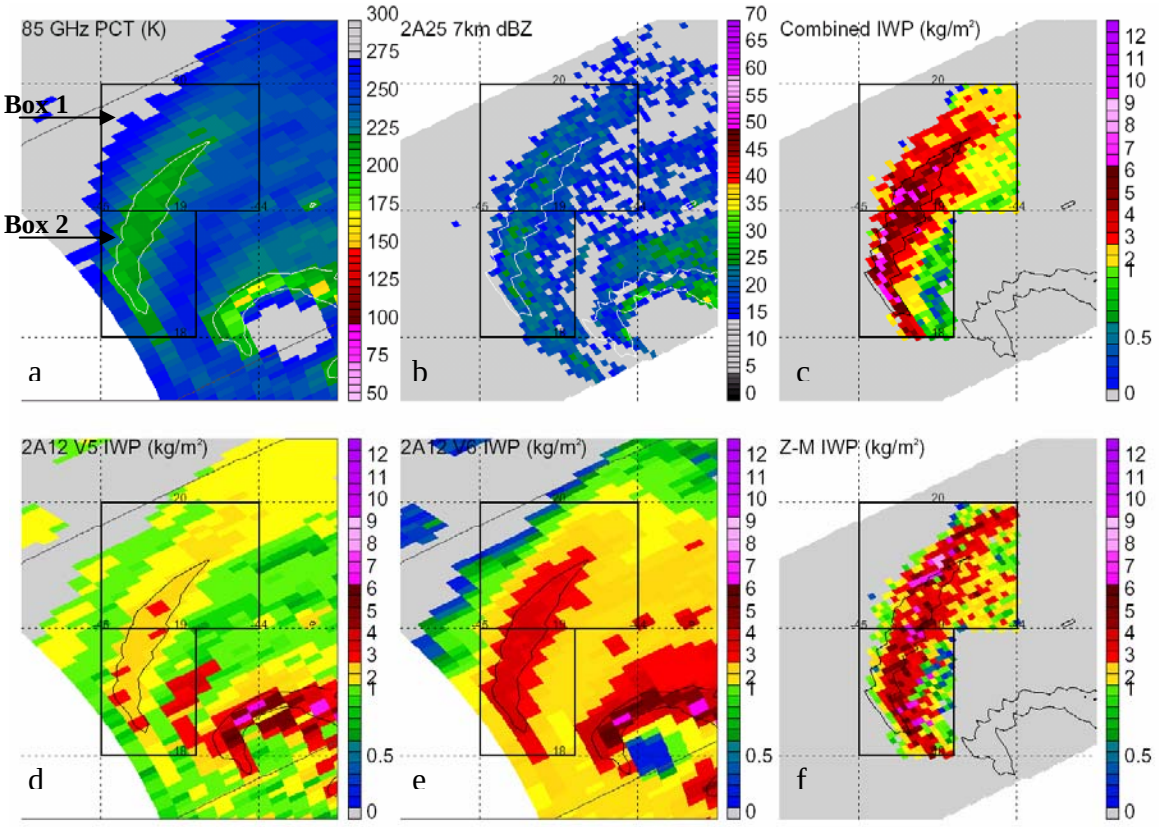

Figure 3.29. Retrieval results of ice water path (IWP) in box 1 and 2 of the Hurricane Isabel overpass on Sept. 8, 2003. Each panel shows (a) TMI 85 GHz PCT (shaded, K,), (b) PR 2A25 7 km reflectivity (shaded, dBZ), (c) IWP retrieved by the combined radar-radiometer algorithm (shaded, kg/m^2), (d) IWP retrieved by the Z-M algorithm (shaded, kg/m^2), (e) IWP retrieved by the version 5 of 2A12 algorithm (shaded, kg/m^2), (f) IWP retrieved by the version 6 of 2A12 algorithm (shaded, kg/m^2). The contour of 220 K 85 GHz PCT is overplotted in each panel.

observations. The large 2A12 V6 IWP values are related to the low 85 GHz PCT area, which is also a high reflectivity area at 7 km altitude. Similar pattern is shown in combined IWP field, but in higher resolution because of the combined use of TMI and PR. A significant result of the combined IWP field is that *all IWP values greater than 10 kg/m^2 are inside the 220 K 85 GHz PCT contour.* The Z-M IWP field has a similar pattern, but it is noisy, with several large IWP pixels outside the 85 GHz ice scattering contour. Version 5 of 2A12 IWP has a quite different pattern that is neither consistent with the TMI 85 GHz PCT nor the PR reflectivity observations. An area with large IWP values (about 7 kg/m^2) at the east edge of box 2 is artificial. The version 6 of 2A12 hasbeen improved by removing this artifact. The reason could be that the version 6 of 2A12 uses more cloud model profiles than version 5.

Fig. 3.30 shows the pixel-by-pixel comparisons of IWP between these 4 different retrievals. In general, the plots are very scattered and the correlation coefficients are low. One of the main reasons is the mismatch between the TMI and PR observations. The PR beam looks at nadir, while the TMI scans conically with an incident angle of 52.8°. For observing a precipitation feature with a height of, for example, 7 km, the TMI geographic location on the surface would be about $7 \times \sin(52.8^\circ) = 5.6$ km ahead (or behind, depending on the instruments scanning direction) of the geographic location of PR. In this study, a very simple parallax correction is done by moving TMI observations one scan number ahead or behind. Since the distance between adjacent scan lines is about 16 km, an over-correction is very possible. So the pixel-by-pixel comparison might not be fair, but it can at least tell the range of the retrieved parameters and the mean differences

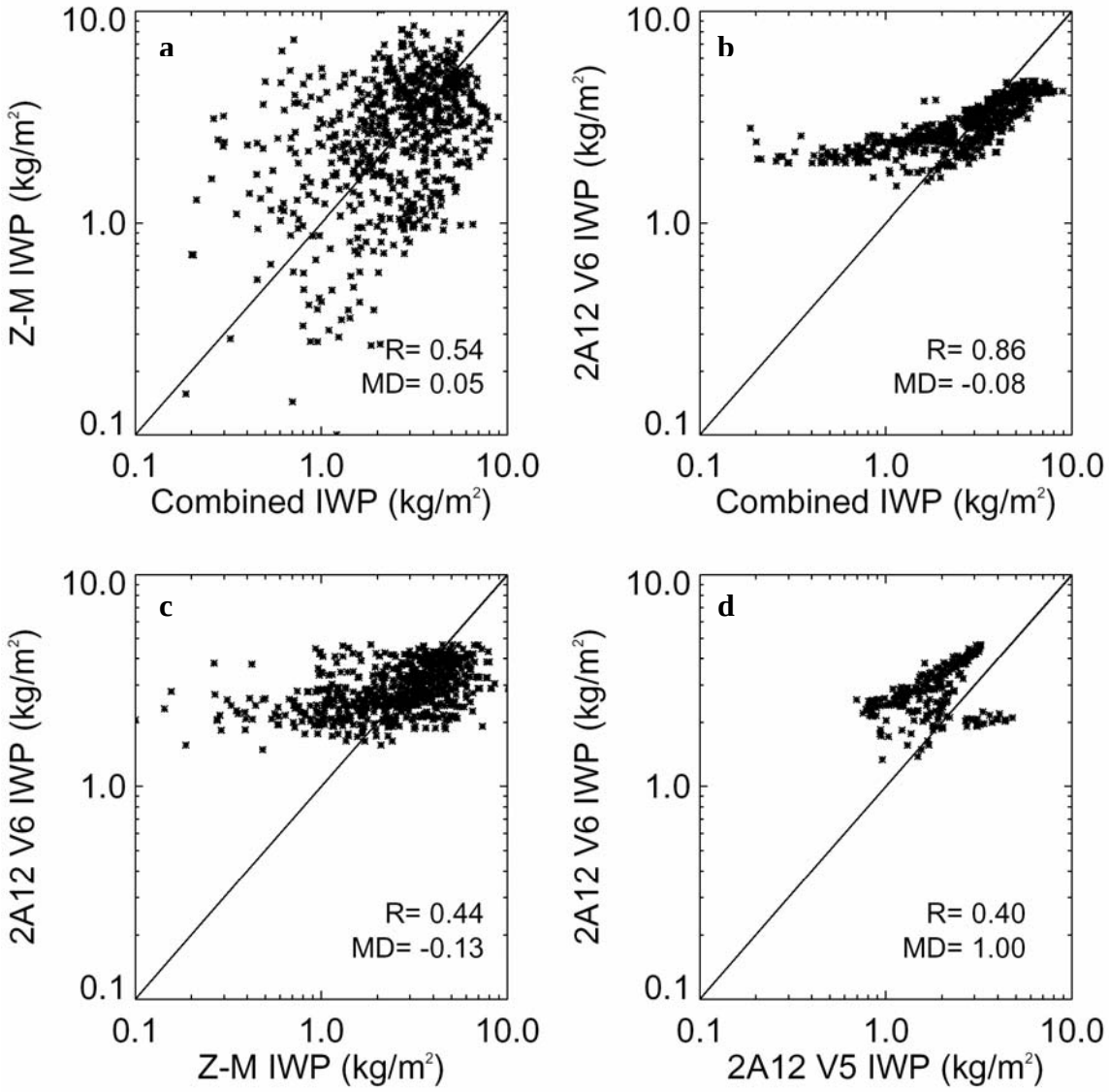

Figure 3.30. The scatter plot of (a) Z-M ice water path (IWP) versus radar-radiometer combined algorithm retrieved IWP; (b) Version 6 of 2A12 IWP versus radar-radiometer combined algorithm retrieved IWP; (c) Version 6 of 2A12 IWP versus Z-M IWP; (d) Version 6 of 2A12 IWP versus Version 5 of 2A12 IWP in box 1 and 2 of the Hurricane Isabel overpass on Sept. 8, 2003. The correlation coefficient (R) and mean difference (MD) are indicated.

between two retrievals. Therefore, the more significant comparison is the mean values in each box among different algorithms as shown in Table 3.9.

For Z-M IWP versus combined IWP in Fig. 3.30a, the correlation is low, but the mean difference is very small (also can be seen from table 3.9), indicating the agreement on average between combined and radar-only algorithm. The agreement between combined and 2A12 V6 IWP (b) is better, with a lower absolute mean difference and higher correlation coefficient. But it is interesting to note that the 2A12 V6 [and V5 in Fig. 3.30d] has no IWP values less than 1 kg/m^2 and greater than 5 kg/m^2 comparing the IWP range of 0.1 to 10 kg/m^2 in the combined and Z-M estimates, showing an insensitivity of 2A12 relative to the combined and Z-M estimates. As discussed above, the beamfilling problem is not substantial for the IWC retrieval in stratiform regions for both radar-only, radiometer-only, and the combined algorithms. That is why the mean IWP differences among those retrievals are very small. But because the footprint difference between TMI 85 GHz and PR is about 2-3 km, this very likely causes the 2A12 insensitivity problem. The combined algorithm doesn't show this problem because of the use of PR observations. For the 2A12 V6 versus Z-M IWP (c), the correlation is very low and the mean difference is higher, showing the discrepancy between radiometer-only and radar-only algorithms. For the 2A12 V6 versus V5 (d), the improvement of 2A12 from V5 to V6 is obvious. The 1 kg/m^2 increase of mean IWP from V5 to V6 makes 2A12 estimate very close to that of the combined and Z-M algorithms.

Table 3.9. Mean IWP (in kg/m^2) estimated by the combined, 2A12 version 5 (V5), 2A12 version 6 (V6), and Z-M algorithms for box 1 and 2 of Fig. 3.27.

Mean IWP	Combined	2A12 V5	2A12 V6	Z-M
Box 1	3.01	1.76	2.82	3.01
Box 2	3.04	2.22	3.13	3.17
Box 1 & 2	3.02	1.95	2.95	3.07

Fig. 3.31 shows the LWP retrievals in box 1 and 2. The 19 GHz vertical polarization brightness temperature and PR 2A25 near surface reflectivity are presented in panel (a) and (b). The 220 k contour of 85 GHz PCT is over-plotted in each panel of Fig. 3.31 for comparisons. From TMI and PR observations shown in (a) and (b), the strong upper level ice scattering signature is not directly related to the strong lower level rain emission, in other words, the storm is tilted. The most intensive rain band [as shown by arrow A in panel (b)] in box 1 and 2 is located to the south-east of the strong ice scattering contour. Because of the large footprint, this intense narrow rain band shown in (b) appears to be a large area with a high brightness temperature of about 270 K in the 19 GHz vertical polarized Tb field. The narrow rain band feature can be found in both of the combined LWP (c) and Z-M LWP (f) fields, although it is a little bit wider in the combined LWP field. This fact, as well as the similar patterns in the whole box 1 and 2 among (a), (b), (c), and (f), indicates that these two retrievals are consistent with the PR and TMI observations. The spatial patterns of the 2A12 V5 (d) and V6 (e) LWPs are quite different from the above two retrievals as well as from the observations. They appear to be consistent with the 85 GHz ice scattering instead of the low frequency rain emission and PR low level reflectivity observations. This strange performance demonstrates that in this case the 2A12 overemphasizes the high frequency information, but neglects the information from low frequencies, which sometimes are very important although they are in very low resolutions. In this circumstance (the ice aloft is tilted relative to the rain below), the scattering information is misleading for low level liquid water estimates. The overestimate of 2A12 V5 LWP inside the ice-scattering contour is

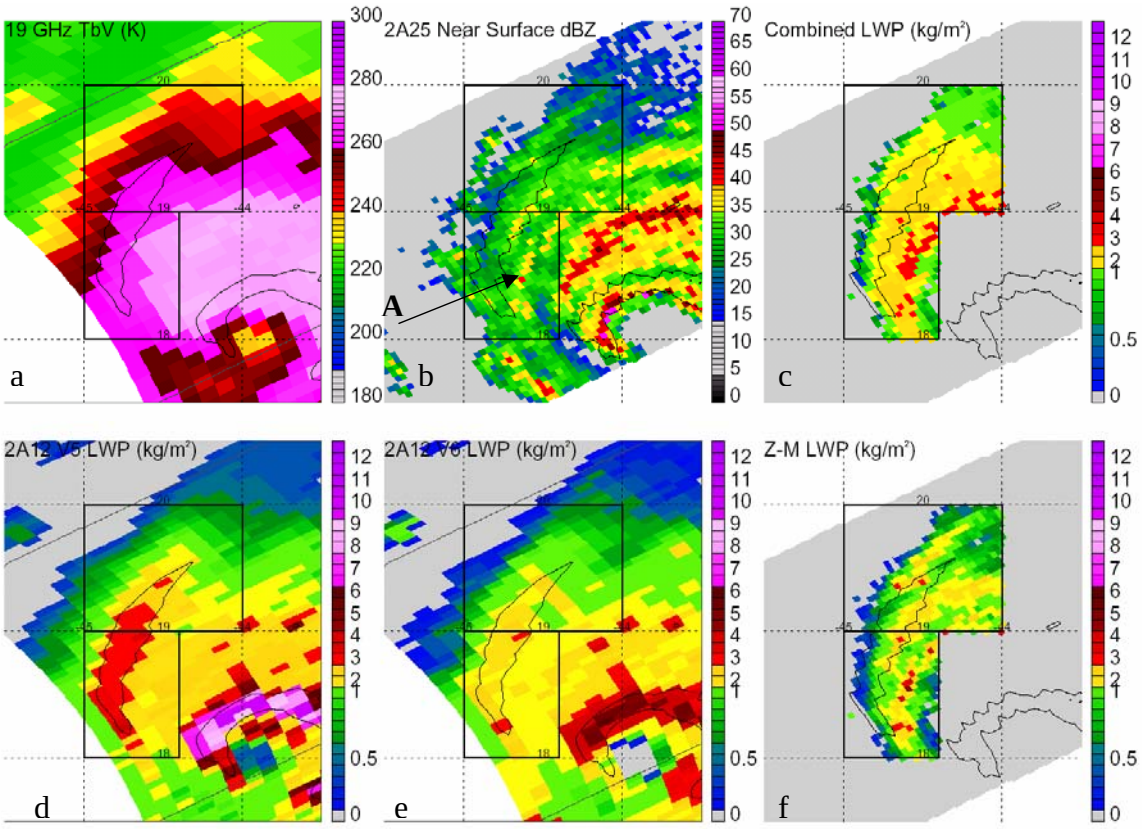

Figure 3.31. Retrieval results of liquid water path (LWP) in box 1 and 2 of the Hurricane Isabel overpass on Sept. 8, 2003. Each panel shows (a) TMI 19 GHz vertical polarization T_b (shaded, K), (b) PR 2A25 near surface reflectivity (shaded, dBZ), (c) LWP retrieved by the combined radar-radiometer algorithm (shaded, kg/m^2), (d) LWP retrieved by the Z-M algorithm (shaded, kg/m^2), (e) LWP retrieved by the version 5 of 2A12 algorithm (shaded, kg/m^2), (f) IWP retrieved by the version 6 of 2A12 algorithm (shaded, kg/m^2). The contour of 220 K 85 GHz PCT is overplotted in each panel.

about a factor of 2 relative to the combined and Z-M estimates. A significant change of the 2A12 V6 LWP magnitude is found, especially inside the ice-scattering contour, which makes it very close to the radar-radiometer and radar-only retrievals. This change results from the inclusion of the melting layer emission in 2A12 V6 (C. Kummerow, personal communication). But the pattern of 2A12 V6 LWP field is still similar to that of 2A12 V5, showing that the large footprint of the low frequency channels remains problematic.

Similarly to Fig. 3.30, Fig. 3.32 presents the scatter plots between different LWP retrievals in box 1 and 2. Again the plots are very scattered because of the matching problem between the PR and TMI due to the different incident angle of the two instruments. The best correlation is found between the Z-M and combined LWP (a), with a correlation coefficient of 0.79. Although the mean difference between the 2A12 V6 and combined (b) is lower than that between the Z-M and combined, the insensitivity problem of 2A12 LWP makes the correlation coefficients in (b) and (c) quite low. From the comparison between 2A12 V5 and V6 (d), the 2A12 V6 estimate is lower than V5 by 0.47 kg/m^2 on average, but the correlation coefficient is high (0.91), showing there is no major change on the spatial pattern and basic physics.

Table 3.10 shows the mean LWP retrievals in box 1 and 2. The 2A12 V5 mean LWP is about 100% higher than the Z-M mean LWP, while the combined and 2A12 V6 retrievals are very close to each other and they are about 30% higher that the Z-M LWP. The similarity of the mean values between the combined and 2A12 V6 LWP is considered to be by chance given their different spatial patterns. As pointed out by Nesbitt et al. (2004), the overestimation of 2A12 V5 LWP in stratiform precipitation is mainly caused by the melting layer emission, which is not accounted for in the 2A12 V5

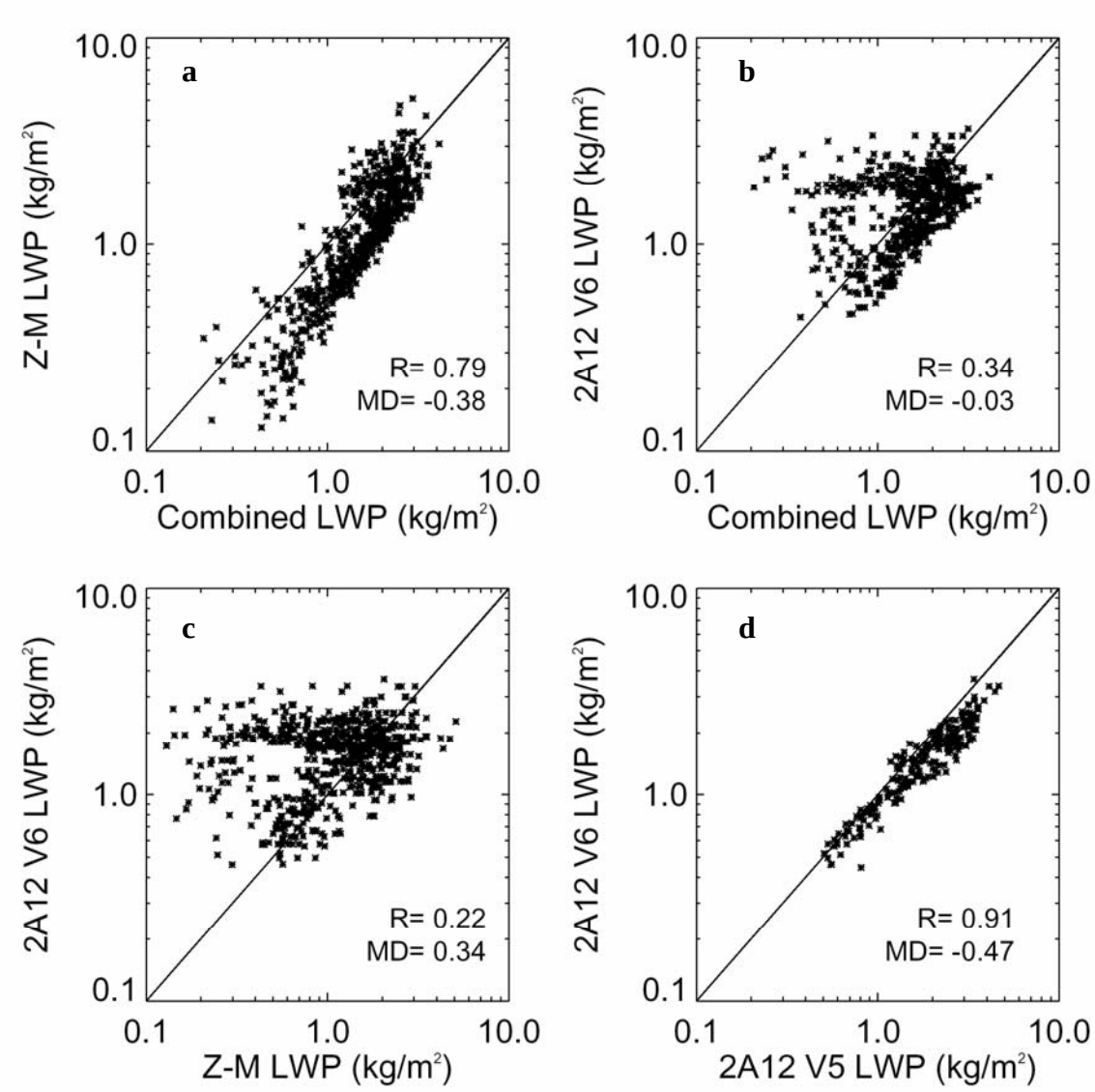

Figure 3.32. The scatter plot of (a) Z-M liquid water path (LWP) versus radar-radiometer combined algorithm retrieved LWP; (b) Version 6 of 2A12 LWP versus radar-radiometer combined algorithm retrieved LWP; (c) Version 6 of 2A12 LWP versus Z-M LWP; (d) Version 6 of 2A12 LWP versus Version 5 of 2A12 LWP in box 1 and 2 of the Hurricane Isabel overpass on Sept. 8, 2003. The correlation coefficient (R) and mean difference (MD) are indicated.

Table 3.10. Mean LWP (in kg/m^2) estimated by the combined, 2A12 version 5 (V5), 2A12 version 6 (V6), and Z-M algorithms for box 1 and 2 of Fig. 3.27.

Mean LWP	Combined	2A12 V5	2A12 V6	Z-M
Box 1	1.61	1.69	1.34	1.29
Box 2	1.72	2.65	2.01	1.26
Box 1 & 2	1.66	2.09	1.62	1.28

LWP (Olson et al. 2001a,b; Kummerow et al. 2001). In the hydrometeor profiles with less ice optical depth above the emission layer, the increase in emission primarily by water-coated aggregates above the freezing level has been shown to increase passive microwave rain rate retrievals by up to 100% (Bauer et al. 1999). However, the 2A12 V6 includes the melting-layer emission, while the combined algorithm does not. Since we also find that the 2A12 V5 and V6 overemphasize the scattering information in strong ice-scattering features when estimating the liquid water content, the similar estimates between 2A12 V6 and combined algorithm probably result from different physical processes. On the other hand, the sensitivity of the radar-only rainfall estimate to the PR attenuation correction and the raindrop size distribution assumption also causes uncertainty in the Z-M estimate. Masunaga et al. (2002) found that TMI near surface precipitation water content values at low latitudes are higher than the PR's and they linked this low bias to the PR's attenuation correction. Since there is no validation data available, we can not judge which estimate is better. Considering the uncertainties among these 4 algorithms and the instrument footprint mismatching, we think the agreement among the combined, Z-M, and 2A12 V6 algorithm is relatively good.

The vertical profiles of mean liquid and ice water contents estimated by the combined, Z-M, and 2A12 V5 and V6 algorithms are presented in Fig. 3.33. In the ice region, although the mean IWPs from the combined and Z-M algorithm are very close to each other, the Z-M IWC above 7 km is lower than the corresponding combined IWC. This is consistent with the CAMEX-4 comparison result shown in Fig. 3.12 and Fig. 3.13. The Z-IWC relation provided by Black (1990) was derived from the aircraft in-situ measurements at 6-7 km and might be an underestimate for IWC above 7 km. On the

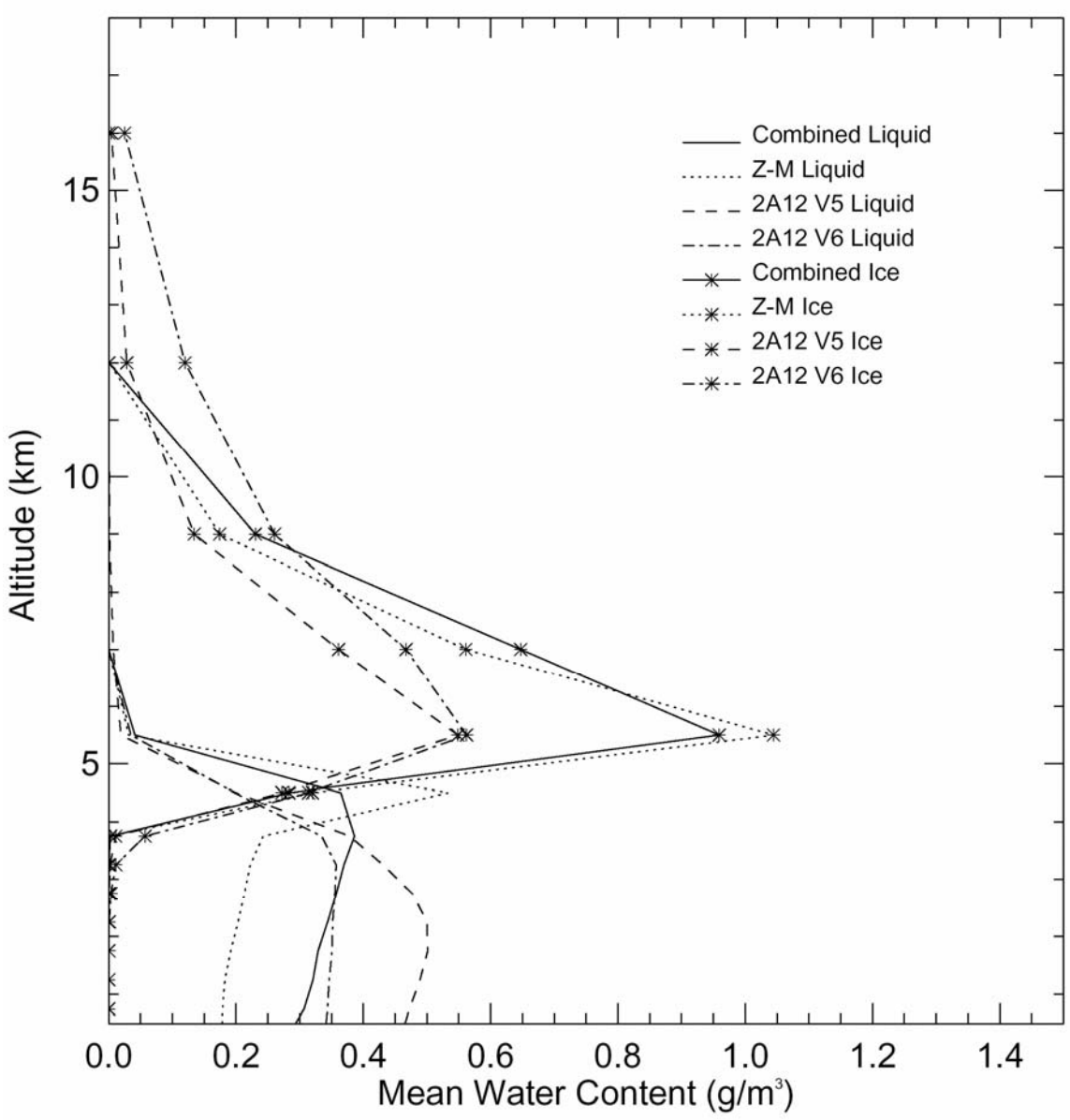

Figure 3.33. Vertical profiles of mean hydrometeor (liquid and ice precipitation water) content estimated by the combined, Z-M, 2A12 version 5 (V5), and 2A12 version 6 (V6) algorithms for box 1 and 2 in Fig. 3.27.

other hand, the shape of ice water content profiles from the combined and radar-only algorithm is in very good agreement, but the shape of 2A12 V5 and V6 ice water profiles is quite different. Although the height of the maximum IWC is the same (5-7 km) for all retrievals, the magnitude of 2A12 IWC retrievals is much smaller than the other two. By comparing with the PR reflectivity profile and cloud top observations, the non-zero values of 2A12 V5 and V6 above 12 km are considered to be artificial, which may be due to the inappropriate selection of the hydrometeor profiles by the 2A12's Bayesian scheme, or differences between the selected cloud model profiles and nature. Such 2A12 IWC profiles might produce 85 and 37 GHz brightness temperatures resembling the TMI observed, but the shape is not consistent with radar observations. On the other hand, the combined algorithm can keep the shape of radar observed hydrometeor profiles as well as obtain total water content estimates consistent with TMI observations. Similarly, in the rain region, the vertical shapes of the Z-M LWC and combined LWC are in agreement except for the melting layer, although the combined LWC is about 50% higher than the Z-M LWC below the melting layer. The mean LWC profile of the 2A12 V6 retrieval below the melting layer is very close to that of the combined retrieval, while the 2A12 V5 profile has a quite different vertical shape and a significant overestimate. These are all similar as has been found in the mean LWP comparisons in Table 3.10.

3.7.4 Case Study for Eyewall Regions in Hurricane Isabel (2003)

The box 3 shown in Fig. 3.27 is the box that is chosen to study the Isabel eyewall region including intense convective precipitation. It is a $0.8^{\circ} \times 1.1^{\circ}$ box located between 17.8 and 18.6 N, 43.2 and 44.3 W. A strong eyewall can be seen from the 85 GHz PCT

(Fig. 3.27a), 37 GHz PCT (Fig. 3.27b), and PR near surface reflectivity (Fig. 3.27c) fields. The PR 2A23 rain type classification shows the eyewall to be convective. As mentioned previously, the eye and eyewall features could hardly be seen in low frequency observations (Fig. 3.27 d,e) due to the large footprints. In addition to the beamfilling problem, the tilting eyewall geometry will cause some difficulties in the retrieval. Fig. 3.34 shows the schematic radius-height cross section of a typical hurricane eyewal structure. The core of maximum radar reflectivity has an outward slope. Since the PR looks at nadir, but the TMI has a slant view, the slope of the eyewall structure will cause some uncertainties to match the PR and TMI observations.

Let us first consider the IWP retrievals shown in Fig. 3.35. The combined IWP field (c) has a similar pattern to the 2A12 V5 (d) and V6 (e) and Z-M (f) retrievals and 85 GHz PCT (a) and PR 7 km reflectivity (b), except that the Z-M IWP field appears to be noisy. For the eye region, the combined and radar-only algorithm can easily identify the no-echo region from the PR observations, but there are non-zero values of IWP from the 2A12 V5 and V6, showing that the radiometer-only algorithm has trouble identifying this kind of feature.

The pixel-by-pixel comparisons (Fig. 3.36) are very scattered. The reason has been explained in previous sections. Comparing with the radar-only algorithm (Fig. 3.36a), the combined algorithm doesn’t show the beamfilling-caused insensitivity problem that is shown for 2A12 V6 comparing with Z-M (Fig. 3.36c). This fact indicates that even in the eyewall convective region with a strong rain inhomogeneity, the combined algorithm performs like a radar-only algorithm and avoids the beamfilling problem caused by a radiometer-only algorithm.

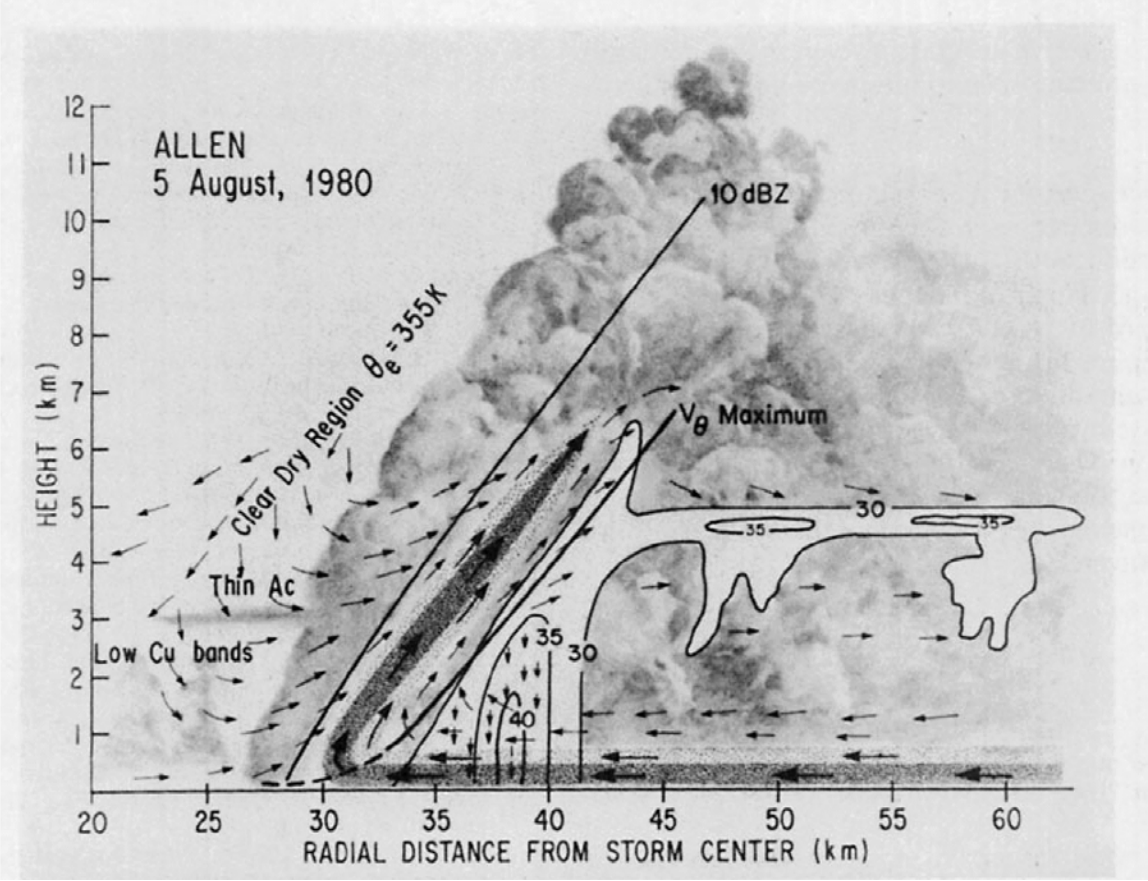

Figure 3.34. Schematic cross section depicting the locations of the clouds and precipitation, the radius of maximum wind (RMW), and radar-vertical airflow through the eyewall of Hurricane Allen on 5 Aug. 1980. The downward motion in the eye is based on estimates of radial divergence, while the downdrafts within the high rainfall rate region are inferred from vertical velocity time series from the individual passes. Radar reflectivity (dBZ) contours are based on a composite using 15 passes, although there is considerable pass-to-pass variability. The slope of the cloudy region on the inside edge of the eyewall is based on radar minimum detectable signal analysis, aircraft altimeter readings, handheld photography and observer notes. Darker shaded regions denote the location of the largest radial and vertical velocity (reprinted with permission from Jorgensen 1984b).

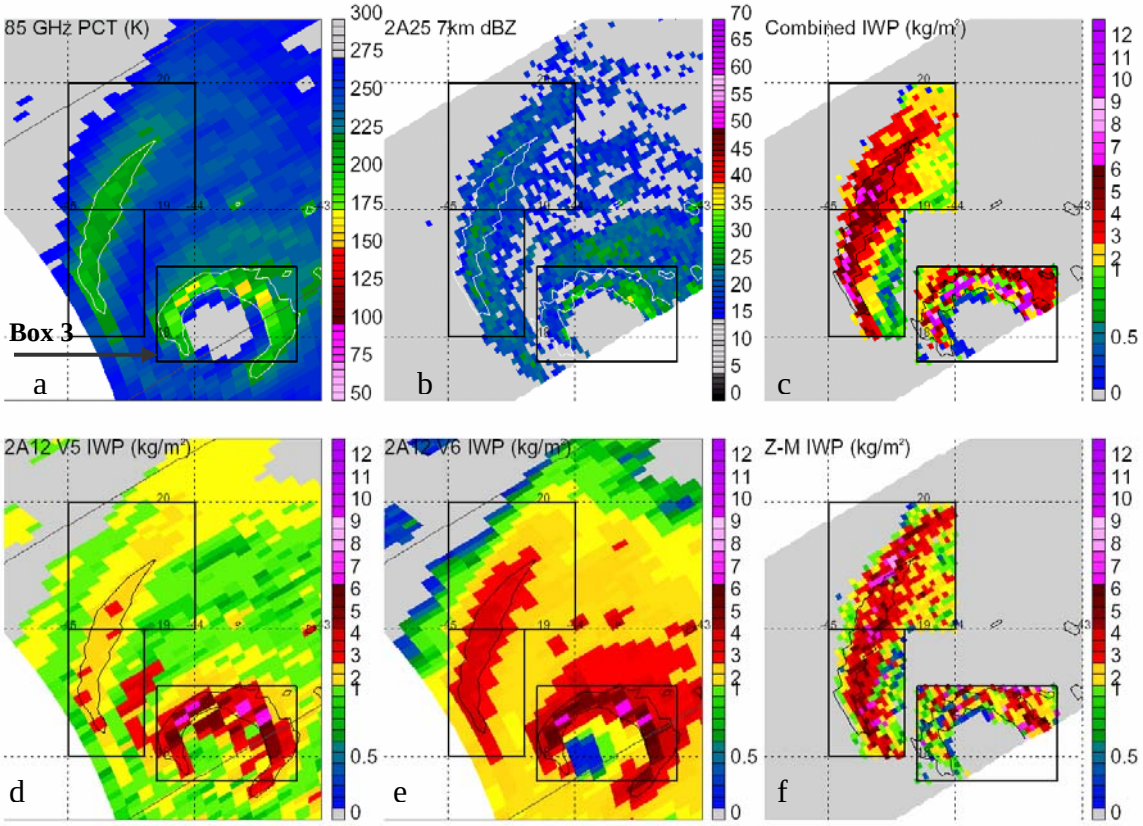

Figure 3.35. Retrieval results of ice water path (IWP) in box 3 of the Hurricane Isabel overpass on Sept. 8, 2003. Each panel shows (a) TMI 85 GHz PCT (shaded, K,), (b) PR 2A25 7 km reflectivity (shaded, dBZ), (c) IWP retrieved by the combined radar-radiometer algorithm (shaded, kg/m^2), (d) IWP retrieved by the Z-M algorithm (shaded, kg/m^2), (e) IWP retrieved by the version 5 of 2A12 algorithm (shaded, kg/m^2), (f) IWP retrieved by the version 6 of 2A12 algorithm (shaded, kg/m^2). The contour of 220 K 85 GHz PCT is overplotted in each panel.

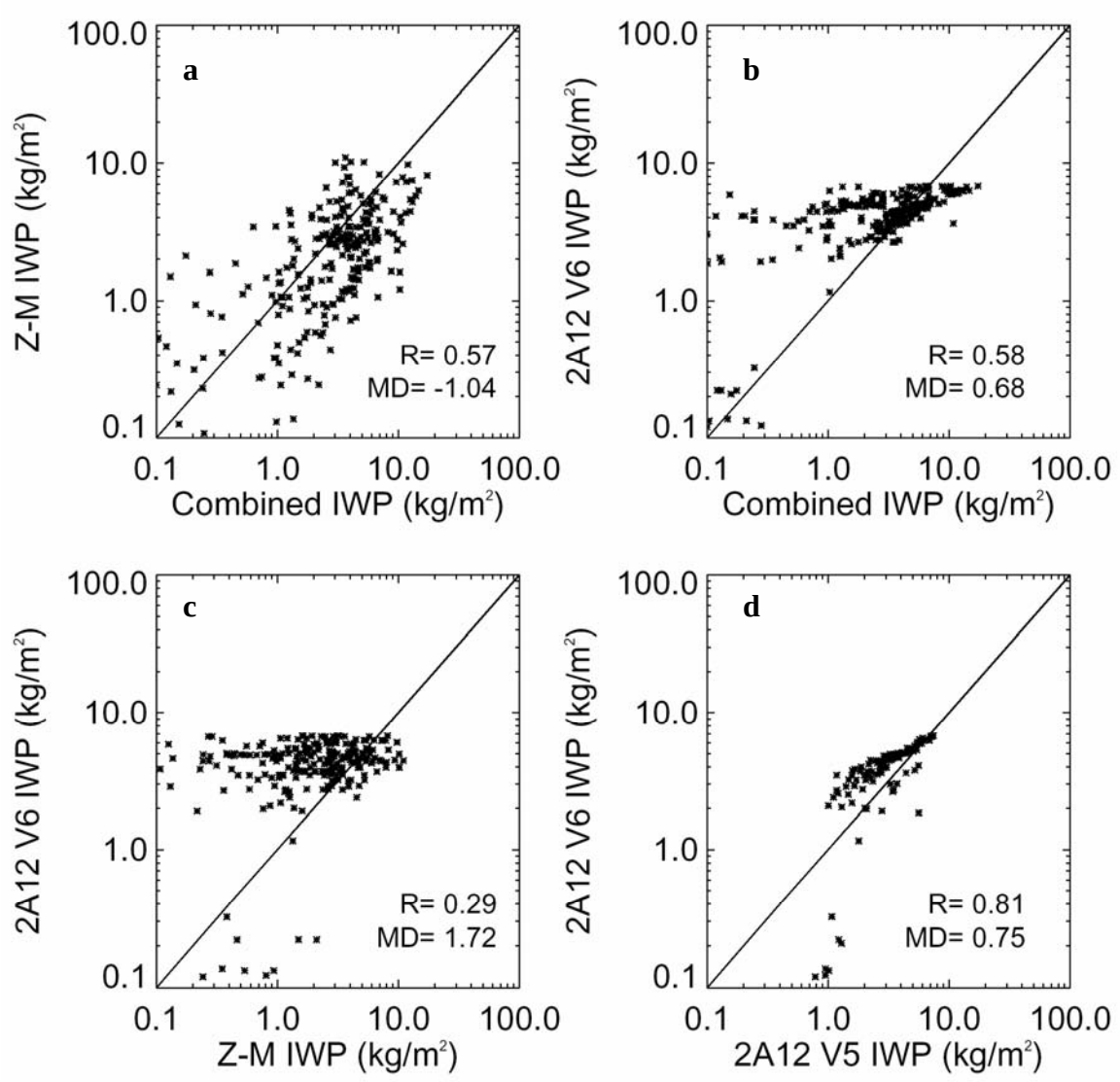

Figure 3.36. The scatter plot of (a) Z-M ice water path (IWP) versus radar-radiometer combined algorithm retrieved IWP; (b) Version 6 of 2A12 IWP versus radar-radiometer combined algorithm retrieved IWP; (c) Version 6 of 2A12 IWP versus Z-M IWP; (d) Version 6 of 2A12 IWP versus Version 5 of 2A12 IWP in box 3 of the Hurricane Isabel overpass on Sept. 8, 2003. The correlation coefficient (R) and mean difference (MD) are indicated.

Table 3.11. Mean IWP and LWP (in kg/m^2) estimated by the combined, 2A12 version 5 (V5), 2A12 version 6 (V6), and Z-M algorithms for box 3 of Fig. 3.27a.

	Combined	2A12 V5	2A12 V6	Z-M
Mean IWP	3.59	3.52	4.28	2.55
Mean LWP	2.83	5.83	3.79	2.63

The mean IWPs (Table 3.11) are quite different among these four algorithms. A 40% overestimate is found for the combined and 2A12 V5 IWP relative to the Z-M IWP. The 2A12 V6 mean IWP is even higher, about 68% higher than the Z-M retrieval. It is not surprising to have a 40-70% variation. This large uncertainty is mainly caused by the unique dynamics in the eyewall region. Strong embedded updrafts in the broader eyewall updraft can lift liquid water above the freezing level and make the microphysics in the ice region very complicated. In addition to snow and graupel species, there can be a certain amount of supercooled water (Simpson 1963; Black et al. 1994; Herman and Heymsfield 2003; Black et al. 2003; Heymsfield et al. 2001). The Z-M relationship in the convective region definitely counts a lot of supercooled water and graupel so that the IWC estimate is much lower than that in stratiform region for the same radar reflectivity. This might be true for the lower level such as 6-7 km, which is the level that the NOAA P3 aircraft flew for obtaining the microphysical measurements that were used to derive the Z-IWC relationship in Black (1990). But for higher levels, it is questionable because of the strength of updrafts in tropical cyclones is generally much weaker that those in continental convection (Zipser and LeMone 1980; Jorgensen and LeMone 1989; Jorgensen et al. 1985; Lucas et al. 1994; Zipser and Lutz, 1994; Cecil et al. 2002; Toracinta et al. 2002). On the other hand, the combined algorithm assumes no supercooled water and a simple snow/graupel fraction above the top of the melting layer (about 6 km). The no-supercooled water assumption may be true for most cases, but for unusually intense eyewalls including strong “hot towers” it is questionable. The simple snow/graupel fraction assumption may also cause some uncertainties. The 2A12

algorithm depends on the cloud model runs and it is also very sensitive to the microphysical parameterization.

The LWP retrievals in box 3 are presented in Fig. 3.37. From the PR near surface reflectivity observations (b), the strong eyewall feature is only a very narrow arc-shaped band. The reflectivity is decreased from 50 dBZ to 30-35 dBZ from the strongest part of the eyewall to the transition zone. But the 19 GHz vertically polarized brightness temperature field (a) shows almost universally high values of 270 K. The overemphasizing of the high frequency information instead of the low frequency information makes the 2A12 V5 and V6 LWP fields a very different pattern comparing with the combined and Z-M LWP fields. The latter two are in good agreement and they are consistent with PR observations. But the 2A12 LWP fields are in similar pattern with the 85 GHz observation, with large LWP values inside the 200 K contour of the 85 GHz PCT. Because of the beamfilling problem, no clear eye can be seen in the 2A12 V5 LWP field, while the 2A12 V6 makes an improvement by showing about 1/3 clear eye in its LWP retrieval.

Fig. 3.38 shows the pixel-by-pixel comparisons for LWP retrievals from different algorithms in box 3. From the Z-M LWP versus combined LWP (a), the use of low frequency observations does produce an insensitivity problem on the combined retrieval relative to the radar-only retrieval. The large Z-M LWP values above 7 kg/m^2 are underestimated and the small Z-M LWP values below 0.2 kg/m^2 are overestimated by the combined algorithm. The insensitivity problem of the 2A12 V6 is more severe from the 2A12 V6 versus combined (b) and the 2A12 V6 versus Z-M (c) comparisons. The 2A12 V6 LWP is confined between 0.6 to 6 kg/m^2, all values beyond this range are either

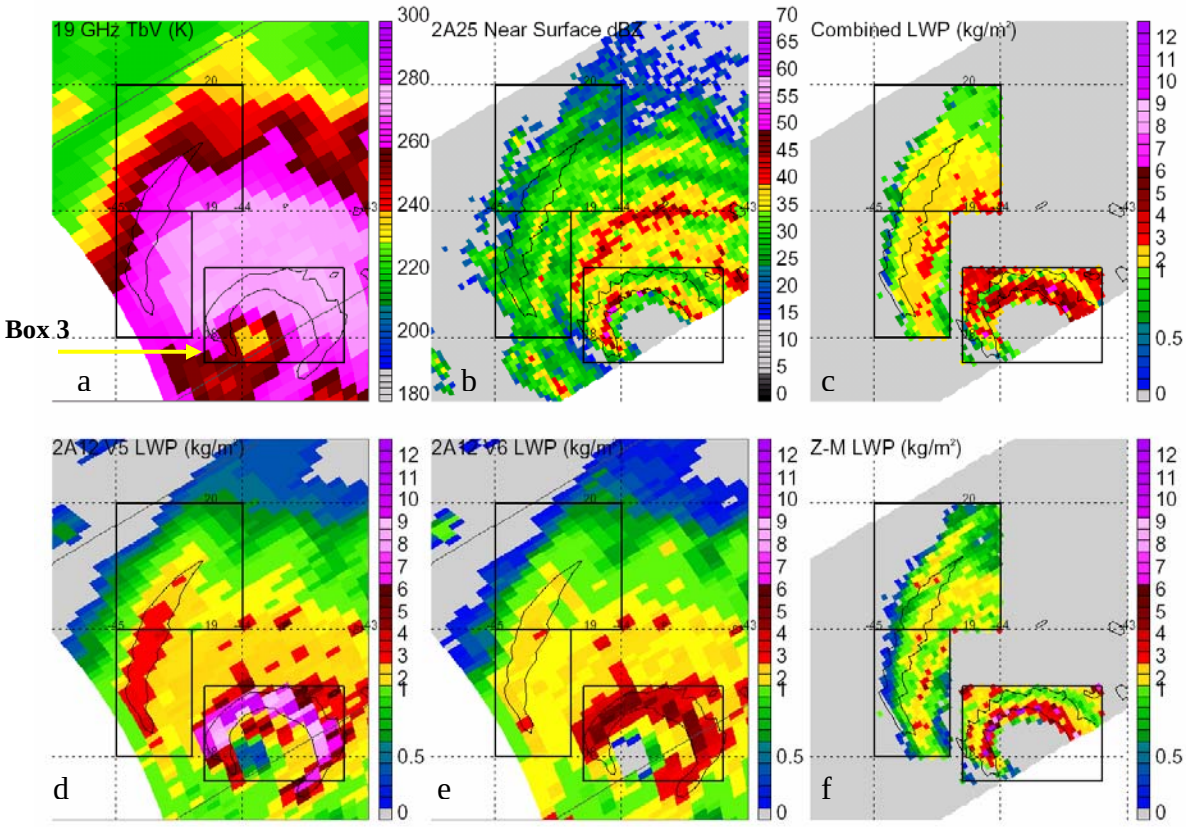

Figure 3.37. Retrieval results of liquid water path (LWP) in box 3 of the Hurricane Isabel overpass on Sept. 8, 2003. Each panel shows (a) TMI 19 GHz vertical polarization T_b (shaded, K), (b) PR 2A25 near surface reflectivity (shaded, dBZ), (c) LWP retrieved by the combined radar-radiometer algorithm (shaded, kg/m^2), (d) LWP retrieved by the Z-M algorithm (shaded, kg/m^2), (e) LWP retrieved by the version 5 of 2A12 algorithm (shaded, kg/m^2), (f) IWP retrieved by the version 6 of 2A12 algorithm (shaded, kg/m^2). The contour of 220 K 85 GHz PCT is overplotted in each panel.

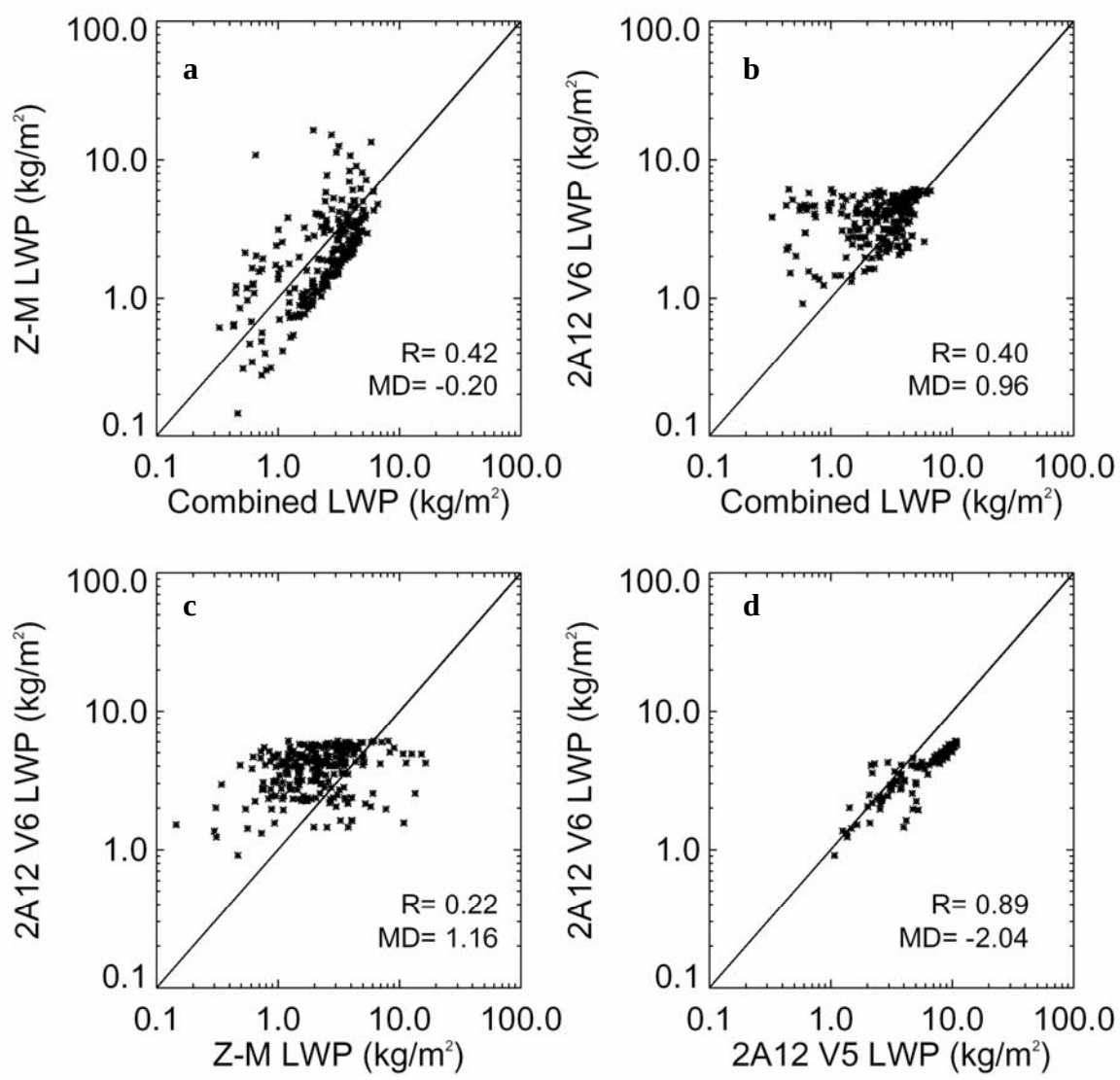

Figure 3.38. The scatter plot of (a) Z-M liquid water path (LWP) versus radar-radiometer combined algorithm retrieved LWP; (b) Version 6 of 2A12 LWP versus radar-radiometer combined algorithm retrieved LWP; (c) Version 6 of 2A12 LWP versus Z-M LWP; (d) Version 6 of 2A12 LWP versus Version 5 of 2A12 LWP in box 3 of the Hurricane Isabel overpass on Sept. 8, 2003. The correlation coefficient (R) and mean difference (MD) are indicated.

overestimated or underestimated. As noted in previous sections, the LWC retrieval in the strong convective region would be affected by the beamfilling problem to the largest extent. Comparing with three previous cases (IWC and LWC in the stratiform region, IWC in the convective region), this is the only case that the combined retrieval appears to be biased by the beamfilling problem relative to the radar-only algorithm. On the other hand, the 2A12 is biased for all the four cases.

The mean LWP retrievals from the combined and Z-M algorithm are in agreement with only a slight overestimate of the combined relative to Z-M estimate (Table 3.11). But a 44% (120%) overestimate is found for the 2A12 V6 (V5) retrievals relative to the Z-M LWP. The overall 25% overestimate of 2A12 V5 relative to the PR 2A25 rainfall is found by Nesbitt et al. (2004). They found that the overestimate is preferentially evident in the large Mesoscale Convective System (MCS) features that contain a higher fraction of stratiform rain than in smaller, more isolated features. They linked this bias to the non-inclusion of the melting-layer emission in 2A12 V5. They also found that the convective intensity is positively correlated with the TMI overestimates relative to PR. Similarly, we find that the 2A12 V6 LWP overestimate in the intense convective region (44%) is larger than that in the stratiform region (30%) relative to the radar-only estimate. Nesbitt et al. (2004) did not give a clear reason of this convective-related bias but considered it as a 2A12 Bayesian scheme problem. However, this special example shows that the 2A12 overemphasizes the high frequency scattering information when estimating the liquid water content and rain rate, which may avoid a part of the low resolution and beamfilling problem caused by using low frequency emission information. But the missing of the low-frequency information in strong ice-scattering features makes this algorithm largely

biased. As mentioned in section 3.2.2, except for the beamfilling problem, the rainfall estimate from low frequencies is supposed to be better than radar-only and scattering-based algorithms because the emission-based algorithm is insensitive to PSD (Wilheit et al. 1977).

Fig. 3.39 shows the vertical profiles of mean LWC and IWC from these 4 algorithms. In the ice region, the shapes of these IWC profiles are quite similar, except that the Z-M IWC estimate above 7 km is much lower than others. As hypothesized above, the Z-IWC relation for convective regions used in the Z-M algorithm might not be suitable for the condition above 7 km because the original particle size distribution measurements in Black (1990) were taken at 6-7 km. In the rain region, the shape of the combined LWC profile is similar with Z-M, but the 2A12 LWC profiles are quite different in the lowest 1-3 km. The same problem of 2A12 V5 has been found in Fig. 3.1 from the 1-yr TRMM tropical cyclone statistics. Although more cloud model profiles have been added to the 2A12 V6 database, the improvement from V5 to V6 is focused on the magnitude of the retrievals and the physics has not been changed.

3.8 Summary and Discussion

To improve intensity forecasting of tropical cyclones and our understanding of the microphysical processes in precipitation systems, it is necessary to study the microphysical properties based on long-term, large-coverage observations from aircraft and satellite remote sensors. CAMEX and TRMM observations provide an excellent chance to achieve this goal. In this chapter, a combined radar-radiometer algorithm is developed to retrieve the vertical hydrometeor profiles in tropical cyclones and

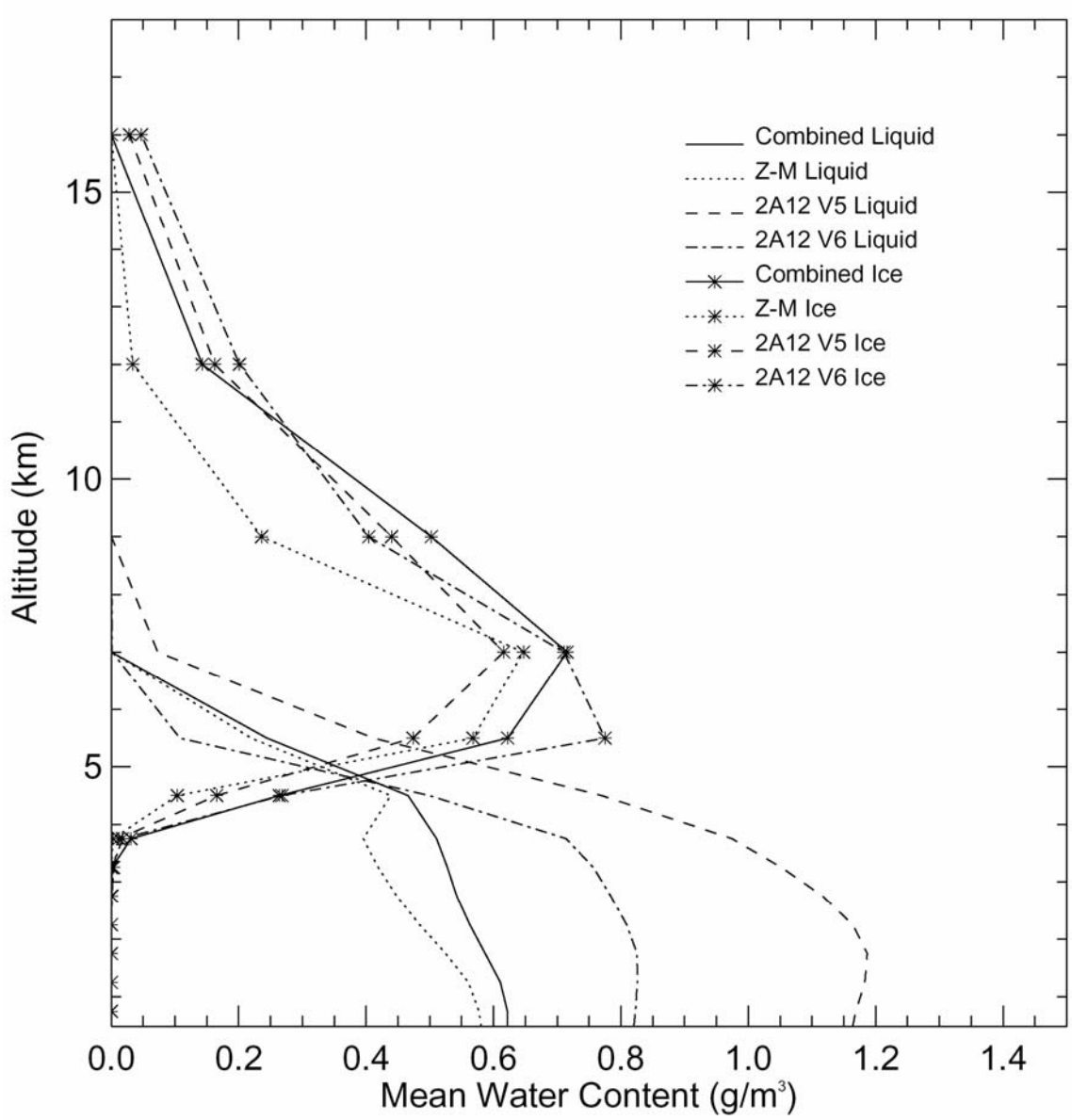

Figure 3.39. Vertical profiles of mean hydrometeor (liquid and ice precipitation water) content estimated by the combined, Z-M, 2A12 version 5 (V5), and 2A12 version 6 (V6) algorithms for box 3 in Fig. 3.27.

convective systems over oceans, which has the direct implication on the main TRMM goal – obtaining the 4-D latent heating profile over the Tropics.

The combined radar-radiometer algorithm developed here has new features compared with existing TRMM-related precipitation algorithms. It is a fully physical technique that is designed to retrieve different N_0's for rain, snow, and graupel and to provide physically meaningful estimates for both IWC and LWC profiles. It uses the vertical radar reflectivity profile to constrain the vertical shape of the retrieved hydrometeor profiles and uses the radiometer brightness temperatures to determine the vertically integrated ice and liquid water content, making the retrieval consistent with both radar and radiometer observations. A forward radiative transfer model is employed to calculate the simulated brightness temperatures in AMPR and TMI channels. A simulated annealing technique is used to minimize the differences between observed and simulated brightness temperatures.

Sensitivity tests show that the uncertainties due to the sea surface wind speed, vertical profiles of the temperature and relative humidity are comparable with the 1-D Eddington approximation error of the radiative transfer model. Especially in strong precipitation regions, the error caused by these atmospheric environment parameters is negligible. Uncertainties caused by the cloud ice and cloud liquid water are relatively larger, but they are still within the total RTM and instrument error. The main assumption of the algorithm is the snow/graupel fraction profile. In stratiform regions, all snow is assumed above the top of the melting layer. In convective regions, a simple convective intensity dependent snow/graupel fraction is assumed. No supercooled water above the

melting layer is considered. The sensitivity test shows that the major uncertainty of the retrieval will come from this assumption.

The algorithm is applied to the CAMEX-4 tropical cyclones and convection dataset. The high resolution EDOP and AMPR observations allow us to investigate the algorithm performance without significant nonuniform beamfilling problems. The retrieved IWC at about 8-11 km is compared with DC-8 aircraft *in-situ* measurements. After minimizing the mismatch problem between the ER-2 and DC-8 aircraft, the agreement is quite good in stratiform regions. But in convective regions, the uncertainty is relatively large, although the mean difference between the retrieved and aircraft derived IWC is very small. So we can conclude that the assumption of all-snow above the melting layer in stratiform regions is reasonable for tropical oceanic rainfall systems, confirming the same findings from microphysical measurements (Stith et al. 2002, Black and Hallett 1986, 1999). The very simple snow/graupel fraction assumption in convective regions is the main reason for the large IWC uncertainty.

In nature, there are transition regions between stratiform and convective regions. The microphysical characteristics in the transition region could be different with that in stratiform and convective regions. Therefore, uncertainties would exist when applying the algorithm to these kinds of regions.

An underestimate of IWC at 8-11 km by the radar-only Z-M algorithm relative to the combined radar-radiometer algorithm and aircraft *in situ* measurements is found. It is hypothesized that the Z-IWC relation (Black 1990) used here is not suitable for above 7 km altitudes. The retrieved LWC and surface rain rate are in agreement with radar-only

and radiometer-only estimates. By comparing with independent measurements, N_0 and 50 GHz brightness temperature retrievals are also quite reasonable.

After some implementation revisions, we adapted the combined radar-radiometer algorithm for application to TRMM observations. One TRMM case study provides not only an intercomparison among the combined, radar-only (Z-M), and radiometer-only (2A12) algorithms, but also an investigation of the beamfilling problem of satellite-based remote sensing retrievals.

Since there are no validation data available, this study is not aimed at investigating the absolute beamfilling problem for the radar-only retrieval (readers are referred to Kozu and Iguchi 1999 and Durden et al. 1998 for this kind of study), but to examine the beamfilling bias of the combined and 2A12 retrieval relative to the radar-only retrieval, given that the TRMM PR has a much higher resolution than TMI low frequency channels. It is shown that the 2A12 retrieval has an insensitivity problem caused by the beamfilling bias relative to the radar-only Z-M retrieval for both IWC and LWC in both nearly uniform stratiform and eyewall convective regions. However, an obvious improvement is seen from the combined retrieval. Except for the LWC in eyewall convective regions, the combined algorithm has a similar performance as the radar-only algorithm regarding the beamfilling issues. As found by Chiu et al. (1990), for the footprint size of 40 km (between TMI 19 and 10 GHz footprints), the beamfilling problem can cause about 40% underestimate of the surface rain rate on average for the radiometer-only algorithm. But for the radar-only algorithm on the TRMM PR footprint size of 4-5 km, only 11% underestimate of the surface rain rate is found (Durden et al. 1998). Since it is very complicated to deal with the beamfilling problem (Kummerow

1998; Ha and North 1995; Petty 1994a,b) with a physical model, combining radar and radiometer observations provides a workable solution to reduce the beamfilling error from the radiometer-only retrieval.

When examining the estimates by different rain types, the performance of different algorithms can be evaluated more physically. The Hurricane Isabel (2003) case study shows that IWP estimates by the combined, Z-M, and 2A12 V6 algorithms over a nearly uniform stratiform region are in very good agreement (within 4%, see table 3.9). The mean IWP in this region is underestimated by 2A12 V5. The improvement of 2A12 V6 relative to V5 comes from more cloud model profiles used to develop V6, which may partly avoid the inappropriate selection of the hydrometeor profiles by the 2A12's Bayesian scheme. However, the mean IWC profiles of 2A12 V5 and V6 show artificial non-zero values above the radar cloud top (12 km) up to 16 km altitude, indicating the problem has not been removed completely. A small underestimate of mean IWC from 7 km to 12 km altitude by the Z-M algorithm relative to the combined algorithm is found in the stratiform region (Fig. 3.33). This is consistent with the results from the CAMEX-4 application. The reason is that the Z-IWC relation may not be suitable for these higher levels.

The general spatial patterns of the combined and Z-M LWP in the stratiform region in the Hurricane Isabel orbit are in agreement with each other. It is also consistent with the pattern of PR near surface reflectivity and TMI low frequency brightness temperature observations. But the pattern of 2A12 V5 and V6 LWP is quite different, which is similar to the 85 GHz PCT pattern. This overemphasis of scattering information by 2A12 LWP retrievals is misleading in this case. A high overestimation (100% relative to the Z-M

mean LWP) of the 2A12 V5 mean LWP in the stratiform region is found, which is consistent with the results by Nesbitt et al. (2004), who pointed out that the exclusion of the melting layer emission is the main reason for overestimating the 2A12 V5 rain rate in stratiform regions. In 2A12 V6, a big improvement is made by including the melting layer effect, which decreases rain rate and LWC estimates. This study shows about 30% reduction of the mean LWP from 2A12 V5 to V6 for the Hurricane Isabel case. The combined and 2A12 V6 mean LWP retrievals in the stratiform region in the Isabel Sept. 08 orbit are very close to each other, both of which are about 30% higher than the Z-M retrieval. In the rain region, the radar-only retrieval may be biased by the attenuation correction error and the DSD assumption (Masunaga et al. 2002). However, the combined algorithm does not include the melting layer emission, while the 2A12 V6 overemphasizes the high frequency ice-scattering information. These uncertainties are probably responsible for the discrepancy.

In the eyewall convective region in the Isabel orbit, the spatial patterns of IWP retrievals from the combined and Z-M algorithm are similar, with a clear eye region as shown in the PR near surface reflectivity field. But no clear eye can be seen either from 2A12 V5 or from 2A12 V6 IWP field, showing the disadvantage of the radiometer-only method. Due to the large variation of the microphysical characteristics in the eyewall region, a large variability of the mean IWP estimates among different algorithms is found. The combined and 2A12 V5 IWP is 40% higher than the Z-M IWP, while the 2A12 V6 IWP is about 68% higher than the Z-M IWP. An underestimate of IWP by the Z-IWC relation in the convective region is very likely because this relation was derived from the microphysical measurements only at 6-7 km level (Black 1990). The amount of

supercooled water and graupel would be reduced above this level due to the relatively weaker updraft in tropical oceanic convection compared to that in the continental convection (Jorgensen et al. 1985; Zipser and Lutz 1994; Cecil et al. 2002). However, for some extreme cases, “hot towers” (very strong convective updrafts with overshoooting) might exist in hurricanes, then the assumption of no supercooled water above the melting layer in the combined algorithm could cause some overestimation of the ice amount. The variation of the microphysical characteristics in the eyewall convective region would also influence the 2A12 retrieval because both the cloud model hydrometeor profile and the radiative transfer calculation are very sensitive to the microphysics parameterization.

The LWP retrievals from the combined and Z-M algorithms in the eyewall convective region are in agreement in the mean value and general spatial pattern. As was found in the stratiform region, the 2A12 LWP V5 and V6 fields resemble the 85 GHz PCT instead of the low frequency brightness temperature patterns. This study finds that the overemphasis of the ice scattering information in the 2A12 LWP retrieval is the main reason for the overestimate of LWP in strong ice-scattering regions. It is also found that the shapes of the mean hydrometeor profiles retrieved by the combined algorithm are consistent with those retrieved by the radar-only algorithm, which are directly related to the PR reflectivity observations. But the shape of the 2A12 hydrometeor profile contains artifacts in the top of the ice region and the lowest 1-3 km of the rain region.

As an important addition to existing algorithms, the new combined radar-radiometer algorithm developed in this study has promise for improving our understanding and may lead to better quantitative precipitation estimation from remote sensing measurements. Applying the algorithm to more TRMM data will generate a

valuable database to study the microphysical properties in tropical oceanic rainfall systems and should help to improve microphysical parameterizations in numerical models. The algorithm has been developed based on several assumptions and thus can be improved with more advanced knowledge concerning the particle size distributions, particle phases, and bulk densities in the ice region. The crucial assumption of snow/graupel/supercooled-water fractions in the ice region causes a large uncertainty in convective precipitation and the transition regions. Either more microphysical observations or a better approach is needed to improve the retrieval. For the LWC retrieval in the rain region, the inclusion of the melting layer emission is necessary in order to reduce the overestimate caused by this effect.

The new combined radar-radiometer algorithm developed in this study has several advantages compared with either radar-only or radiometer-only algorithms. In the future, the Global Precipitation Mission (GPM) satellites are planned to carry a dual wavelength precipitation radar and microwave radiometers. This study implies that a fully physical combined radar-radiometer algorithm will be optimal for GPM because particle size and LWC/IWC properties could be derived from the dual-wavelength radar parameters and reduce the assumptions in the retrieval.

The intercomparison of different retrievals in this study implies that separately treating different rain types will help understanding the physical limitation of different algorithms as well as the microphysical characteristics in different precipitation types. A potential future work is to analyze the statistical variability of hydrometeor profiles in different rain types, different oceanic precipitation features, and different regions inside tropical cyclones (e.g., eyewall and rainbands).